EXPERIMENTAL STATIC STABILITY STUDIES OF SEVERAL TACTICAL MISSILE CONFIGURATIONS AT MACH NUMBERS FROM 1.76 TO 3.01

E. Earl Lindsay, et al

Arnold Engineering Development Center

Prepared for:

ARO, Incorporated

April 1975

NOTICES

When U. S. Government drawings specifications, or other data are used for any purpose other than a definitely related Government procurement operation, the Government thereby incurs no responsibility nor any obligation whatsoever, and the fact that the Government may have formulated, furnished, or in any way supplied the said drawings, specifications, or other data, is not to be regarded by implication or otherwise, or in any manner licensing the holder or any other person or corporation, or conveying any rights or permission to manufacture, use, or sell any patented invention that may in any way be related thereto.

Qualified users may obtain copies of this report from the Defense Documentation Center.

References to named commercial products in this report are not to be considered in any sense as an endorsement of the product by the United States Air Force or the Government.

This report has been reviewed by the Information Office (OI) and is releasable to the National Technical Information Service (NTIS). At NTIS, it will be available to the general public, including foreign nations.

APPROVAL STATEMENT

This technical report has been reviewed and is approved for publication.

FOR THE COMMANDER

Jimmy W. Mullins

JIMMY W. MULLINS
Lt Colonel, USAF
Chief Air Force Test Director, VKF
Directorate of Test

Frank J. Passarello

FRANK J. PASSARELLO
Colonel, USAF
Director of Test

REPORT DOCUMENTATION PAGE	READ INSTRUCTIONS BEFORE COMPLETING FORM
1 REPORT NUMBER: AEDC-TR-75-27 — 2 GOVT ACCESSION NO.	3 RECIPIENT'S CATALOG NUMBER: AD A009 137
4 TITLE (and Subtitle): EXPERIMENTAL STATIC STABILITY STUDIES OF SEVERAL TACTICAL MISSILE CONFIGURATIONS AT MACH NUMBERS FROM 1.76 TO 3.01	5 TYPE OF REPORT & PERIOD COVERED: Final Report, Aug 16 - Sept 7, 1974
	6. PERFORMING ORG. REPORT NUMBER
7 AUTHOR(s): E. Earl Lindsay and J. L. Jordan, ARO, Inc.	8. CONTRACT OR GRANT NUMBER(s)
9 PERFORMING ORGANIZATION NAME AND ADDRESS: Arnold Engineering Development Center, Arnold Air Force Station, TN 37355	10. PROGRAM ELEMENT, PROJECT, TASK AREA & WORK UNIT NUMBERS: Project 9738, System 921C
11 CONTROLLING OFFICE NAME AND ADDRESS: Army Missile Command (AMSMI-RDK), Redstone Arsenal, AL 35809	12. REPORT DATE: April 1975
	13. NUMBER OF PAGES: 112
14 MONITORING AGENCY NAME & ADDRESS(if different from Controlling Office)	15. SECURITY CLASS. (of this report): UNCLASSIFIED
	15a. DECLASSIFICATION DOWNGRADING SCHEDULE: N/A

16 DISTRIBUTION STATEMENT (of this Report)

Approved for public release; distribution unlimited.

17 DISTRIBUTION STATEMENT (of the abstract entered in Block 20, if different from Report)

18 SUPPLEMENTARY NOTES

Available in DDC.

19 KEY WORDS (Continue on reverse side if necessary and identify by block number)

guided missiles	fins
tactical weapons	sizes (dimensions)
supersonic characteristics	aerodynamic forces
aerodynamic control surfaces	wind tunnel tests

20 ABSTRACT (Continue on reverse side if necessary and identify by block number)

An experimental investigation was conducted in the low supersonic Mach number regime to obtain generalized, systematic force and moment data on several tactical missile configurations. Aerodynamic characteristics were determined for a typical missile body and nine body-fin configurations. The aerodynamic loading on each fin was also obtained for the nine fin configurations in a cruciform arrangement at zero deflection. The test was conducted at Mach numbers of 1.76, 2.00, 2.50, and 3.01 and

DD FORM 1 JAN 73 1473 EDITION OF 1 NOV 65 IS OBSOLETE

20, Continued

free-stream Reynolds numbers, based on model length, from 8.3 to 14.5 million. The angle-of-attack range was from -1 to 45 deg, and the roll angle range was from 0 to 90 deg. Results are presented to illustrate the effects of fin aspect ratio, planform shape, and planform area on the missile and fin aerodynamic characteristics.

PREFACE

The work reported herein was conducted by the Arnold Engineering Development Center (AEDC), Air Force Systems Command (AFSC), at the request of the Army Missile Command (AMSMI-RDK), Redstone Arsenal, Alabama, for the Martin-Marietta Corporation, Orlando, Florida. The work was done by ARO, Inc. (a subsidiary of Sverdrup & Parcel and Associates, Inc.), contract operator of AEDC, AFSC, Arnold Air Force Station, Tennessee, under ARO Project No. V41A-52A. The manuscript (ARO Control No. ARO-VKF-TR-74-130) was submitted for publication on December 20, 1974.

CONTENTS

ILLUSTRATIONS

Figure

Preceding page blank

Figure | Page

Figure | Page

TABLE

1.0 INTRODUCTION

As the future generation of highly maneuverable tactical missiles evolves, post-launch angle-of-attack magnitudes are expected to become increasingly higher during initial stages of flight. At the present time, few reliable methods are available for predicting missile behavior for combinations of high angle of attack and low supersonic Mach number. The generation of a methodology suitable for handling high angle-of-attack, low supersonic aerodynamics for arbitrary roll attitudes will require an empirical approach which will necessitate the correlation of a wide range of experimental data.

The purpose of this test program was to obtain generalized, systematic force and moment data on several tactical missile configurations in the low Mach number regime at high angles of attack and arbitrary roll angles. The test objective was to provide a large bank of experimental data to be used in developing methods for predicting the aerodynamic characteristics of highly maneuverable missile configurations. The test was conducted in the von Kármán Gas Dynamics Facility (VKF) Supersonic Wind Tunnel (A) at Mach numbers of 1.76, 2.00, 2.50, and 3.01 and test Reynolds numbers, based on model length, from 8.3 to 14.5 million.

Static stability and axial-force data were obtained on the missile body alone and on the body with each of nine sets of matching tail fins arranged in a cruciform configuration at zero deflection. Aerodynamic forces and moments also were measured on each of the fins in the presence of the missile body. The effects of fin planform shape, aspect ratio, and planform area on missile and fin characteristics were investigated for variations in vehicle attitude and Mach number. The angle-of-attack range was generally from -1 to 45 deg, and the roll angle range was from 0 to 90 deg.

2.0 APPARATUS

2.1 WIND TUNNEL

Tunnel A is a continuous, closed-circuit, variable density wind tunnel with an automatically driven flexible-plate-type nozzle and a 40- by 40-in. test section. The tunnel can be operated at Mach numbers from 1.5 to 6 at maximum stagnation pressures from 29 to 200 psia, respectively, and stagnation temperatures up to 750°R ($M_\infty = 6$). Minimum operating pressures range from about 1/10 to 1/20 of the maximum at each Mach number. The test model can be injected into the tunnel flow for a test run and then retracted into the installation tank for model changes without interrupting the tunnel flow. A description of the tunnel and airflow calibration is provided in the Test Facilities Handbook.*

*Test Facilities Handbook (Tenth Edition). "von Kármán Gas Dynamics Facility, Vol. 4." Arnold Engineering Development Center, May 1974.

2.2 MODEL AND FIN COMPONENTS

Photographs and details of the model and fins are shown in Figs. 1 through 4. The model and components were stainless steel and were furnished by the Martin-Marietta Corporation. The basic missile body had a 3-caliber tangent ogive nose and a 7-caliber cylindrical afterbody. The model was 37.50 in. long with a diameter of 3.75 in.

The nine matching sets of fins, shown in Figs. 3 and 4, consisted of rectangular, delta, and triangular planform geometries. Aspect ratio and planform area varied for each type of fin. The fins were aft mounted and were arranged in a cruciform configuration at zero deflection. Fin orientation and coefficient sign convention are shown in Fig. 5.

Each fin was mounted to a fin balance (Fig. 6) which was aligned and retained in a fin-balance block. Fin changes were facilitated with a series of blocks mounted in slots in the afterbody. Each set of blocks had one block forward and one block aft of each fin-balance block, which positioned the fin trailing edge in line with the model base (see Fig. 2). The blocks were retained in the afterbody slots with the model base plate.

2.3 INSTRUMENTATION

Tunnel A stilling chamber pressure was measured with a 30- or 60-psid transducer referenced to a near vacuum. Based on periodic comparison with secondary standards, the precision of these transducers (a band which includes 95 percent of the calibration data) is estimated to be within ±0.1 percent of the measured pressure. Stilling chamber temperature was measured with a copper-constantan thermocouple to a precision of ±2°F based on the thermocouple wire manufacturer's specifications.

Aerodynamic loads on the total vehicle were measured with a six-component, moment-type, strain-gage balance supplied and calibrated by VKF. Before testing was begun, static loads in each plane and combined static loads were applied to the balance to simulate the range of loads anticipated for the test. The following uncertainties represent the bands of 95 percent of the measured residuals, based on differences between the applied loads and the corresponding values calculated from the final data reduction equations. The range of static loads and the measurement uncertainties follow.

Component	Balance Design Loads	Range of Static Loads	Measurement Uncertainty
Normal force, lb	± 700	± 600	±1.2
Pitching moment,* in.-lb	±3645	±2500	±2.5
Side force, lb	± 700	± 600	±1.5
Yawing moment,* in.-lb	±3645	±2500	±3.5
Rolling moment, in.-lb	± 320	± 100	±0.4
Axial force, lb	± 150	± 75	±0.5

*About balance forward moment bridge.

The transfer distance from the balance reference location to the model moment reference location (see Fig. 2) was 1.753 in. for angles of attack below 28 deg and 3.753 in. for angles of attack above 28 deg and was measured to an estimated precision of ±0.005 in.

Aerodynamic forces and moments were measured on each of the four fins with three-component, force- and moment-type balances supplied by Martin Marietta. The four fin balances were calibrated by VKF with single and combined static loadings for the design load ranges of the balances. The uncertainties listed below were determined in the same manner as were the balance uncertainties for the total vehicle. The fin balance number indicates the balance location (see Fig. 5).

	Design and Applied Load Ranges	Measurement Uncertainty			
	Fin Balance	Fin Balance			
Component	1 through 4	1	2	3	4
Normal force, lb	±100	±1.3	±0.5	±0.5	±0.6
Hinge moment, in.-lb	± 50	±0.6	±0.3	±0.5	±0.3
Root bending moment,* in.-lb	±100	±0.5	±0.4	±0.7	±0.5

*About fin root chord

The transfer distance from the fin balance reference to the fin root chord reference location was 0.571, 0.583, 0.559, and 0.575 in. for fins 1 through 4, respectively, and was measured with an estimated precision of ±0.005 in.

It should be noted that the uncertainties presented above were determined in a calibration laboratory where conditions were ideal compared to operating conditions in the wind tunnel. Zero shifts were observed to occur occasionally on the normal-force component of fin balance number 4 at angles of attack above 28 deg, approximately doubling the magnitude of the uncertainty for that component.

Base pressure in Tunnel A was measured with 15-psid transducers referenced to a near vacuum and having full-scale calibrated ranges of 1, 5, and 15 psia. Based on periodic comparison with secondary standards, the precision is estimated to be ±0.1 percent of full scale of the range being used.

Model flow-field photographs were obtained on several configurations at selected model attitudes and test conditions. Numerous shadowgraph still photographs and schlieren movies were taken to assist in evaluating the effects of flow-field shock wave geometry and leeside separation on missile performance. The shadowgraph and schlieren recordings were obtained with a double-pass optical flow visualization system with a 35-in.-diam field of view.

Vapor screen still photographs and movies were obtained to observe and record the leeside vortex growth on selected configurations at various model stations and attitudes. Model flow-field illumination was provided with a 50-mw helium-neon continuous wave laser with the output beam expanded in one direction with an 8-mm positive cylindrical lens. Still photographs and movies were recorded with a Hasselblad 70-mm and a Mitchell 16-mm camera, respectively. Typical vapor screen photographs for the body alone at Mach number 2.0 are given in Fig. 7.

3.0 PROCEDURE

3.1 TEST CONDITIONS

A test summary showing all configurations tested and the variables for each is presented in Table 1. The test was conducted in two phases, and a summary of the test conditions for each test phase is given below.

	Test Conditions					
Test Phase	M_∞	p_o, psia	T_o, °R	q_∞, psia	p_∞, psia	$Re_\ell \times 10^{-6}$
1	1.76	10.0	565	4.01	1.85	8.3
1,2	2.00	11.5	565	4.12	1.47	8.7
1,2	2.50	16.1	565	4.12	0.94	9.5
1	3.01	32.4	570	5.51	0.87	14.5
2	3.01	22.5	570	3.83	0.60	10.0

3.2 TEST PROCEDURE

The test was conducted in two phases in order to cover the angle-of-attack range from -1 to 45 deg. The angle-of-attack ranges were from approximately -1 to 28 deg and 28 to 45 deg for the first and second test phases, respectively. The roll angle range was from 0 to 90 deg during both phases and was provided by a remotely operated roll mechanism forward of the sting prebend. Limitations in the model attitude ranges are noted in the Test Summary, Table 1.

Data acquisition and model attitude positioning were accomplished with both the pitch-pause and the continuous sweep techniques. The VKF-built Programmed Position Control System (PPCS) was modified for the test and was used during both modes of operation to substantially increase the data acquisition rate. Model pitch and roll attitude requirements for both the pitch-pause and continuous sweep modes were programmed into the PPCS before the test was begun. Data acquisition and model positioning operations were performed automatically during the test by selecting the desired mode of operation and starting the PPCS.

The pitch-pause method was utilized to obtain data on all configurations for the angle-of-attack range from approximately -1 to 45 deg at zero roll. After the model was positioned at the minimum angle of attack and the base pressure stabilized, the PPCS automatically controlled the data recording and model attitude systems until the maximum pitch angle was reached. At each angle of attack in the pitch-pause mode, the control unit delayed approximately 10 sec before recording the data to allow the base pressures to stabilize. The pitch-pause data were obtained primarily to adequately define the base pressure variation with angle of attack.

In order to more nearly simulate the maneuvering mode of a tactical missile, the test was conducted primarily in the continuous sweep mode with variations in roll angle for constant pitch angles of attack. During this mode of operation, the model was pitched to the minimum angle of attack at zero roll and the base pressure allowed to stabilize. The PPCS then initiated the data acquisition system and rolled the model through the roll range from 0 to 90 deg at a nominal sweep rate of 2 deg/sec. The automatic control unit then pitched the model to the next angle of attack, and after a delay of about 10 sec, rolled the model back from 90 deg to 0 roll while recording the data. This sequence was repeated until the model attitude matrix was completed. The delay after each angle-of-attack change allowed the base pressures to stabilize at that pitch-and-roll-angle combination. Base pressures were measured on the first data point during the sweep mode and used throughout the roll sweep to adjust the total axial-force measurements. Generally, the angle-of-attack range was approximately -1 to 45 deg. Data were calculated, tabulated, and plotted at each angle of attack and each 2-deg increment of the roll angle range. Data were sampled at a rate of 1000 items/sec, and 14 data loops were averaged for each data point. Approximately 95 percent of the test data were recorded in the continuous sweep mode of operation.

3.3 DATA PRECISION

3.3.1 Test Conditions

Uncertainties (bands which include 95 percent of the calibration data) in the basic tunnel parameters, p_o, T_o, and M_∞, were obtained from repeat calibrations of the instrumentation (see Section 2.3) and from the repeatability and uniformity of the test section flow during calibrations. These uncertainties were then used to estimate uncertainties in the other free-stream properties, using the Taylor series method of error propagation.

Test Phase	M_∞	Uncertainty, percent M_∞	p_o	T_o	p_∞	q_∞	Re_ℓ
1	1.76	±0.7	±0.1	±0.4	±1.8	±0.5	±0.7
1,2	2.00	±0.5	±0.1	±0.4	±1.6	±0.6	±0.7
1,2	2.50	±0.3	±0.1	±0.4	±1.2	±0.6	±0.7
1,2	3.01	±0.4	±0.1	±0.4	±1.8	±1.0	±0.9

3.3.2 Aerodynamic Coefficients

Vehicle aerodynamic forces and moments are presented in the body axis system. Pitching and yawing momer s are referenced to a point on the model centerline at 64 percent of the model length from the nose (see Fig. 2). The model base diameter was used as the reference length for all body moment coefficients. Axial-force data have been adjusted to zero base axial force using measured model base pressures obtained and applied as described in Section 3.2.

The balance uncertainties listed in Section 2.3 were combined with uncertainties in the tunnel parameters, using the Taylor series method of error propagation, to estimate the precision of the aerodynamic coefficients for each test condition, and these are presented below.

Test Phase	M_∞	Uncertainty at Maximum Measured Coefficient Value, percent C_N	C_m	C_Y	C_n	C_ℓ	C_A
1	1.76	±0.6	±0.5	±0.6	±0.7	±0.9	±3.5
1,2	2.00	±0.6	±0.6	±0.6	±0.8	±0.9	±2.9
1,2	2.50	±0.6	±0.7	±0.6	±0.8	±1.0	±2.6
1	3.01	±1.0	±1.0	±1.1	±1.1	±2.1	±2.6
2	3.01	±1.0	±1.1	±1.1	±1.2	±1.4	±2.7

Test Phase	M_∞	Absolute Uncertainty* near Balance Minimum Load C_N	C_m	C_Y	C_n	C_ℓ	C_A
1	1.76	±0.027	±0.015	±0.034	±0.021	±0.002	±0.011
1,2	2.00	±0.026	±0.015	±0.033	±0.021	±0.002	±0.011
1,2	2.50	±0.026	±0.015	±0.033	±0.021	±0.002	±0.011
1	3.01	±0.020	±0.011	±0.025	±0.015	±0.002	±0.008
2	3.01	±0.028	±0.016	±0.035	±0.022	±0.003	±0.012

*These values were computed directly from the balance uncertainties (Section 2.3) and the nominal test conditions (Section 3.1), which give an indication of the best possible precision. Force transfer is not included in these estimates of moment uncertainty (i.e., C_N and C_Y = 0).

Fin aerodynamic forces and moments are presented in the fin axis system (see Fig. 5). Root-bending moments are referenced to the individual fin root location (see Fig. 4a). The fin uncertainties were determined by the same method as the missile uncertainties. The C_{N_T}, C_{HM_T}, and C_{RB_T} values given below refer to those obtained for fins T3-2, T3-1, and T3-4, respectively, which generally produced the maximum fin aerodynamic loads.

		Uncertainty at Maximum Measured Coefficient Value, percent					
		Fin Balance Number 1			Fin Balance Number 2		
Test Phase	M_∞	C_{N_T}	C_{HM_T}	C_{RB_T}	C_{N_T}	C_{HM_T}	C_{RB_T}
1	1.76	±2.6	±3.4	±1.1	±0.8	±2.7	±0.6
1,2	2.00	±2.1	±2.2	±1.2	±0.8	±1.7	±0.8
1,2	2.50	±2.0	±1.4	±1.5	±0.7	±1.2	±0.9
1	3.01	±2.6	±2.3	±1.7	±1.2	±1.9	±1.2
2	3.01	±2.4	±1.8	±2.0	±1.1	±1.6	±1.3

		Fin Balance Number 3			Fin Balance Number 4		
Test Phase	M_∞	C_{N_T}	C_{HM_T}	C_{RB_T}	C_{N_T}	C_{HM_T}	C_{RB_T}
1	1.76	±0.8	±4.6	±0.8	±1.1	±2.9	±0.7
1,2	2.00	±0.7	±2.9	±1.0	±1.0	±1.9	±0.8
1,2	2.50	±0.7	±1.9	±1.1	±1.0	±1.2	±1.0
1	3.01	±1.2	±3.1	±1.4	±1.4	±2.0	±1.2
2	3.01	±1.1	±2.3	±1.5	±1.3	±1.6	±1.3

		Absolute Uncertainty* Near Balance Minimum Load					
		Fin Balance Number 1			Fin Balance Number 2		
Test Phase	M_∞	C_{N_T}	C_{HM_T}	C_{RB_T}	C_{N_T}	C_{HM_T}	C_{RB_T}
1	1.76	±0.0235	±0.0008	±0.0014	±0.0059	±0.0007	±0.0007
1,2	2.00	±0.0229	±0.0008	±0.0014	±0.0058	±0.0006	±0.0007
1,2	2.50	±0.0229	±0.0008	±0.0014	±0.0058	±0.0006	±0.0007
1	3.01	±0.0171	±0.0006	±0.0010	±0.0043	±0.0005	±0.0005
2	3.01	±0.0246	±0.0009	±0.0015	±0.0062	±0.0007	±0.0007

*These values were computed directly from the fin balance uncertainties (Section 2.3) and the nominal test conditions (Section 3.1), which give an indication of the best possible precision.

Absolute Uncertainty Near Balance Minimum Load (Continued)

Test Phase	M_∞	Fin Balance Number 3 C_{N_T}	Fin Balance Number 3 C_{HM_T}	Fin Balance Number 3 C_{RB_T}	Fin Balance Number 4 C_{N_T}	Fin Balance Number 4 C_{HM_T}	Fin Balance Number 4 C_{RB_T}
1	1.76	±0.0055	±0.0012	±0.0016	±0.0094	±0.0007	±0.0005
1,2	2.00	±0.0053	±0.0011	±0.0015	±0.0092	±0.0007	±0.0005
1,2	2.50	±0.0053	±0.0011	±0.0015	±0.0092	±0.0007	±0.0005
1	3.01	±0.0040	±0.0008	±0.0011	±0.0068	±0.0005	±0.0004
2	3.01	±0.0057	±0.0012	±0.0016	±0.0098	±0.0007	±0.0005

The uncertainty in model attitude, α and ϕ, is estimated to be ±0.1 deg.

4.0 RESULTS AND DISCUSSION

The purpose of the test program was to obtain generalized, systematic force and moment data on several tactical missile configurations in the low Mach number range at high angles of attack and arbitrary roll angles. The primary objective of the test was to provide a bank of experimental data to be used in developing methods for predicting the aerodynamic characteristics of various missile configurations. Results are presented to illustrate typical effects of fin planform shape, aspect ratio, and planform area on missile and fin aerodynamic characteristics for variations in vehicle attitude and Mach number. Missile aerodynamic coefficients are presented for the body axis system. Pitching and yawing moments are referenced to a point on the model centerline at 64 percent of the model length (0.64ℓ) from the nose. Fin aerodynamic coefficients are presented in the fin axis system.

Typical effects of variations in fin planform shape, planform area, and aspect ratio and the influence of Mach number on missile static stability and axial-force characteristics and fin aerodynamic force and moment coefficients are illustrated in Figs. 8 through 15 for the vehicle at zero roll. The fin aerodynamic coefficients are presented for Fin 2, one of the horizontal fins when the vehicle is at ϕ = 0 (see Fig. 5).

The influence of fin planform shape on missile and fin aerodynamic characteristics is illustrated in Figs. 8 and 9, respectively, for Mach numbers 1.76, 2.00, 2.50, and 3.01 and ϕ = 0. Results are presented for rectangular, delta, and triangular shaped fins with an aspect ratio of 1.0 and approximately the same planform area. Figure 8 shows a general decrease in missile nose-up pitching moment as fin leading-edge sweep angle decreased from the triangular, to the delta, to the rectangular fin planform shape. It is also evident from Fig. 8 that fin planform shape had little measurable effect on missile normal-force curve slope and that the magnitude of the axial-force coefficients produced

by the delta and triangular fins was approximately 5 to 10 percent less than that of the rectangular fin.

Figure 9 shows that the fin normal-force coefficient curve slope was greatest for the rectangular fin planform shape and decreased with increasing fin leading-edge sweep angle for the delta and triangular fins. This, of course, was reflected in the missile C_m curves of Fig. 8, where an incremental decrease in C_m was noted for the rectangular fins as compared to the other two shapes. Furthermore, spot checks made indicate that fin-body interference loading is identical or negligible since the C_{N_T} increments between the fins when converted to missile pitching moments agree well with the C_m increments measured on the overall missile (Fig. 8) between the different fins. The differences in C_{N_T} between the fins (doubled for two fins) are small enough relative to overall missile loads as to lie within the symbols on the C_N curves of Fig. 8. Of particular interest is the observation that the fins approached a stall condition near 40 deg angle of attack at Mach number 2.00 and that the angle of attack where stall occurred decreased with increasing fin sweep angle. There was no evidence of fin stall above Mach number 2.00. Fin hinge moment and root bending-moment coefficients presented in Fig. 9 indicate that the fin chordwise and spanwise center-of-pressure location moved aft and inboard, respectively, with increasing fin leading-edge sweep. It is also noteworthy that the hinge moment on the rectangular fin stayed essentially constant over most of the angle-of-attack range and that the absolute level reached was lower than for the other fins, at least for $M_\infty \geq 2.0$.

The effect of fin planform area on missile and fin aerodynamic characteristics is presented in Figs. 10 and 11, respectively, for each Mach number at $\phi = 0$, for the delta shaped fin with an aspect ratio of 2.0. Figure 10 shows the magnitude of the increases obtained in missile forces and moments by the approximately five-fold increase in fin area. The angle-of-attack range of the largest fin was restricted by fin balance loading limitations. The fin loading characteristics (Fig. 11) were nondimensionalized by the appropriate fin reference area and length; consequently, there are relatively small variations shown in these coefficients.

Typical effects of variation in fin aspect ratio on missile and fin aerodynamic characteristics are illustrated in Figs. 12 and 13, respectively, for the delta fin configuration at each Mach number and $\phi = 0$. It can be seen from Fig. 12 that fin aspect ratio effects on missile aerodynamic characteristics cannot be isolated from the effects of change in planform area, which were noted previously in Fig. 10. Figure 13, however, shows that the fin normal-force and root-bending-moment coefficients increased with increased fin aspect ratio. Generally, the fin chordwise center of pressure was forward of the fin hinge line for angles of attack below approximately 10 deg and aft of the hinge line at the higher angles of attack.

The influence of Mach number on missile and fin aerodynamic characteristics is presented in Figs. 14 and 15, respectively, for the body-alone configuration and rectangular, delta, and triangular fin configurations with $\phi = 0$. The three fin planform shapes have an aspect ratio of 1.0 and approximately the same planform area. Figure 14 shows that the effects of Mach number on the body-alone configuration were greatest at high angles of attack ($\alpha \gtrsim 20$ deg), with C_N and C_m decreasing with increased Mach number. The same trend was obtained in C_N for the finned bodies; however, C_m for these configurations increased with increase in M_∞ for $\alpha \lesssim 25$ deg, and this trend reversed at the higher angles of attack although there was no measurable difference in C_m for $M_\infty = 2.5$ and 3.0 at $\alpha \gtrsim 25$ deg. Close scrutiny of the body-alone data also shows a reversal in the effects of Mach number on both the C_N and C_m curves. Typical low supersonic axial-force characteristics were obtained on all configurations, with the crossover in C_A level occurring between approximately 15 and 20 deg angle of attack. The effect of Mach number on fin force and moment coefficients is presented in Fig. 15 and shows that fin-loading characteristics generally decreased with increased Mach number. It may be of interest to note that checks made at maximum angle of attack comparing the C_m increments between the body alone and with rectangular fins, with that computed from the fin loading data, indicate a fin-body interference loading contribution to missile C_m of about 10 percent at $M_\infty = 1.76$ and 5 percent at $M_\infty = 3.0$.

There was no measurable effect on longitudinal-stability and axial-force coefficients for the body-alone configuration as the Reynolds number, Re_ℓ, was reduced from 14.5 to 10 million at Mach number 3.01 for angles of attack from 28 to 45 deg.

Typical missile and fin force and moment data obtained during the continuous sweep roll mode of operation are presented in Figs. 16 through 27 to illustrate the variations in the aerodynamic coefficients with roll angle at a constant angle of attack for different fin configurations and Mach numbers. Missile data are presented for the missile roll angle range from 0 to 90 deg. Fin data are presented to illustrate the variations in the fin force and moment coefficients as a fin rolled from fin position number 1 (top) to fin position number 3 (bottom). The fin data presented combine results for Fin 1 (ϕ_T = 0 to 90 deg) and Fin 2 (ϕ_T = 90 to 180 deg) and are for the sign convention shown in Fig. 5 for Fin 2.

Figures 16 through 18 illustrate typical variations in missile and fin force and moment coefficients with roll angle for configurations with rectangular, delta, and triangular fin shapes at Mach number 2.00 and angles of attack of approximately 10, 21, 32, and 43 deg. Data are presented for the configurations with fins of aspect ratio 1.0 and about the same planform area. Figures 16 and 17 show the orderly variation of the normal force, pitching-moment, side-force, and yawing moment coefficients with increasing model

roll angle. The effects of roll on these coefficients increased, as expected, with increasing angle of attack. Increased roll angle produced only small variations in the axial-force coefficients for the different fins and pitch angles presented. The effect of roll angle on missile rolling-moment coefficient was similar for each fin shape, with the variation in rolling-moment coefficient being greater for the swept leading-edge fins at the maximum pitch angle of 43 deg. Figure 18 shows that the fin roll position (ϕ_T) at which fin maximum normal-force and root-bending-moment coefficients occurred varied from approximately 100 deg at 10 deg angle of attack to about 130 deg at 43 deg angle of attack. Leeside body separation effects are evident for fin roll positions between 0 and 40 deg at 21 and 32 deg angle of attack as fin normal-force coefficients indicate a larger force acting on the leeside than on the windward side of the fin.

Variations in missile and fin force and moment coefficients with roll angle for configurations with different delta fin planform areas for an aspect ratio of 2.0 are presented in Figs. 19 through 21 for Mach number 2.00. Figures 22 through 24 illustrate typical variations in missile and fin aerodynamic coefficients with roll angle for configurations with different delta fin aspect ratios at Mach number 2.00. Although coefficient magnitudes differ, these figures show variations of missile and fin coefficients with roll angle similar to those described previously (Figs. 16 through 18). Two exceptions noted are the reversal in missile rolling-moment characteristics for the configuration with the tallest fin (T3-4) at 10 deg angle of attack (Figs. 20a and 23a) and a more orderly fin hinge-moment variation (Figs. 21 and 24).

Figures 25 through 27 show typical variations in missile and fin force and moment coefficients with roll angle for Mach numbers 1.76, 2.00, 2.50, and 3.01 for a delta fin configuration at angles of attack of 10, 21, 32, and 43 deg. Figures 25 and 26 show that the variations in missile normal-force, pitching-moment, side-force, and yawing-moment coefficients with roll angle for all Mach numbers were as orderly as noted previously for M_∞ = 2.0. Model roll had little effect on the magnitude of the axial-force coefficients for any of the Mach numbers, whereas the variation in missile roll control with roll angle decreased considerably with increasing Mach number. Figure 27 shows no significant effects of Mach number on the variation in fin force and moment coefficients with roll angle. The leeside flow effect on variations in the fin coefficients with fin roll position between 0 and 40 deg decreased with increasing Mach number.

5.0 CONCLUDING REMARKS

A static force test was conducted on typical tactical missile configurations at Mach numbers from 1.76 to 3.01 at angles of attack up to 45 deg and roll angles from 0 to 90 deg. Based on the results presented, the following observations are noted:

1. For fins of the same aspect ratio and planform area, the rectangular fins produced higher control forces and moments than triangular and delta shaped fins.

2. Hinge-moment coefficients for the rectangular fin were generally smaller in magnitude than those for the other two fin shapes and were almost constant over the angle-of-attack range.

3. In general, the fins indicated a stall condition at Mach number 2.00 near 40 deg angle of attack. There was no indication of fin stall at the higher Mach numbers.

4. Fin normal-force and root-bending moment coefficients increased with increased fin aspect ratio for fins of the same planform shape.

5. Increased Mach number decreased the normal-force and pitching-moment coefficients of the body-alone configuration at high angles of attack ($\alpha >$ 20 deg). These trends were reversed at the lower angles of attack, where the effects of Mach number were much smaller.

6. Increased Mach number increased total missile pitching moment for angles of attack below about α = 25 deg. At higher angles of attack the effect reversed, at least for $M_\infty \lesssim 2.50$. Both fin and missile normal force decreased with increased Mach number.

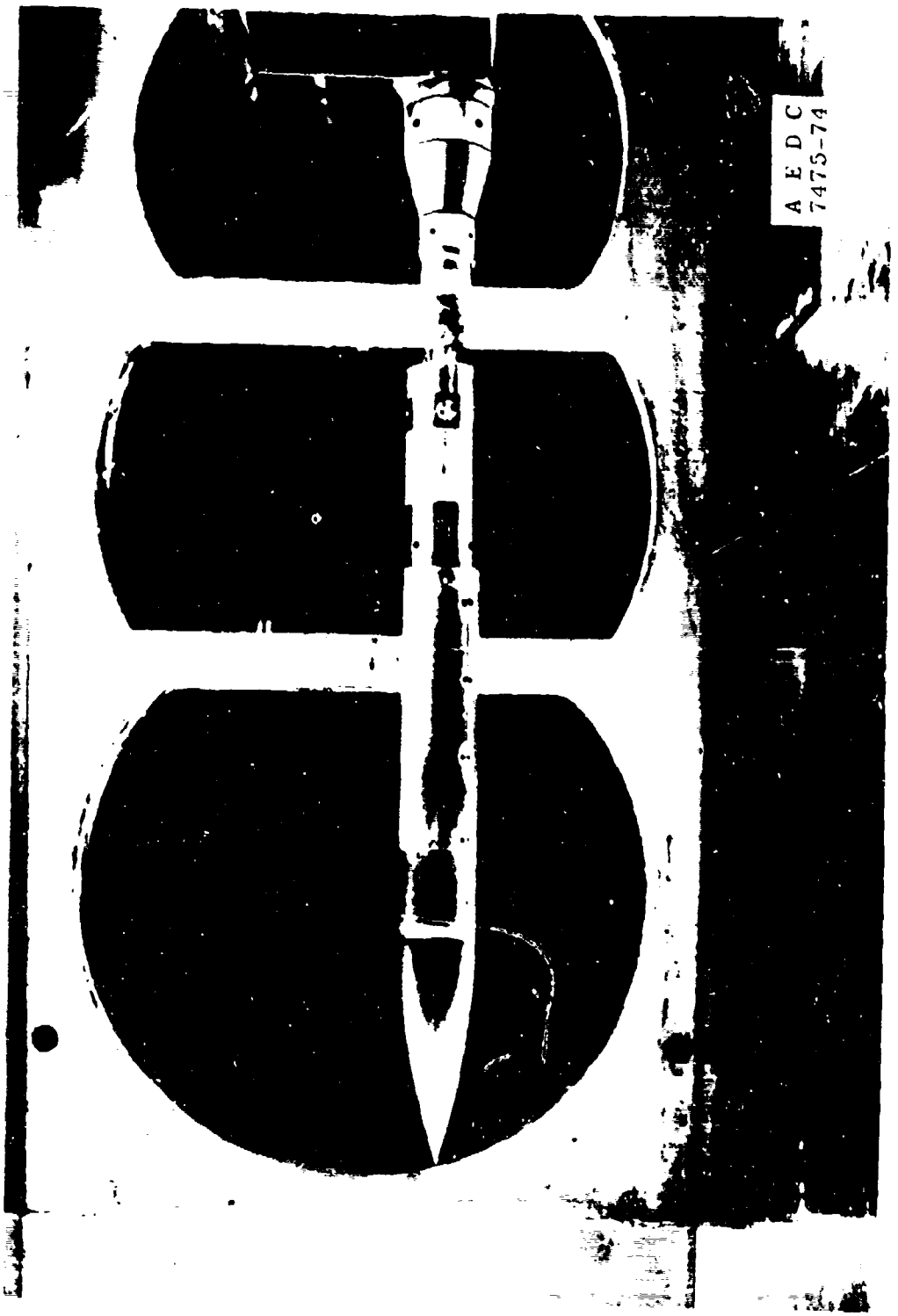

a. Configuration B, $\alpha = 0$

Figure 1. Model installation in tunnel A.

b. Configuration B'T1-5, $\alpha \approx 42$ deg

Figure 1. Concluded.

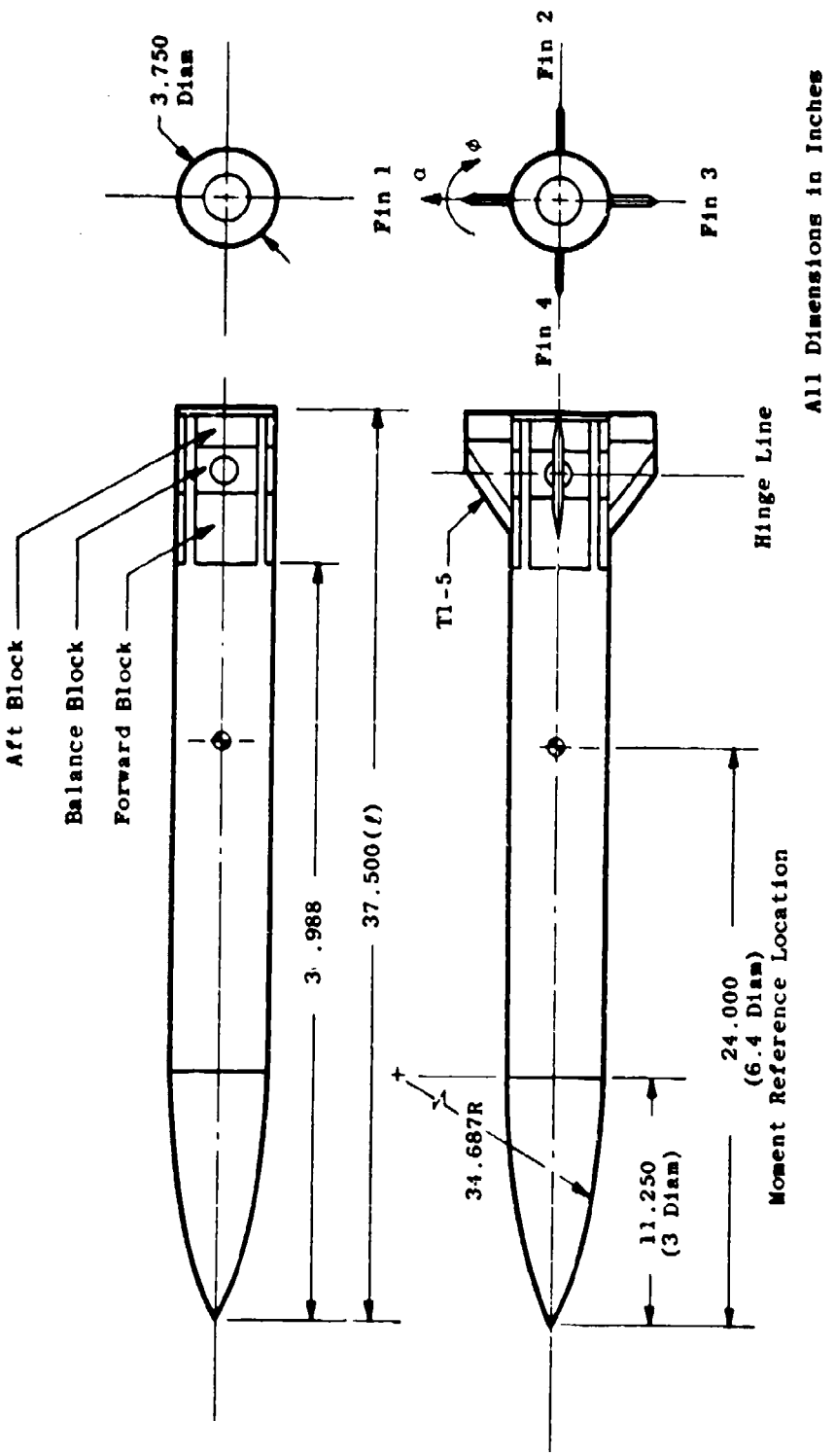

Figure 2. Model details.

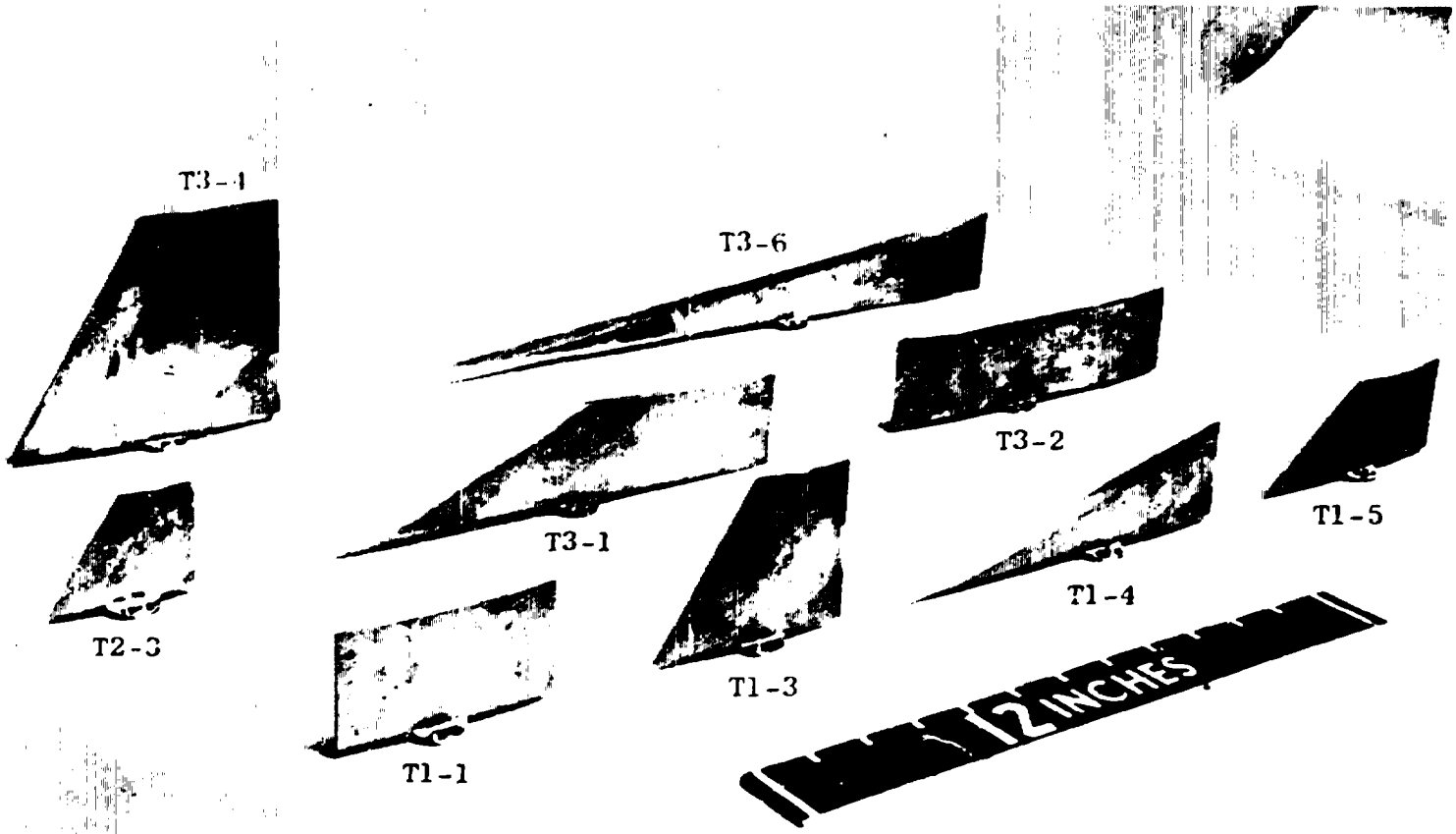

Figure 3. Photograph of fin configurations.

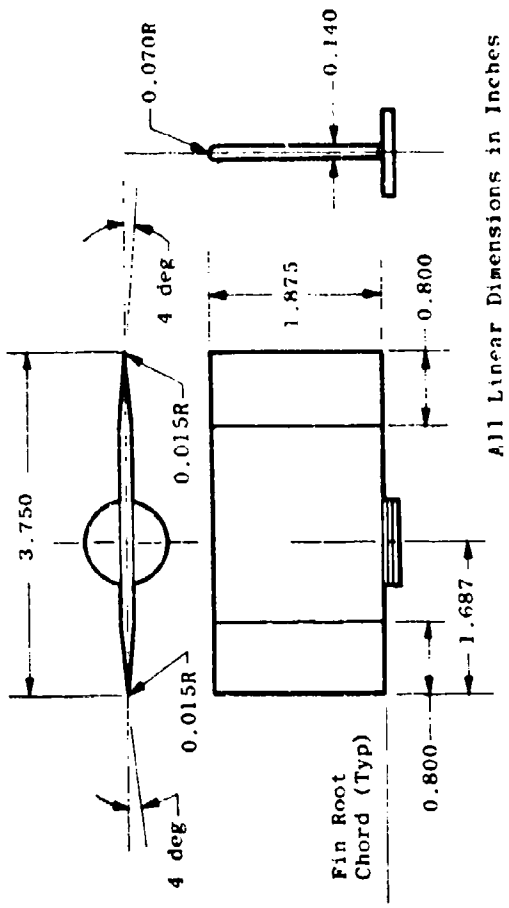

a. Fin T1-1

Figure 4. Fin details.

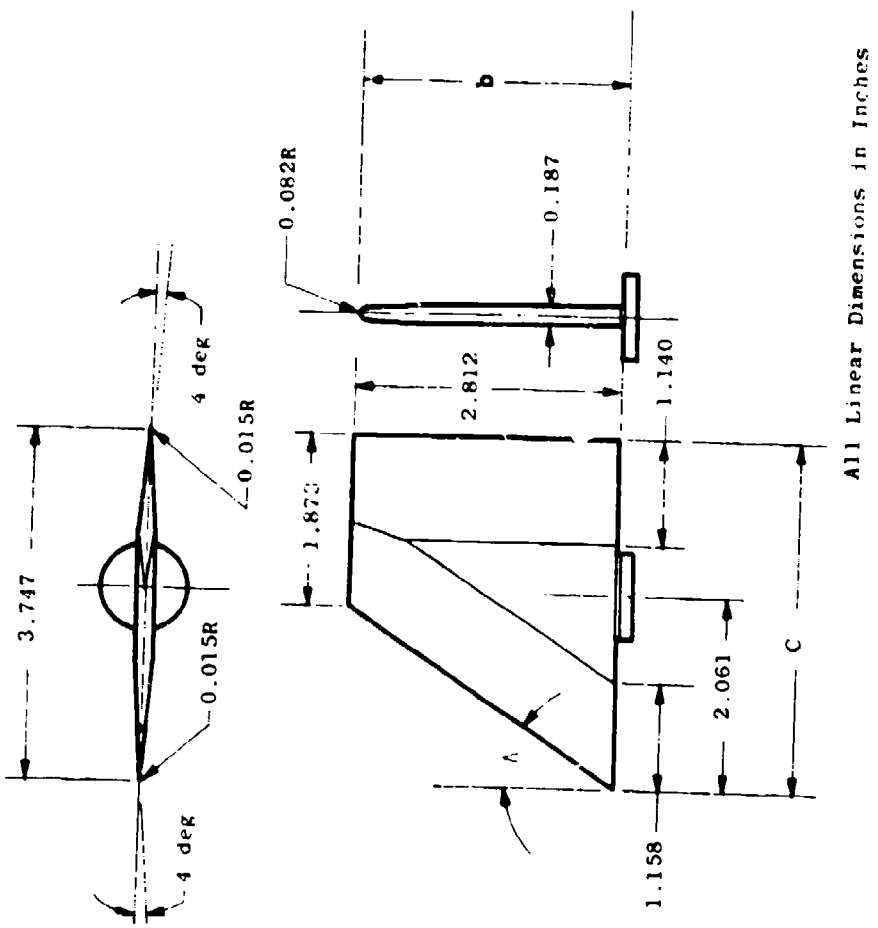

All Linear Dimensions In Inches

b. Fin T1-3
Figure 4. Continued.

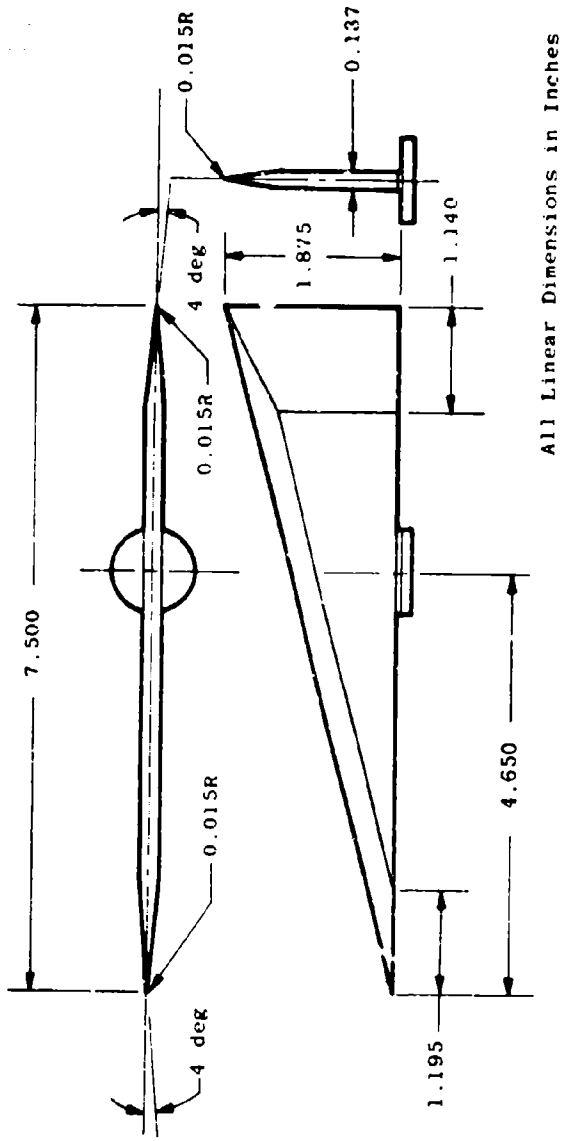

c. Fin T1-4
Figure 4. Continued.

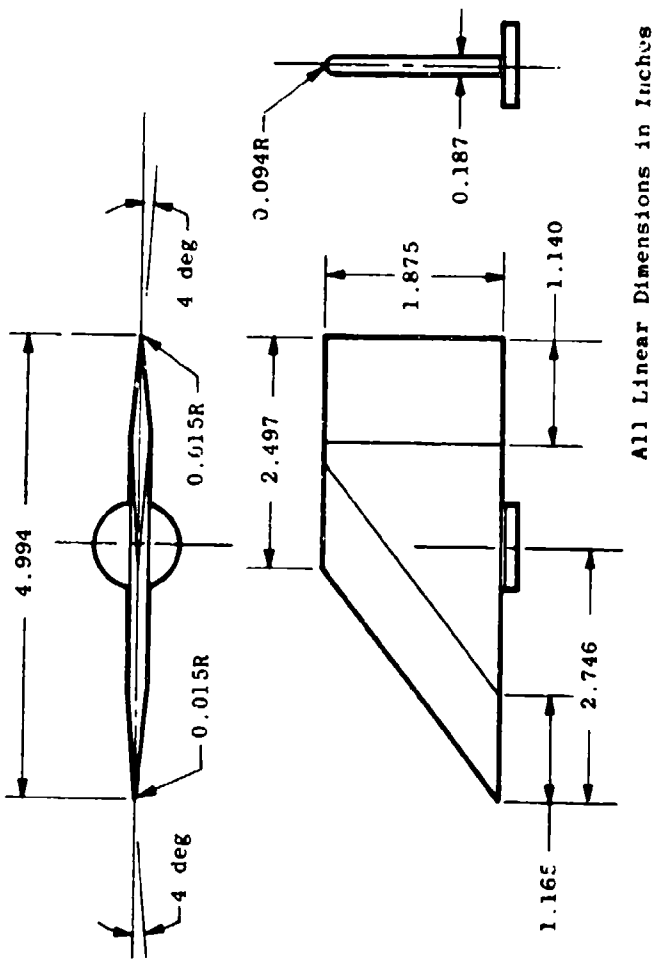

d. Fin T1.5

Figure 4. Continued.

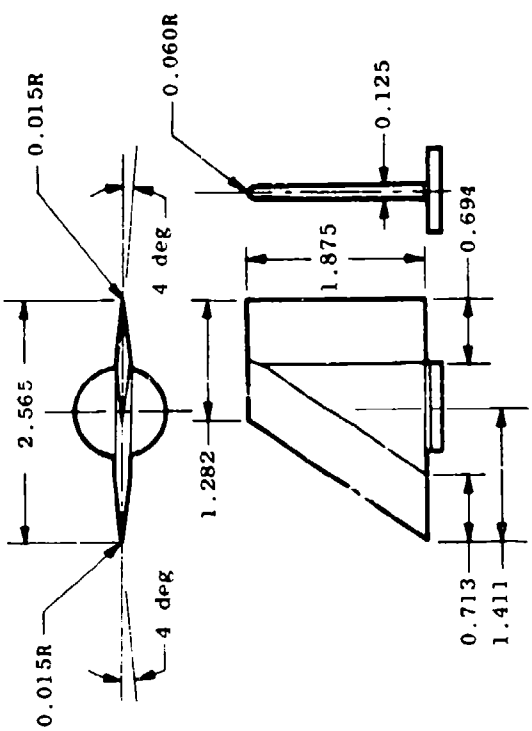

e. Fin T2-3
Figure 4. Continued.

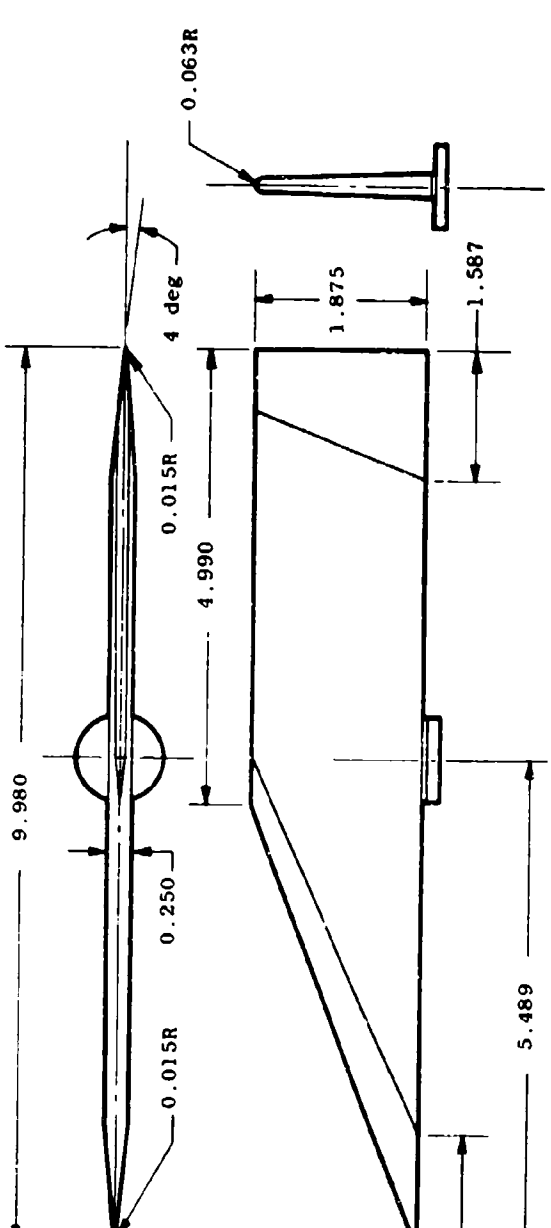

f. Fin T3-1

Figure 4. Continued.

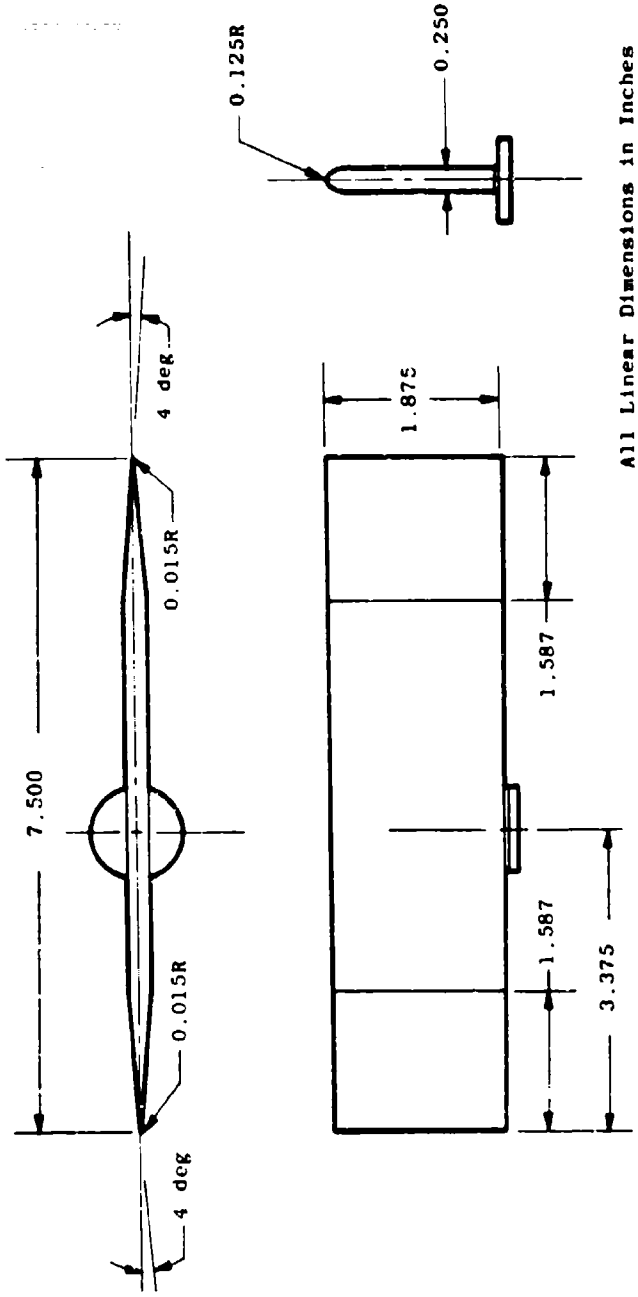

g. Fin T3-2
Figure 4. Continued.

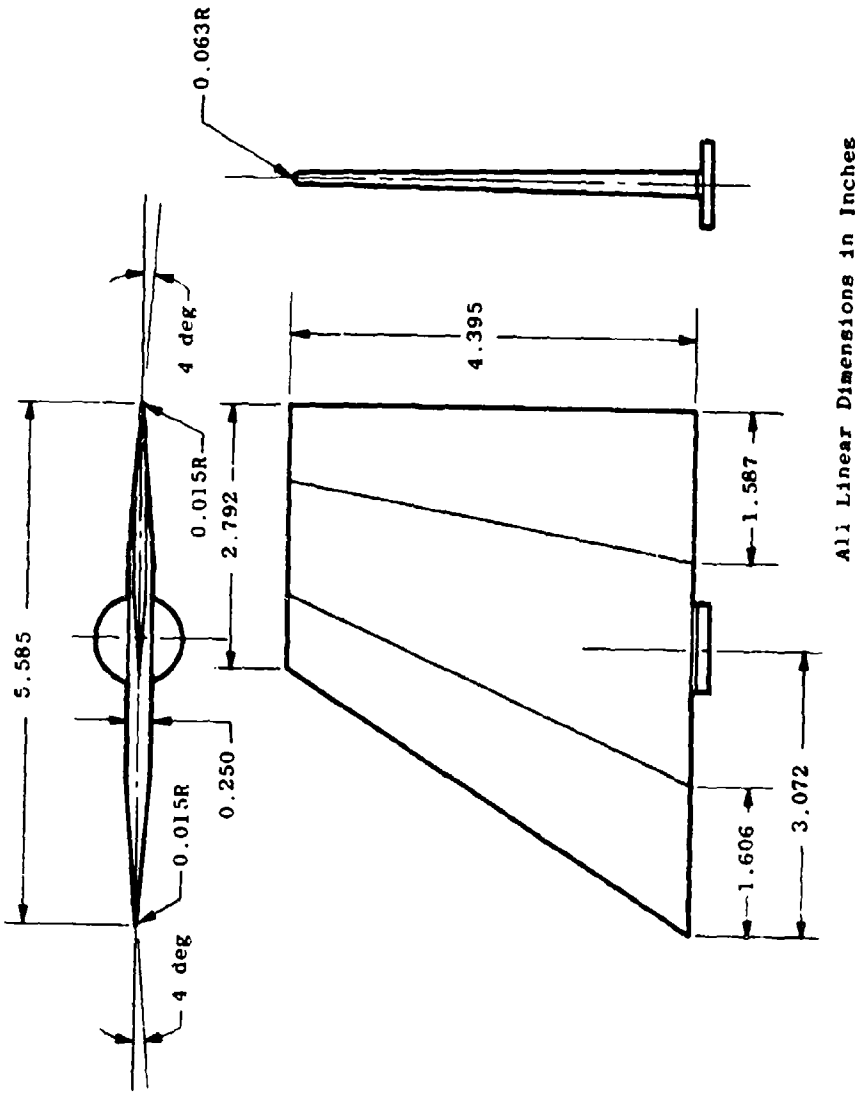

h. Fin T3-4
Figure 4. Continued.

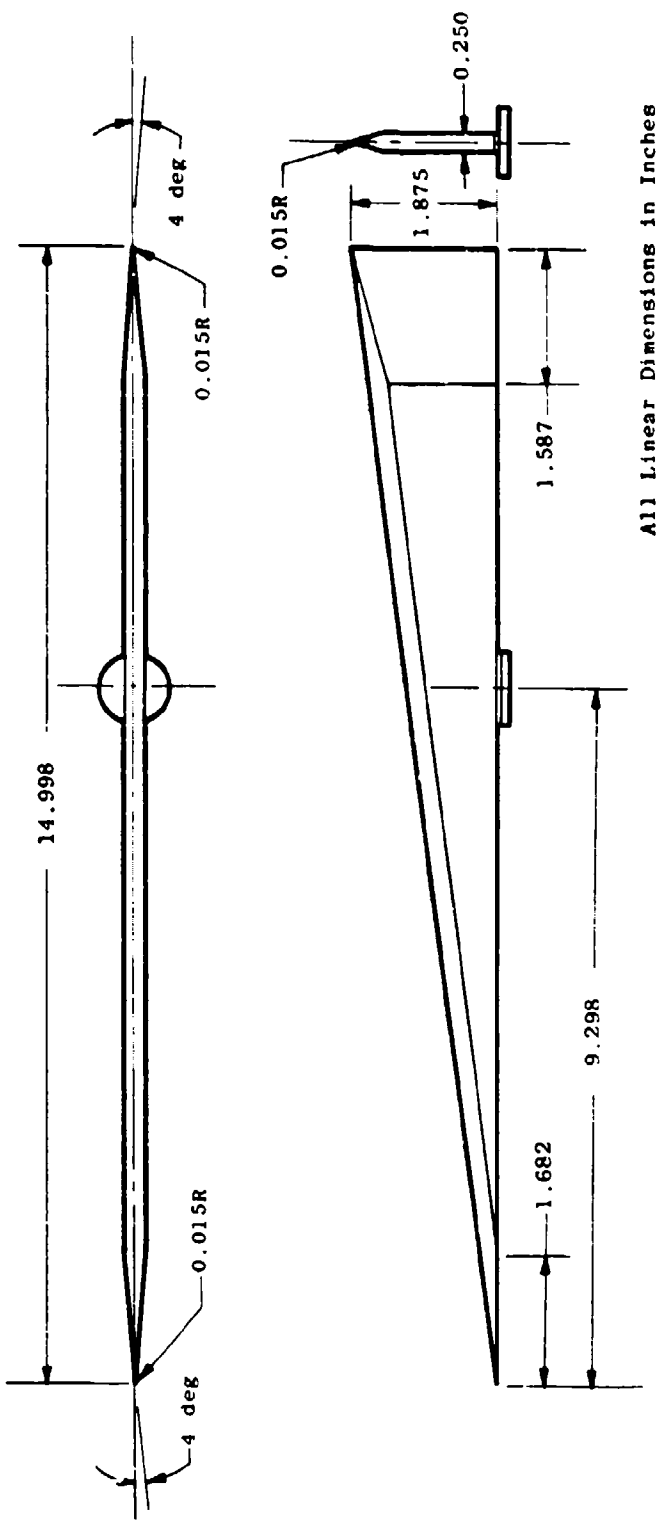

i. Fin T3-6

Figure 4. Concluded.

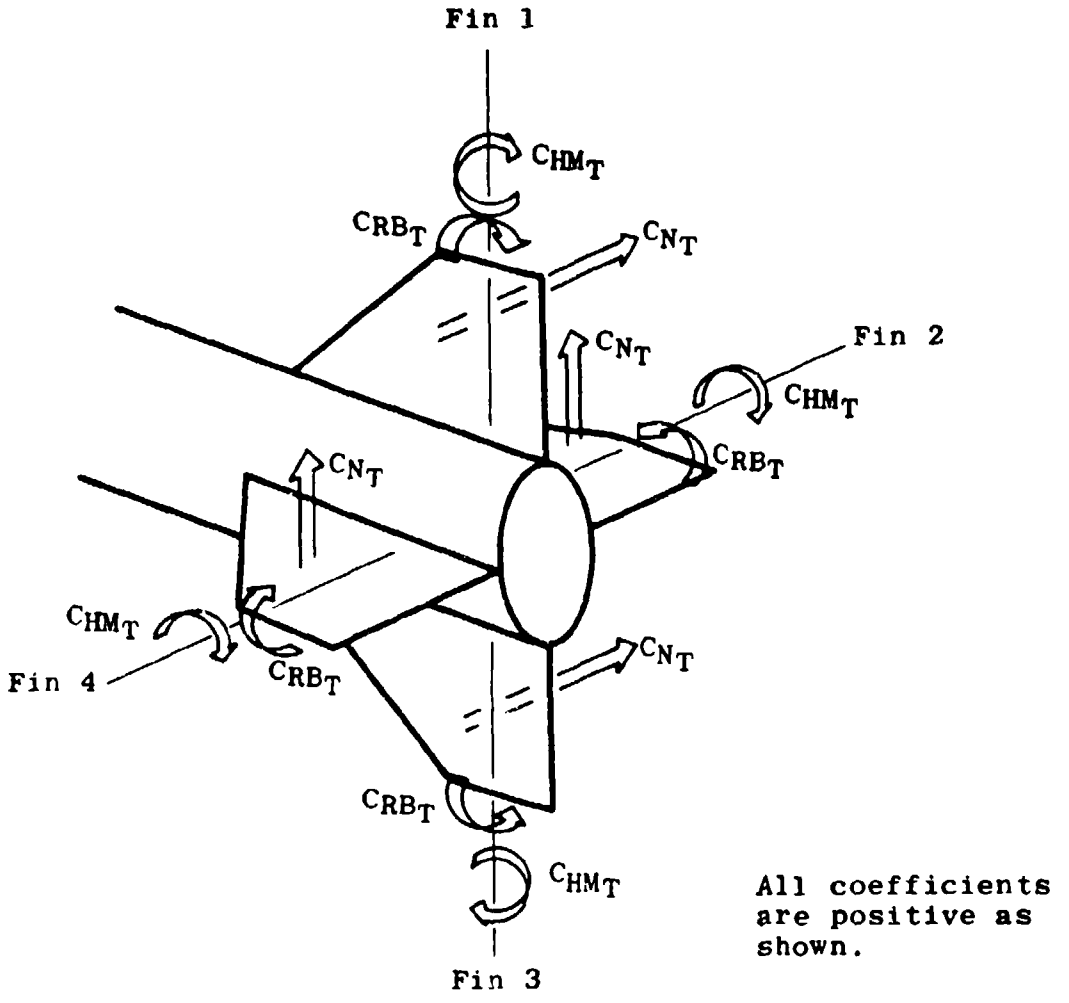

Figure 5. Fin orientation and aerodynamic coefficient sign convention.

Figure 6. Photograph of fin balance.

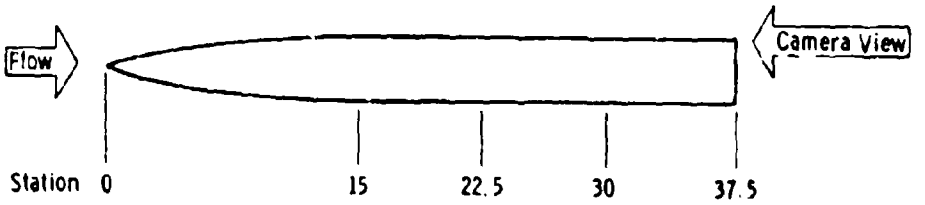

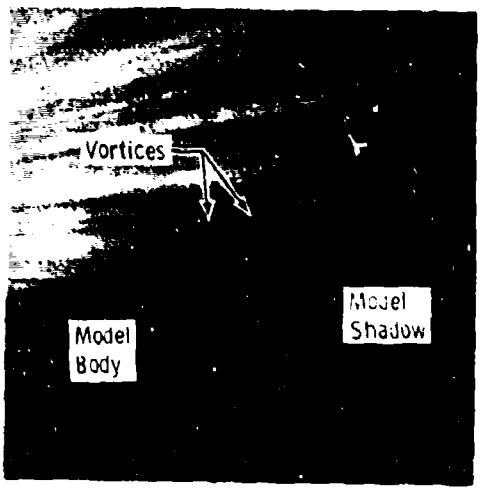

Station 15

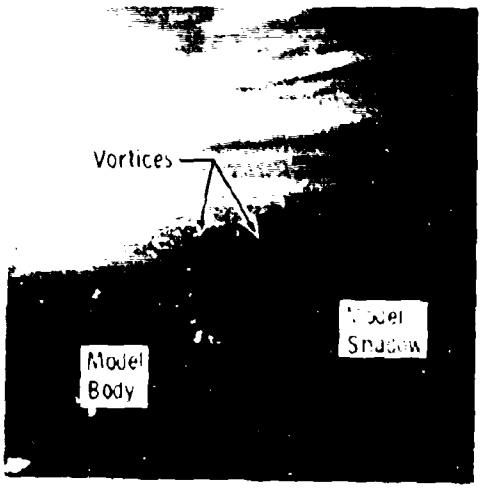

Station 22.5

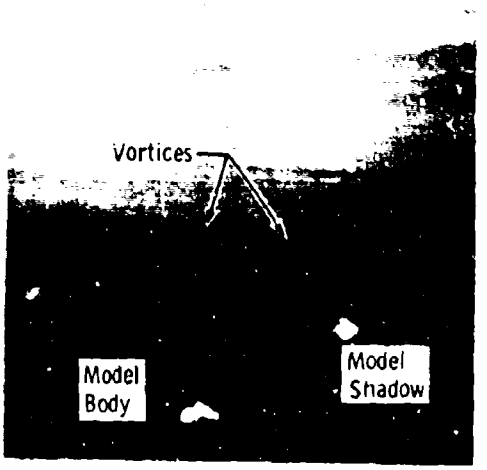

Station 30

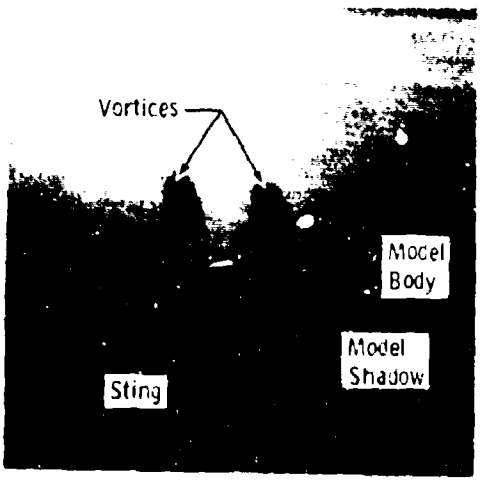

Station 37.5

a. $\alpha \approx 12$ deg

Figure 7. Vapor screen photographs, body-alone configuration (B), $M_\infty = 2.00$.

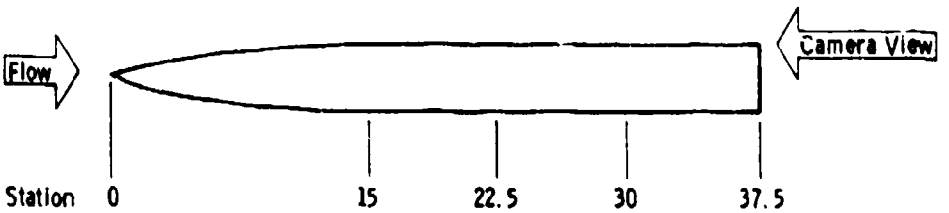

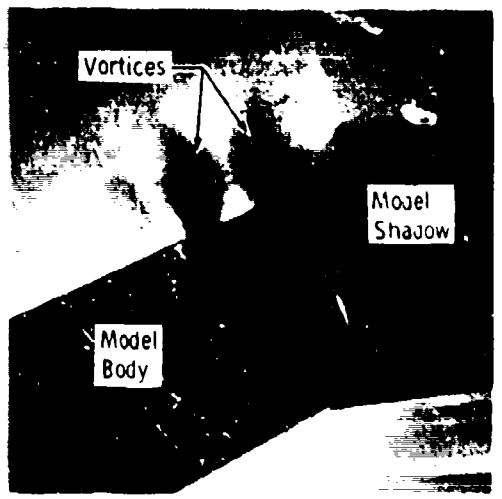

Station 15

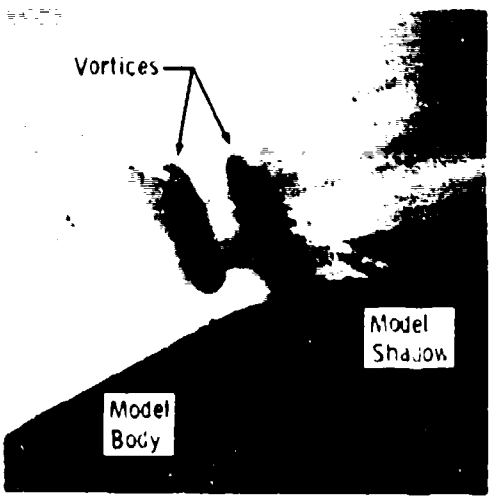

Station 22.5

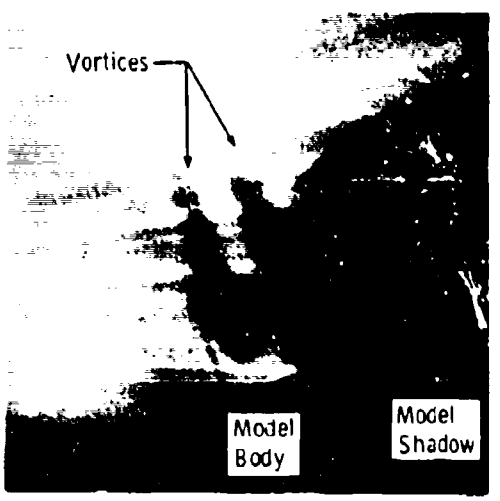

Station 30

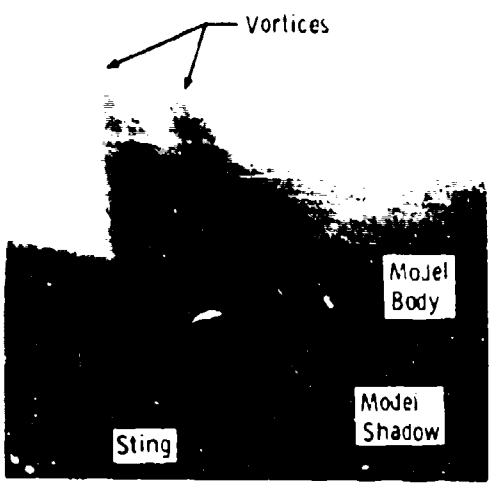

Station 37.5

b. $\alpha \approx 24$ deg

Figure 7. Concluded.

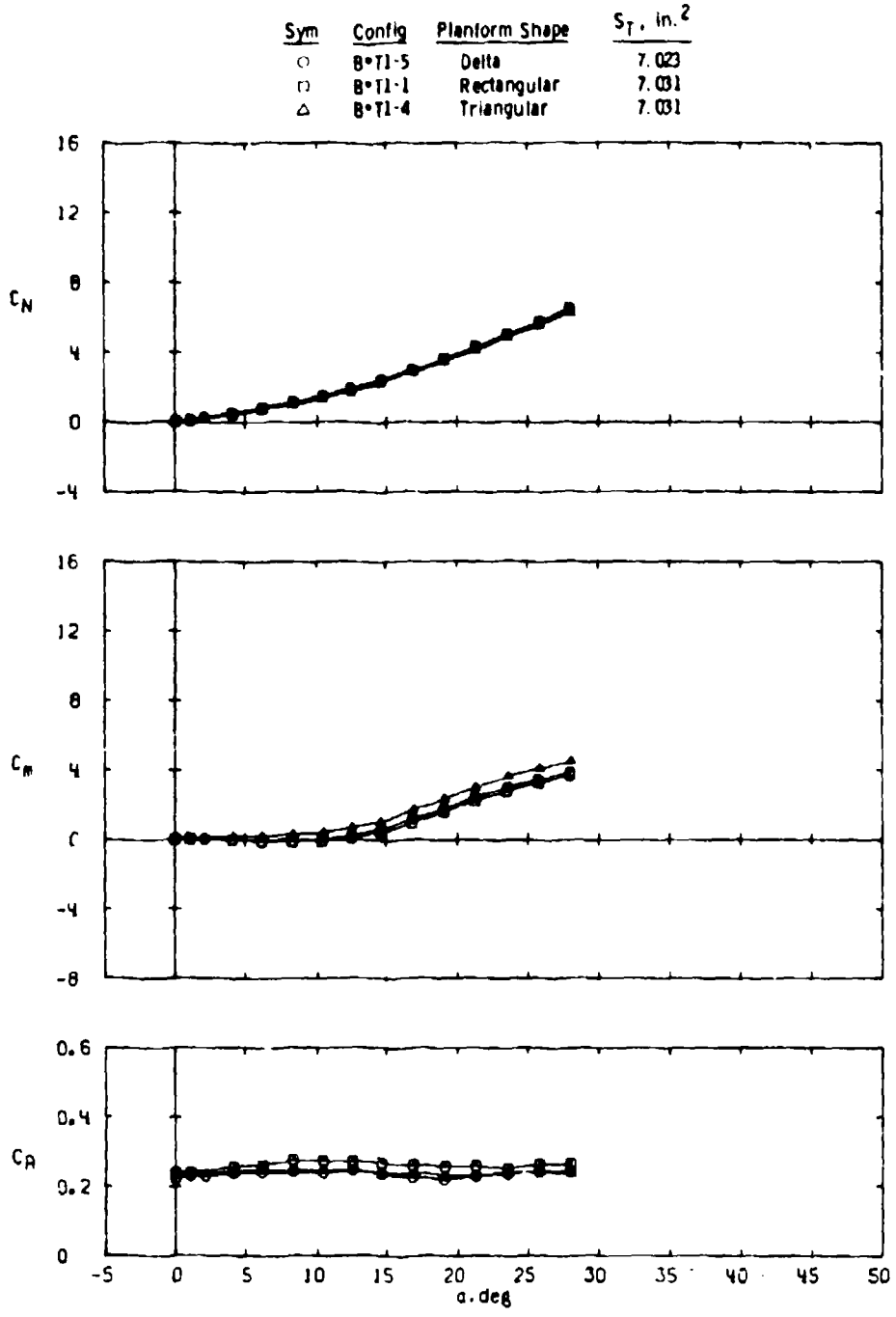

a. M_∞ = 1.76

Figure 8. Effect of fin planform shape on missile longitudinal stability and axial-force characteristics for aspect ratio 1.0 fins, ϕ = 0.

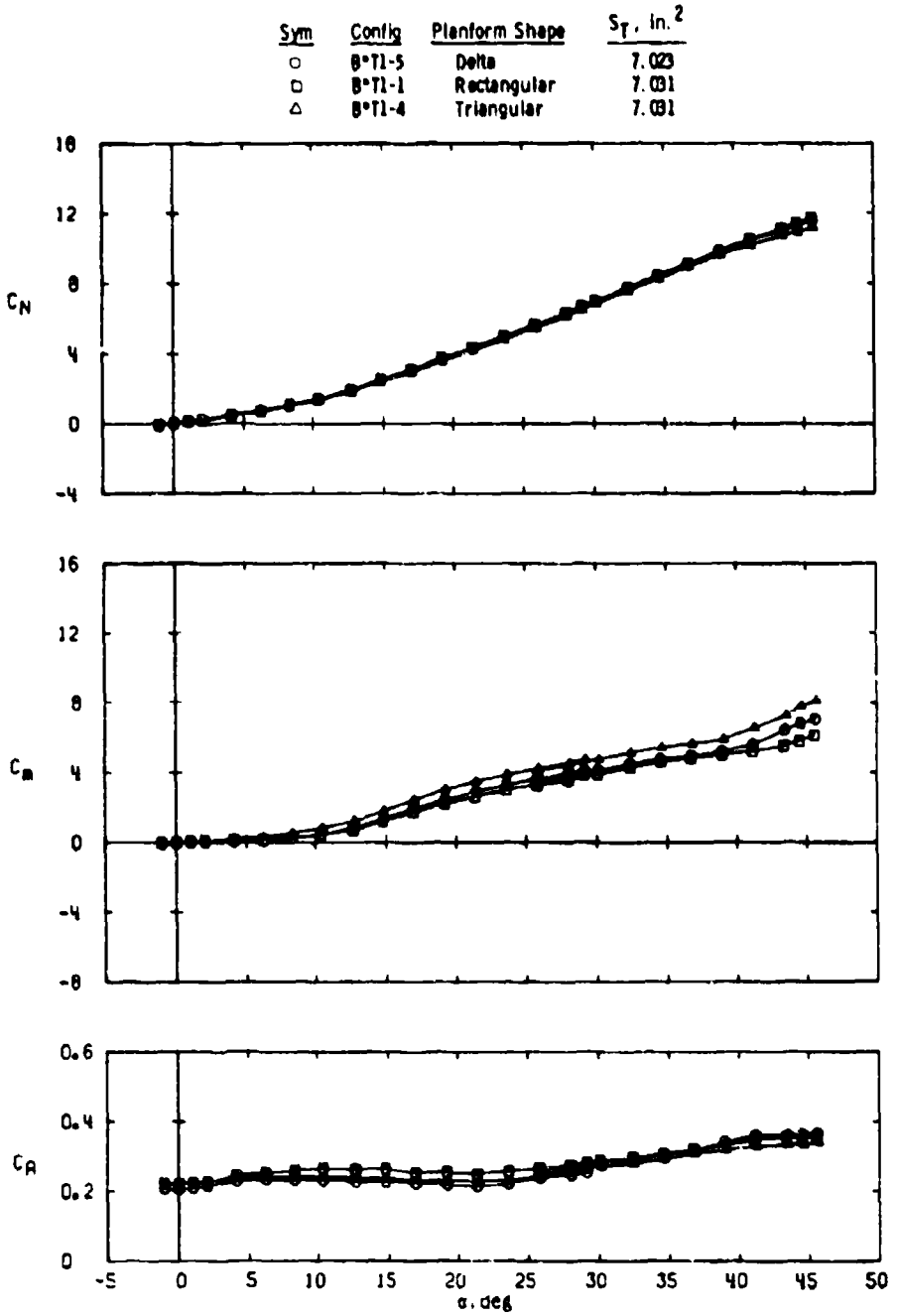

b. $M_\infty = 2.00$

Figure 8. Continued.

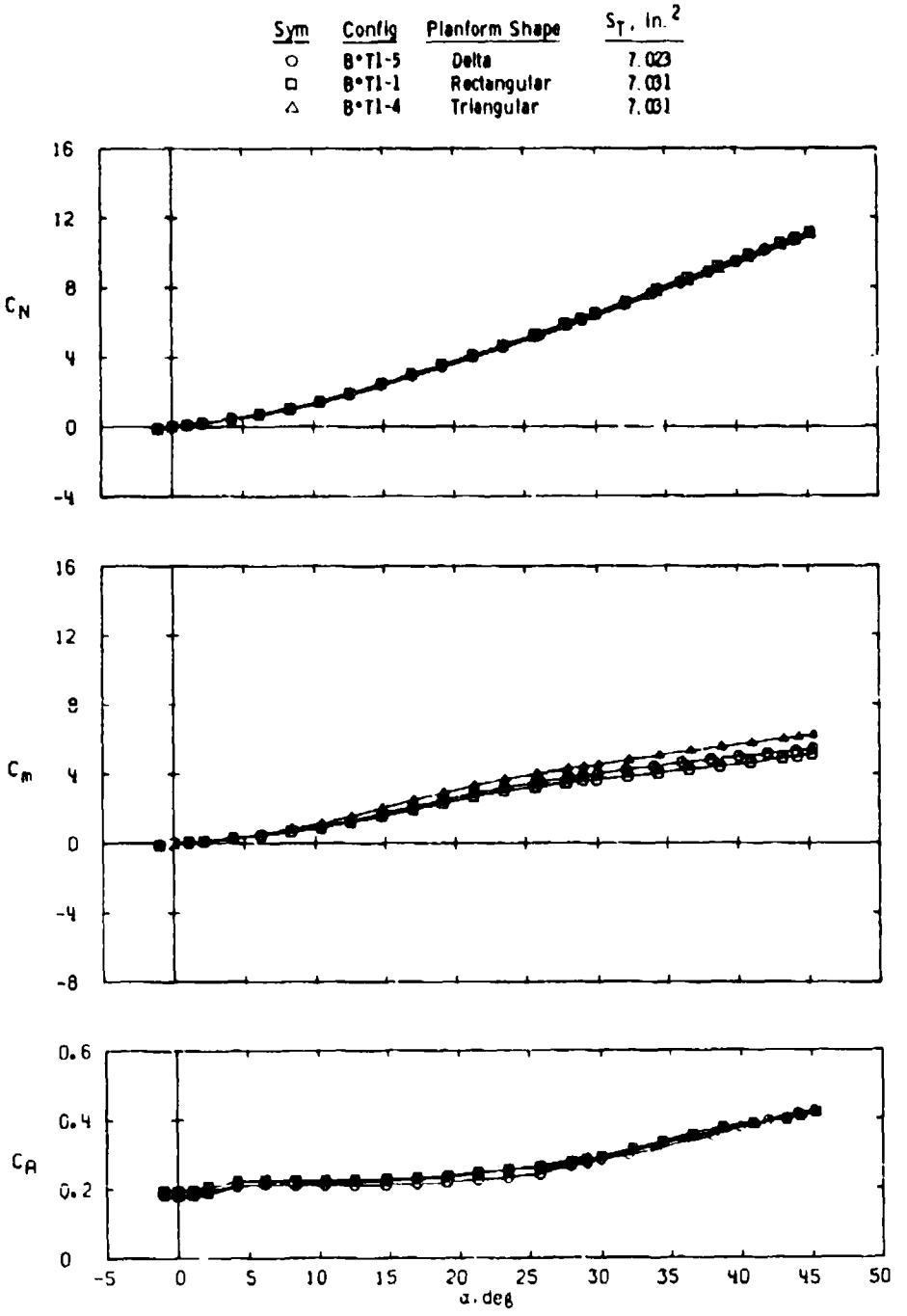

c. $M_\infty = 2.50$

Figure 8. Continued.

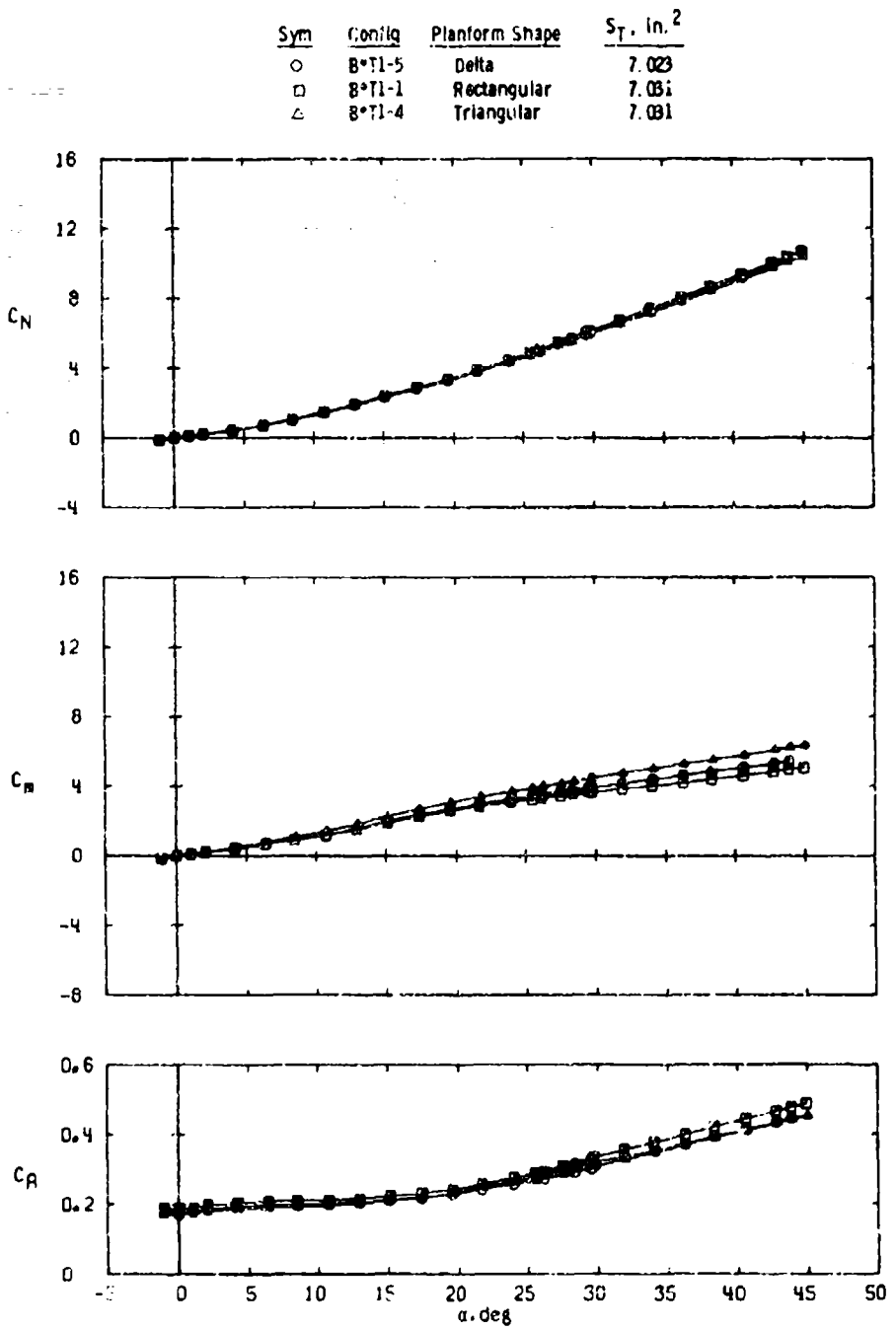

d. $M_\infty = 3.01$

Figure 8. Concluded.

Sym	Config	Planform Shape	S_T, in.^{2}
○	8°T1-5	Delta	7.023
□	8°T1-1	Rectangular	7.031
△	8°T1-4	Triangular	7.031

Data are for Fin 2.

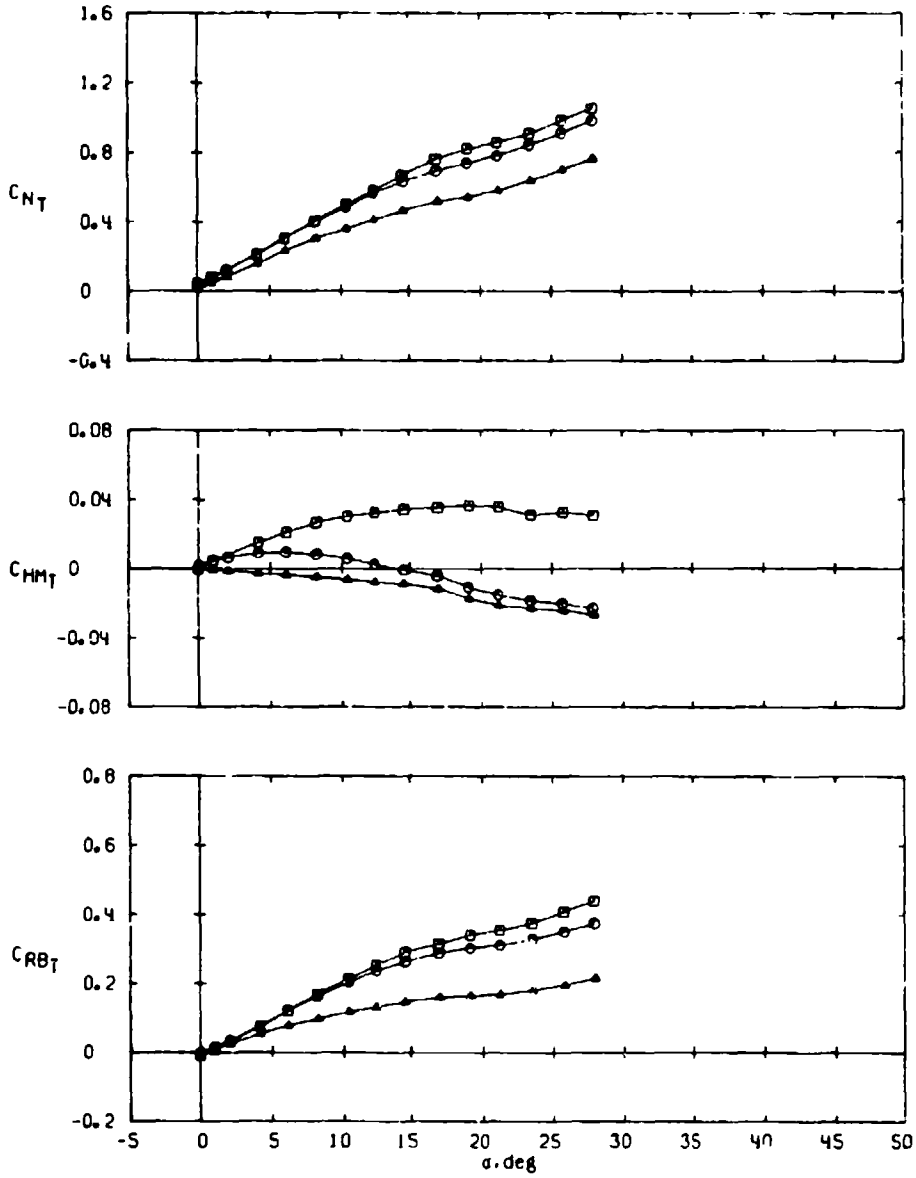

a. $M_\infty = 1.76$

Figure 9. Effect of fin planform shape on fin aerodynamic characteristics for aspect ratio 1.0 fins, $\phi = 0$.

Sym	Config	Planform Shape	S_T, in.^{2}
○	B°T1-5	Delta	7.023
□	B°T1-1	Rectangular	7.031
△	B°T1-4	Triangular	7.031

Data are for Fin 2.

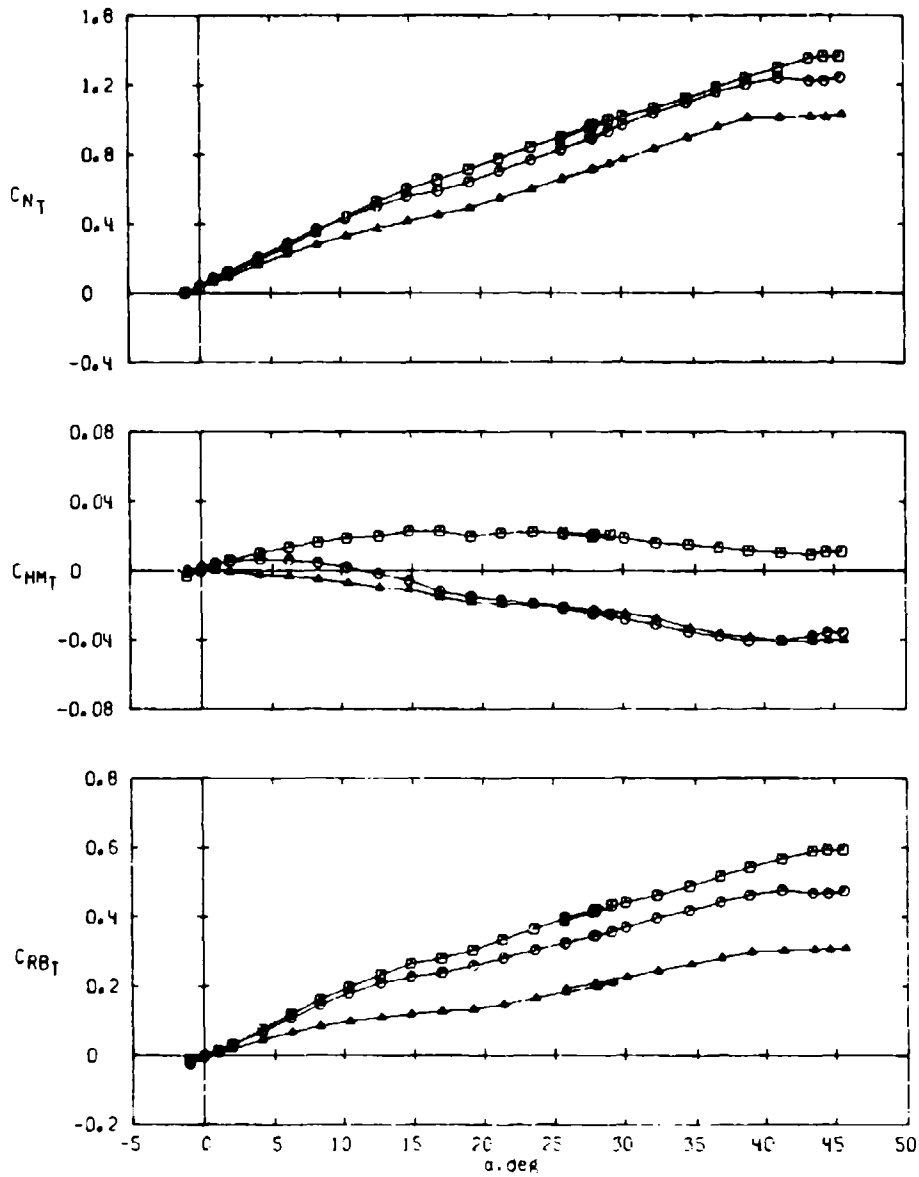

b. $M_\infty = 2.00$

Figure 9. Continued.

Sym	Config	Planform Shape	S_T, in.^{2}
○	B*T1-5	Delta	7.023
□	B*T1-1	Rectangular	7.031
△	B*T1-4	Triangular	7.031

Data are for Fin 2.

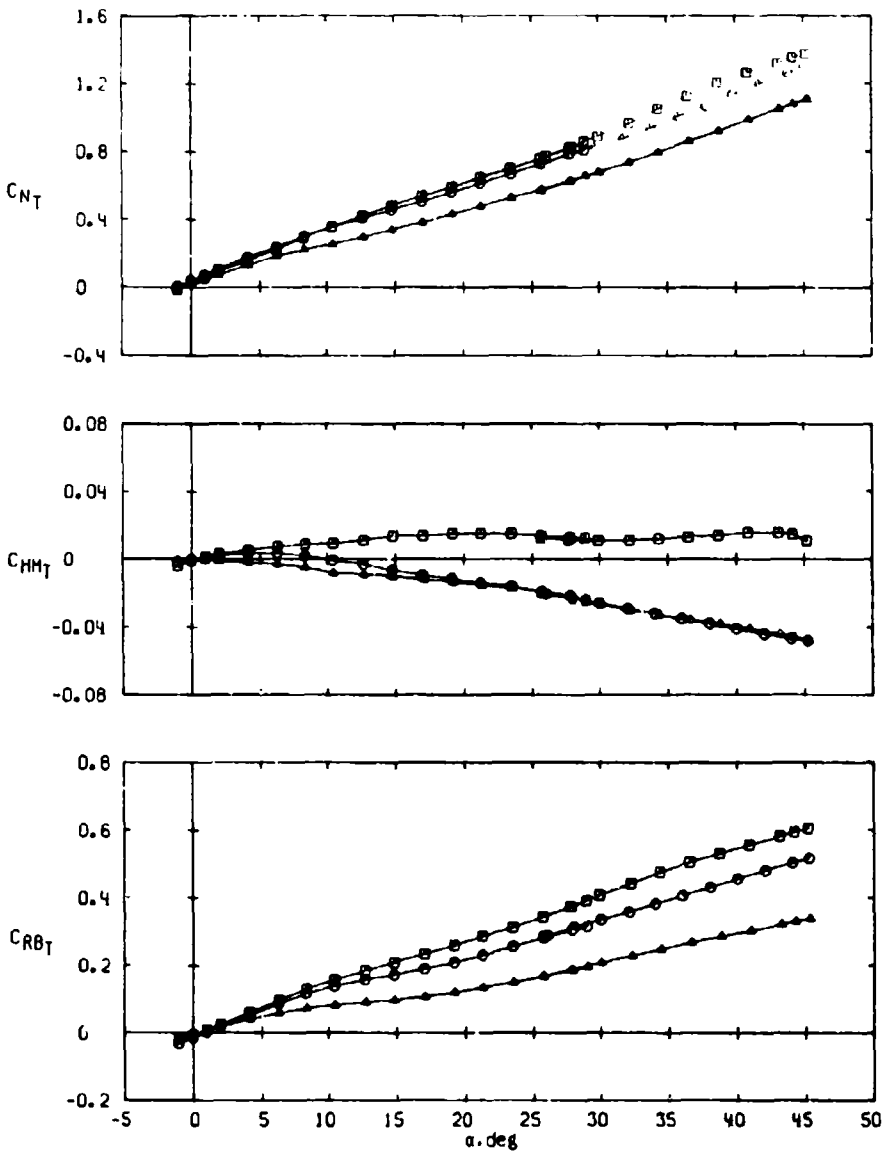

c. $M_\infty = 2.50$

Figure 9. Continued.

Sym	Config	Planform Shape	S_T, in.^{2}
○	B*T1-5	Delta	7.023
□	B*T1-1	Rectangular	7.031
△	B*T1-4	Triangular	7.031

Data are for Fin 2.

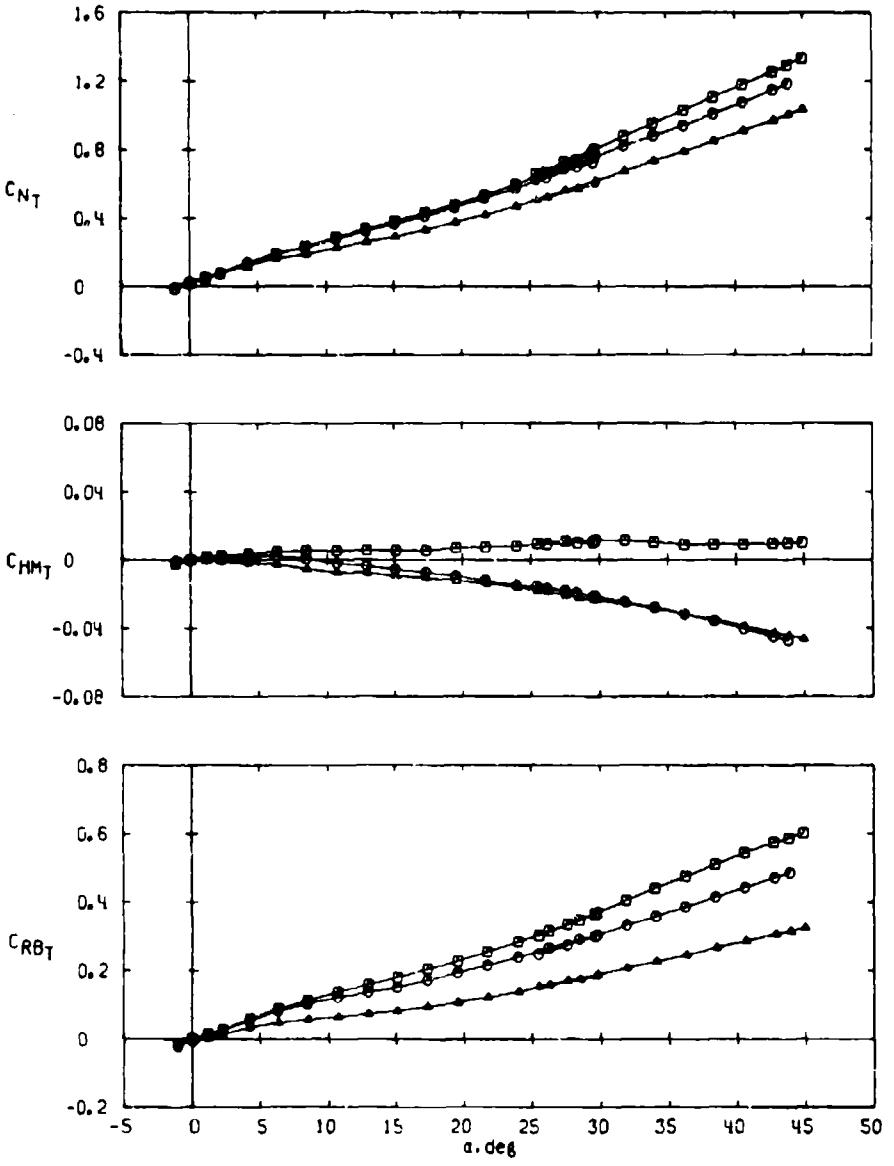

d. $M_\infty = 3.01$

Figure 9. Concluded.

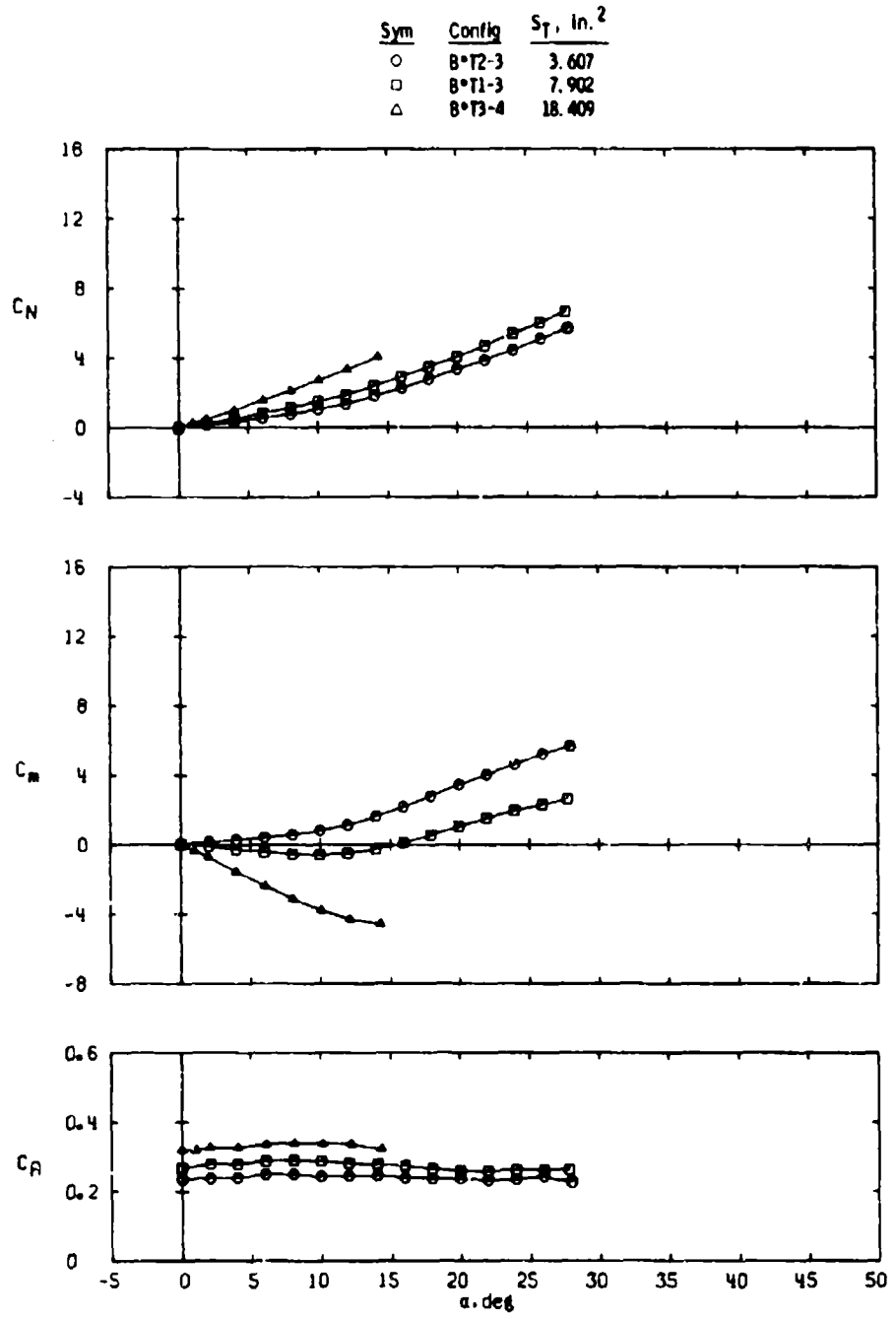

a. $M_\infty = 1.76$

Figure 10. Effect of delta fin planform area on missile longitudinal stability and axial force characteristics for aspect ratio 2.0 fins, $\phi = 0$.

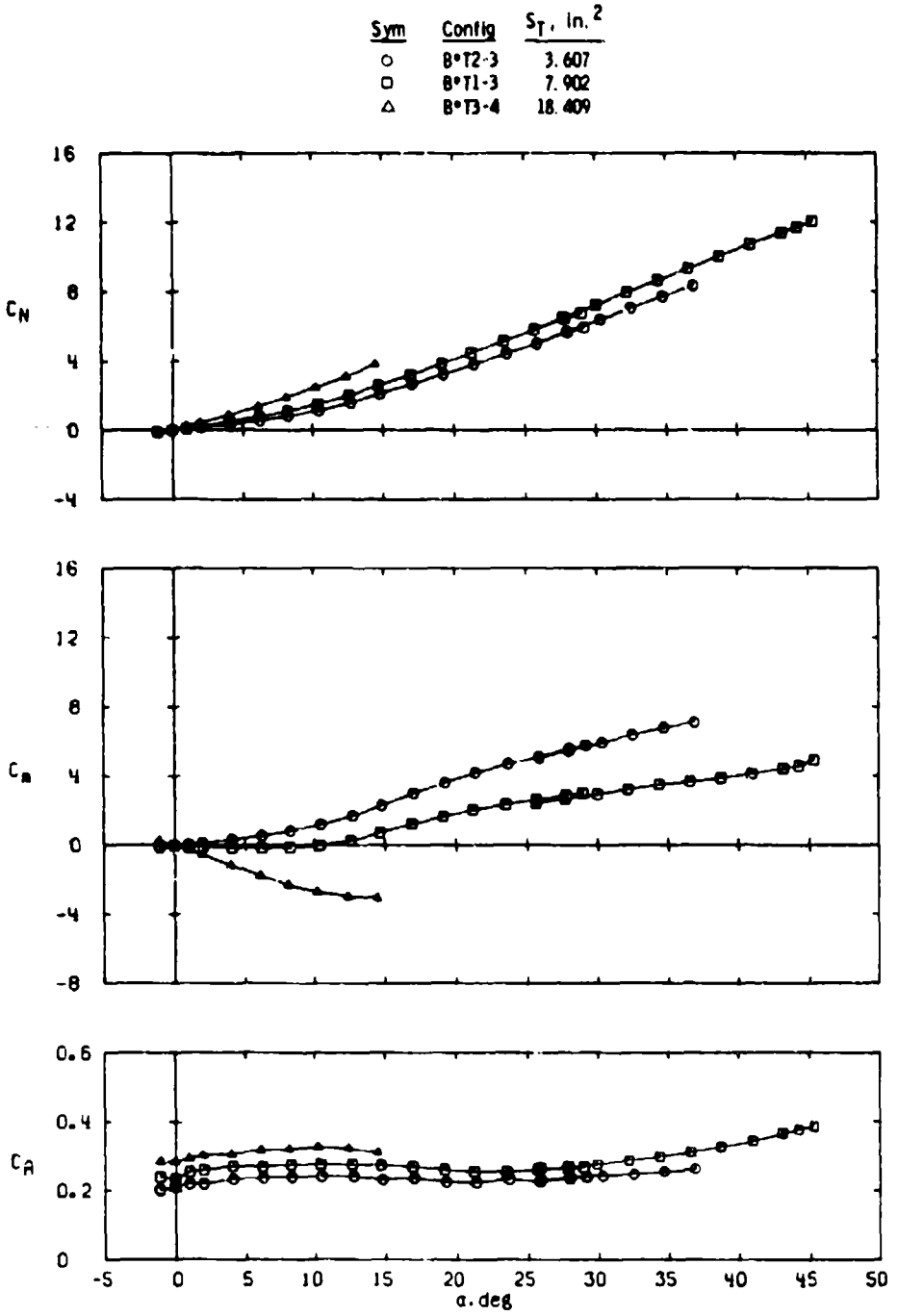

b. M_∞ = 2.00
Figure 10. Continued.

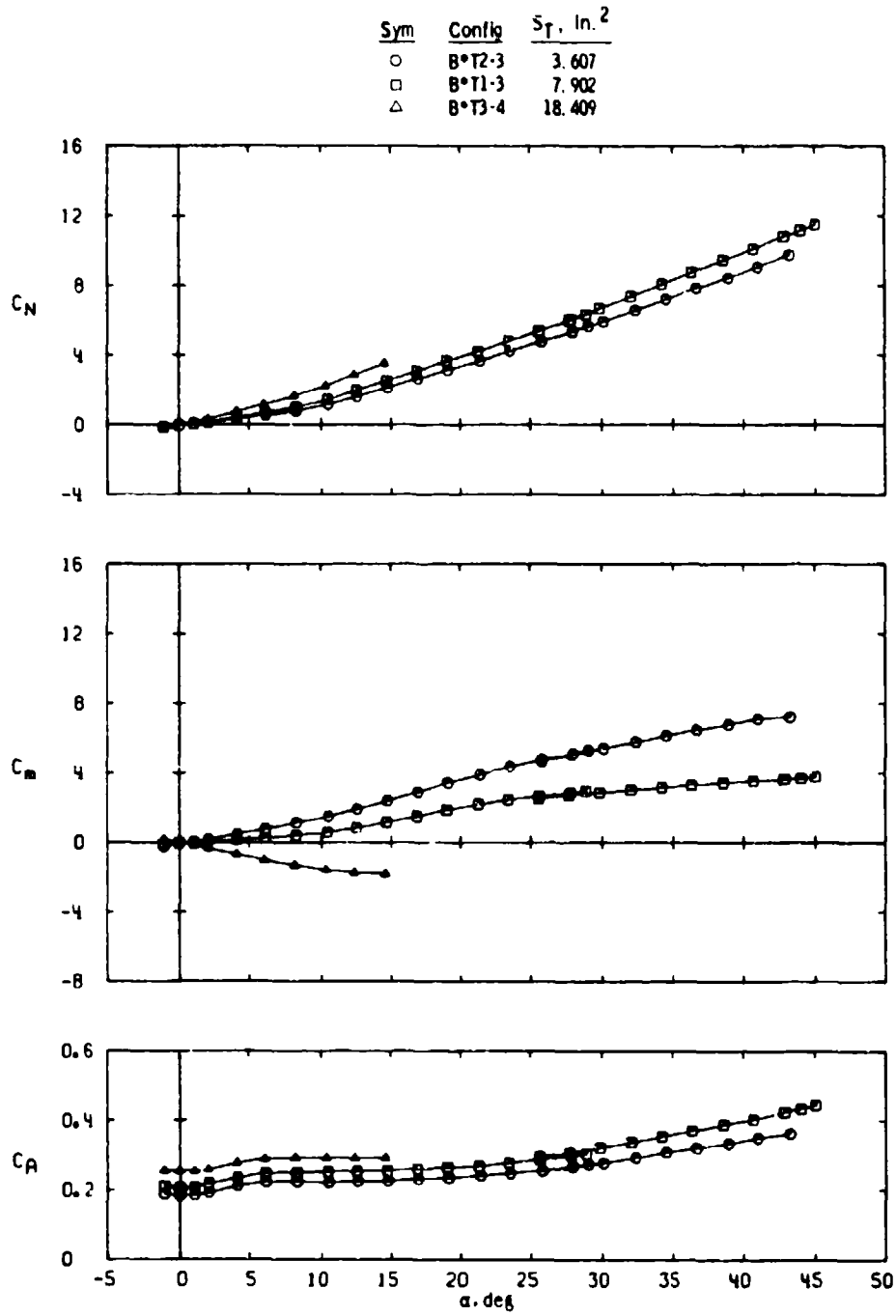

c. M_∞ = 2.50
Figure 10. Continued.

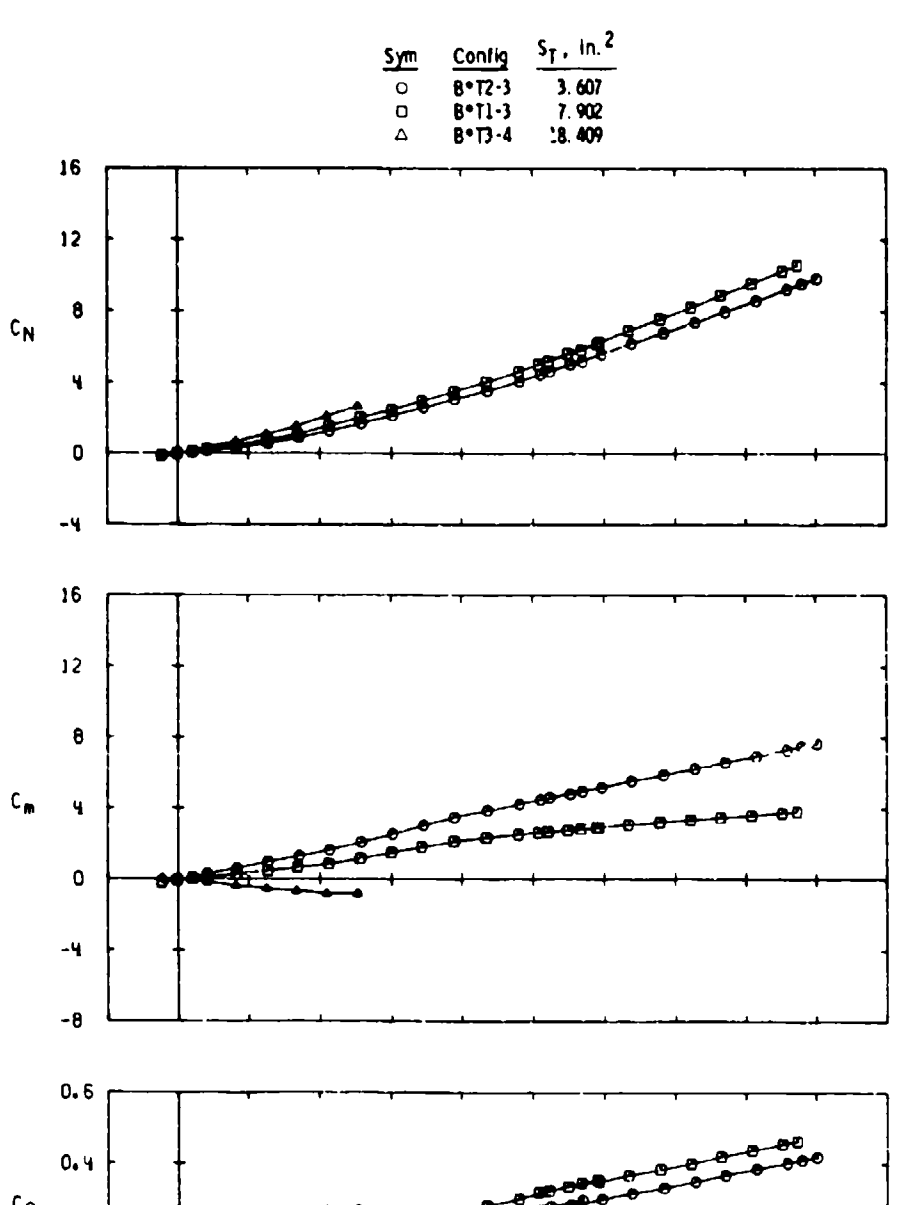

d. M_∞ = 3.01
Figure 10. Concluded.

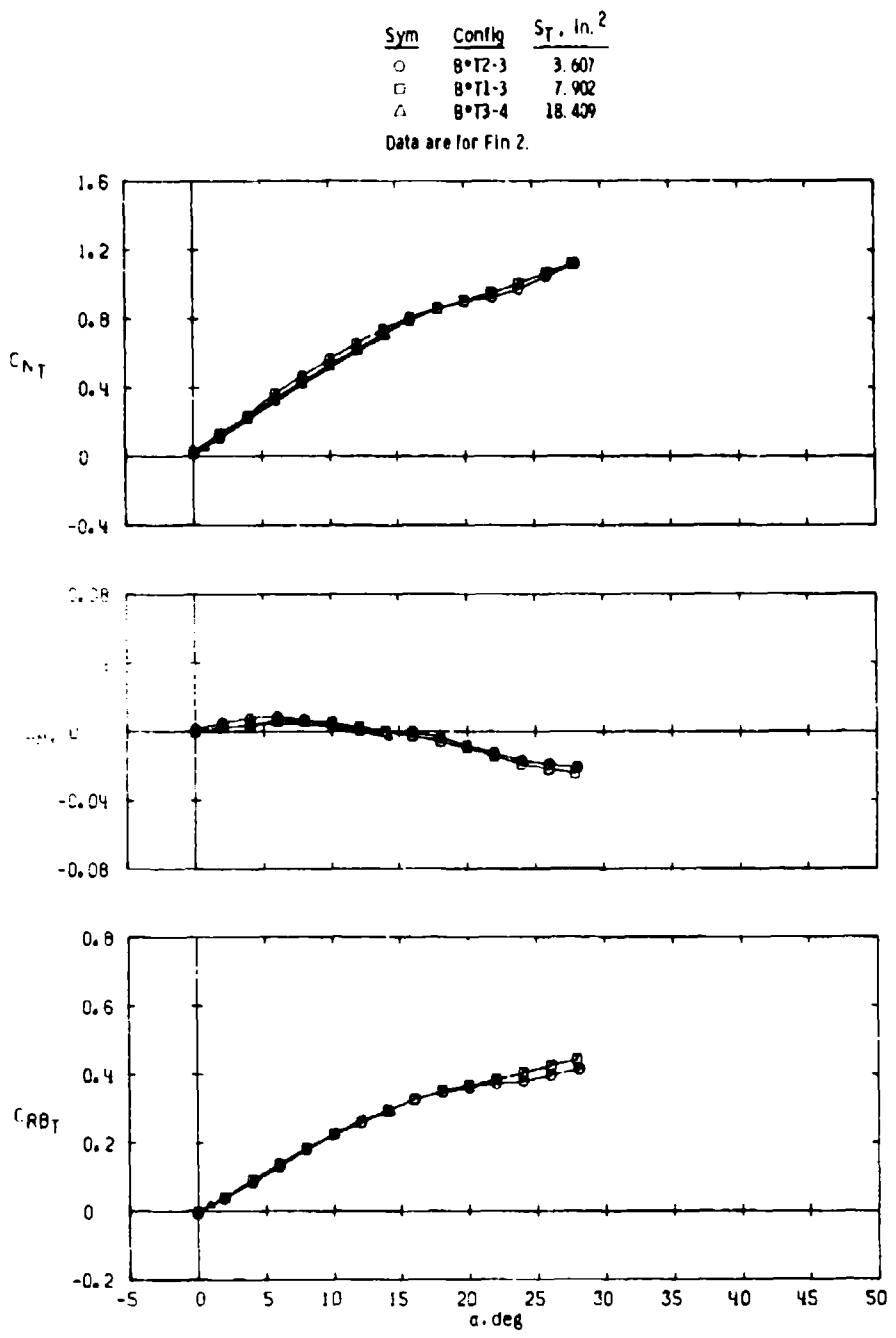

a. $M_\infty = 1.76$

Figure 11. Effect of delta fin planform area on fin aerodynamic characteristics for aspect ratio 2.0 fins, $\varphi = 0$.

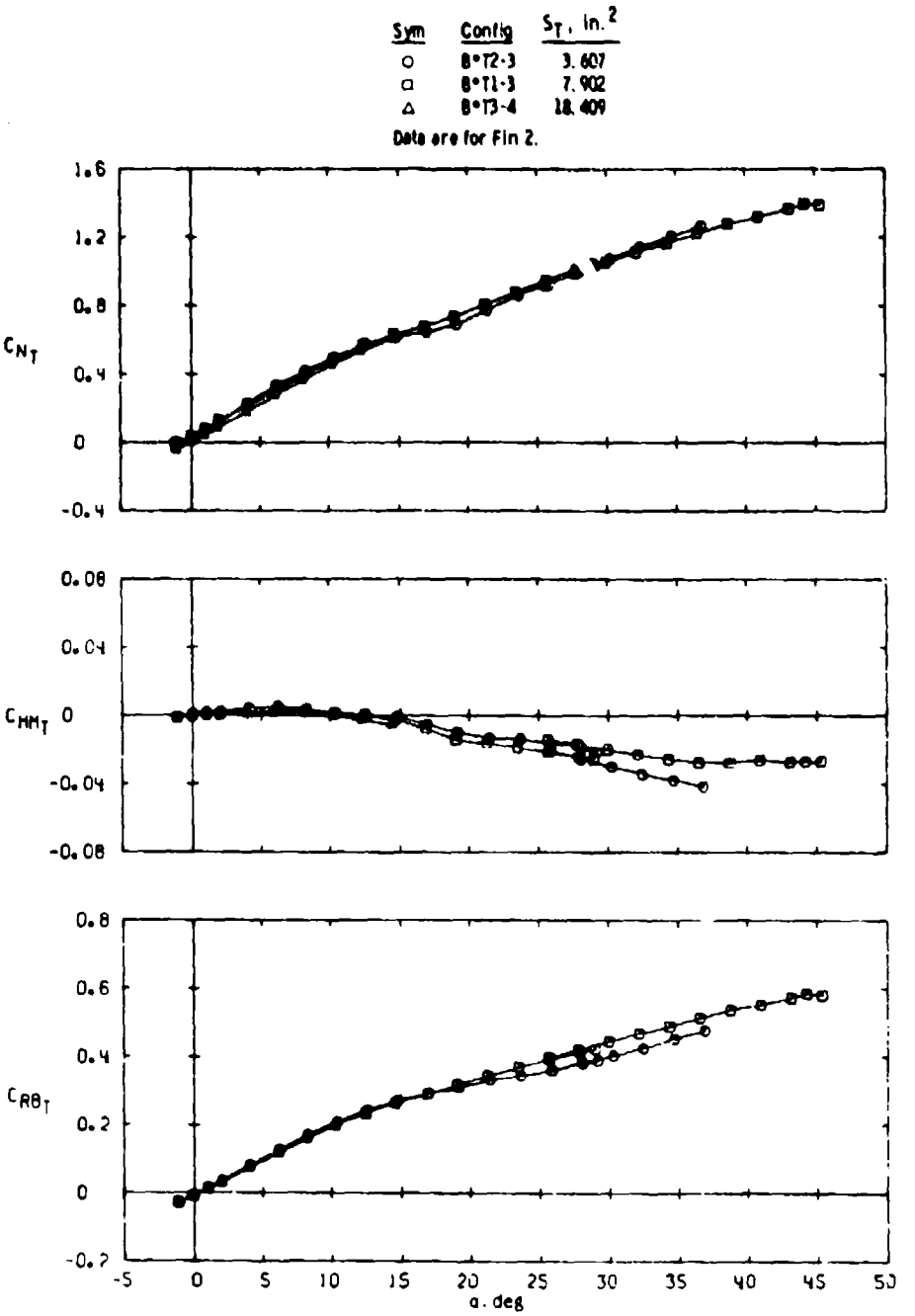

b. M_∞ = 2.00
Figure 11. Continued.

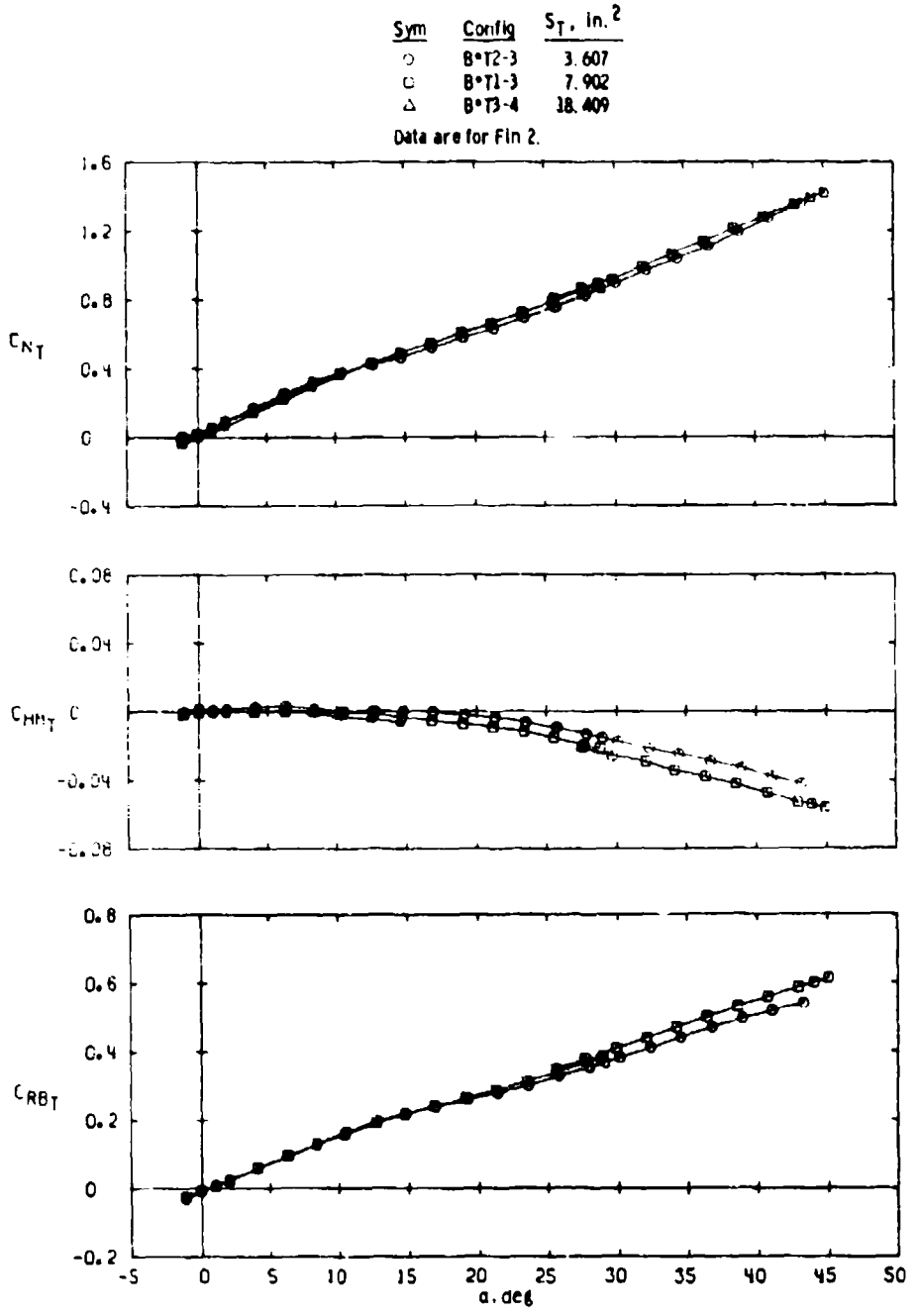

c. M_∞ = 2.50
Figure 11. Continued.

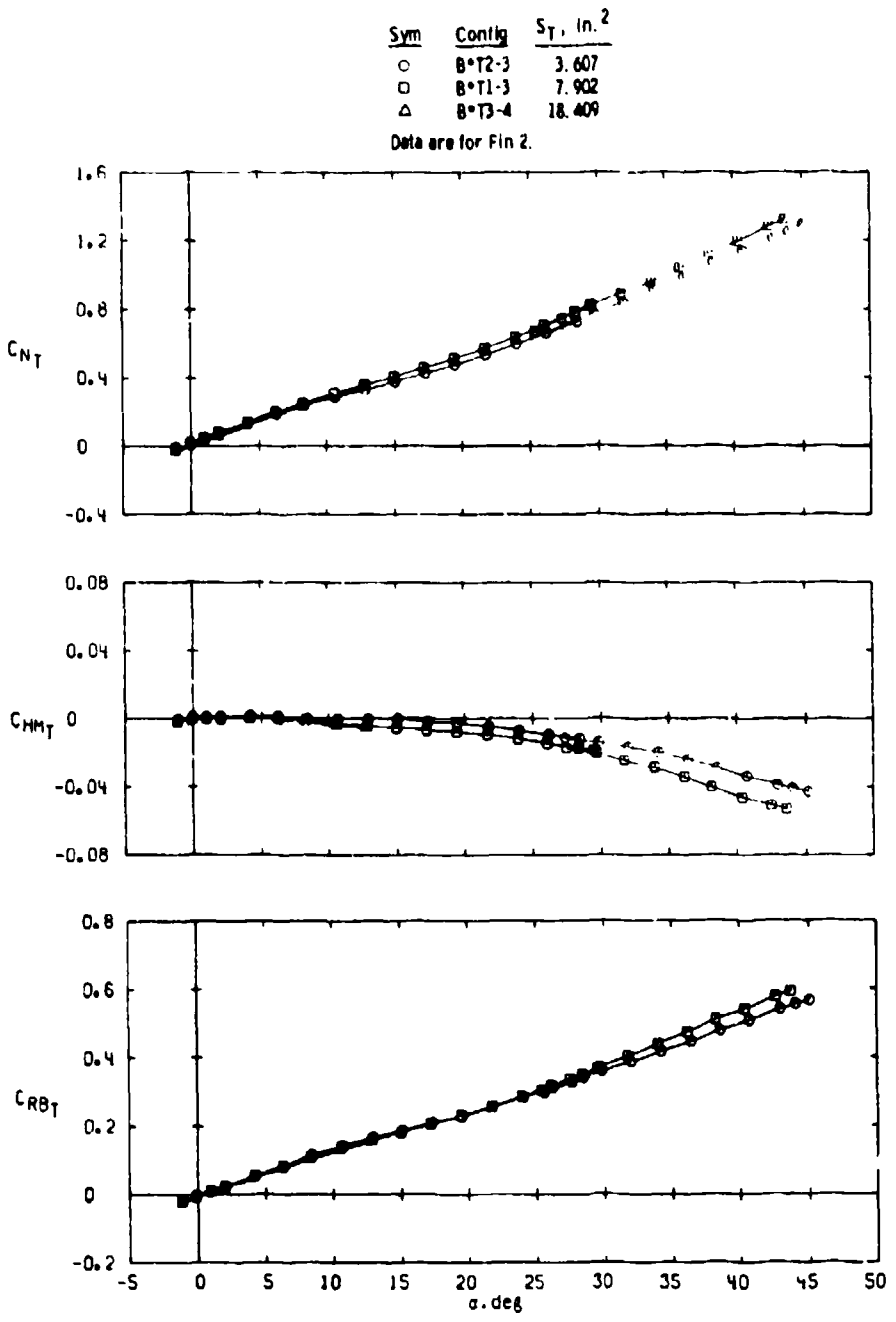

d. M_∞ = 3.01
Figure 11. Concluded.

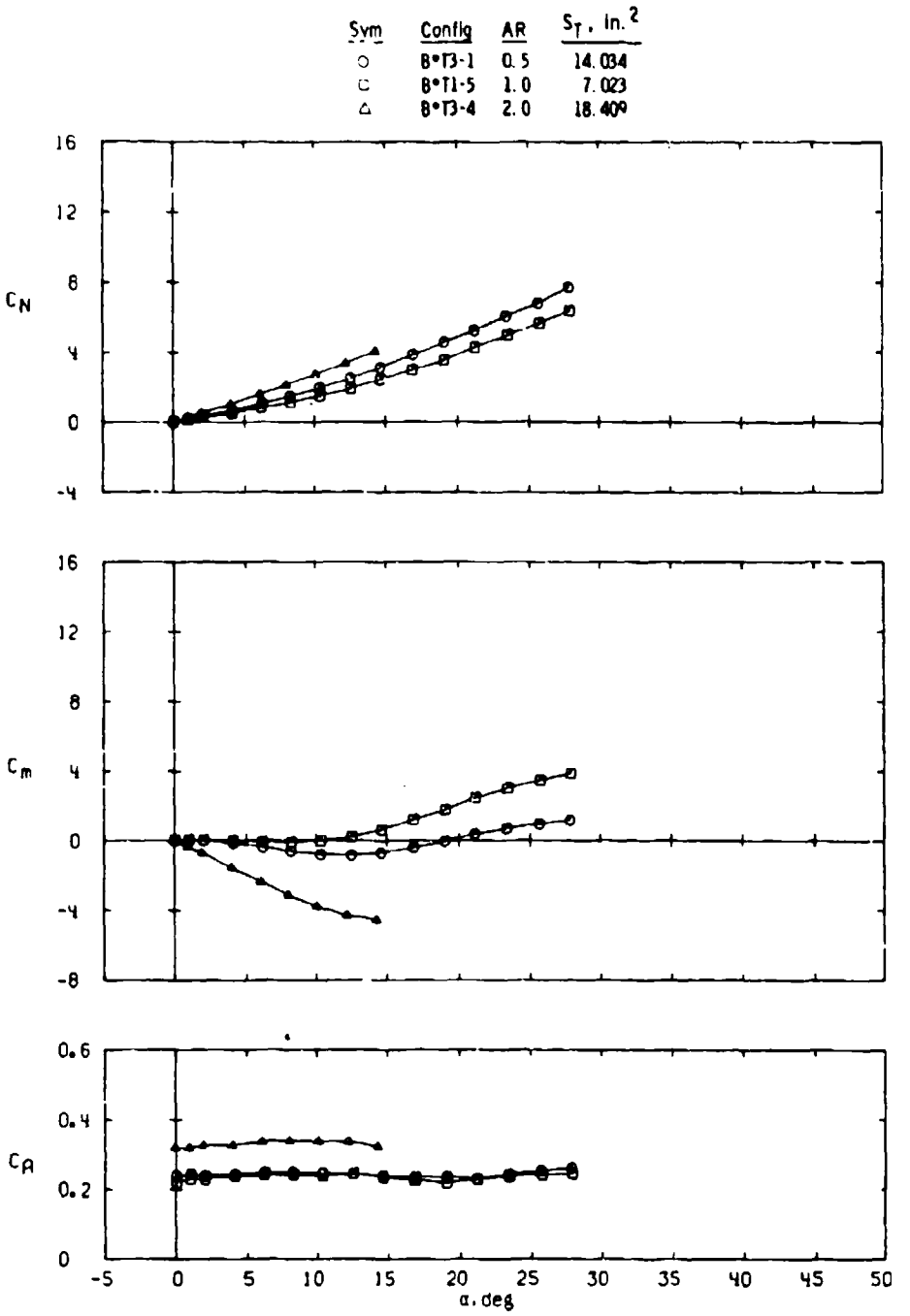

a. $M_\infty = 1.76$

Figure 12. Effect of delta fin aspect ratio on missile longitudinal stability and axial-force characteristics, $\phi = 0$.

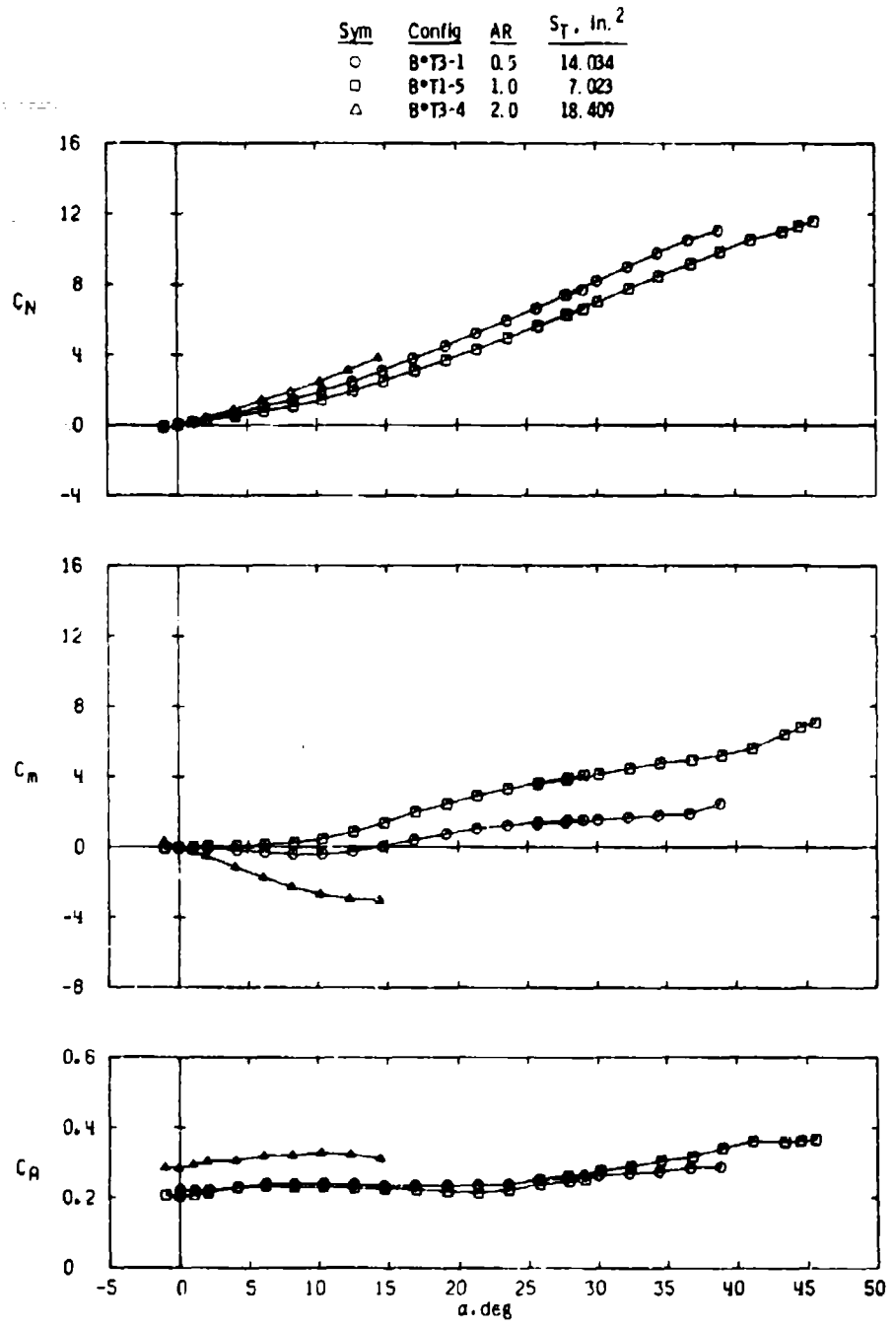

b. $M_\infty = 2.00$

Figure 12. Continued.

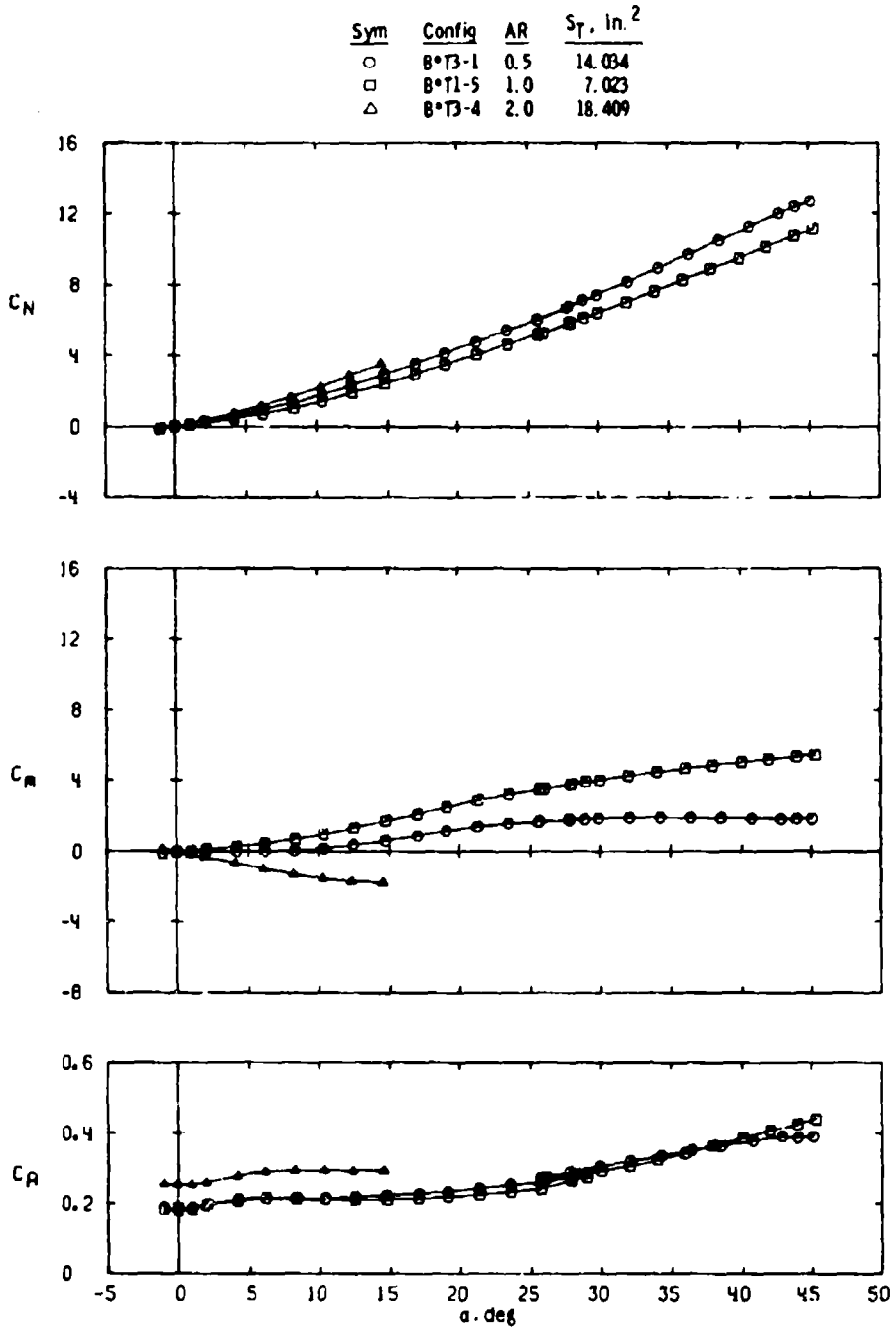

c. M_∞ = 2.50
Figure 12. Continued.

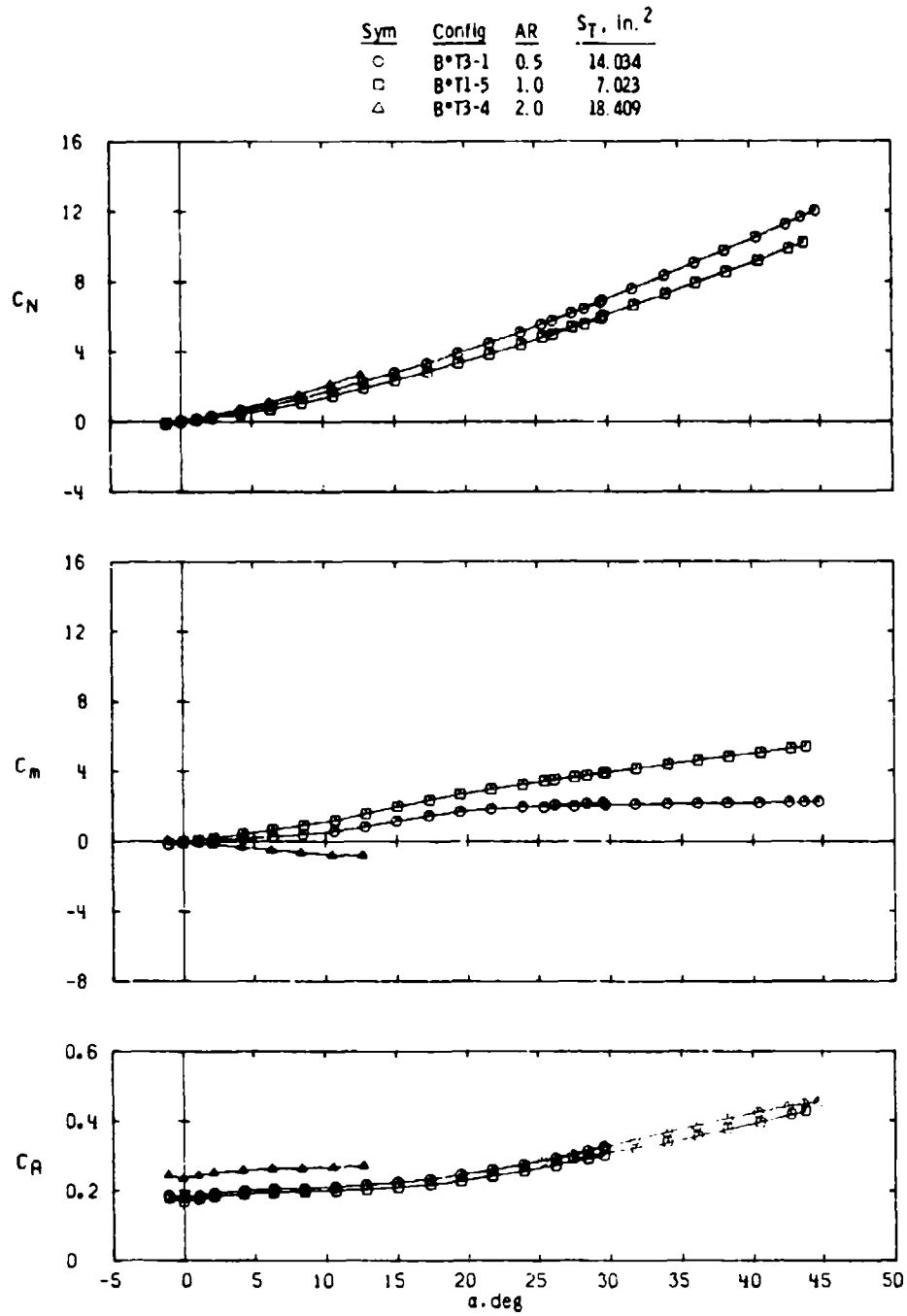

d. M_∞ = 3.01

Figure 12. Concluded.

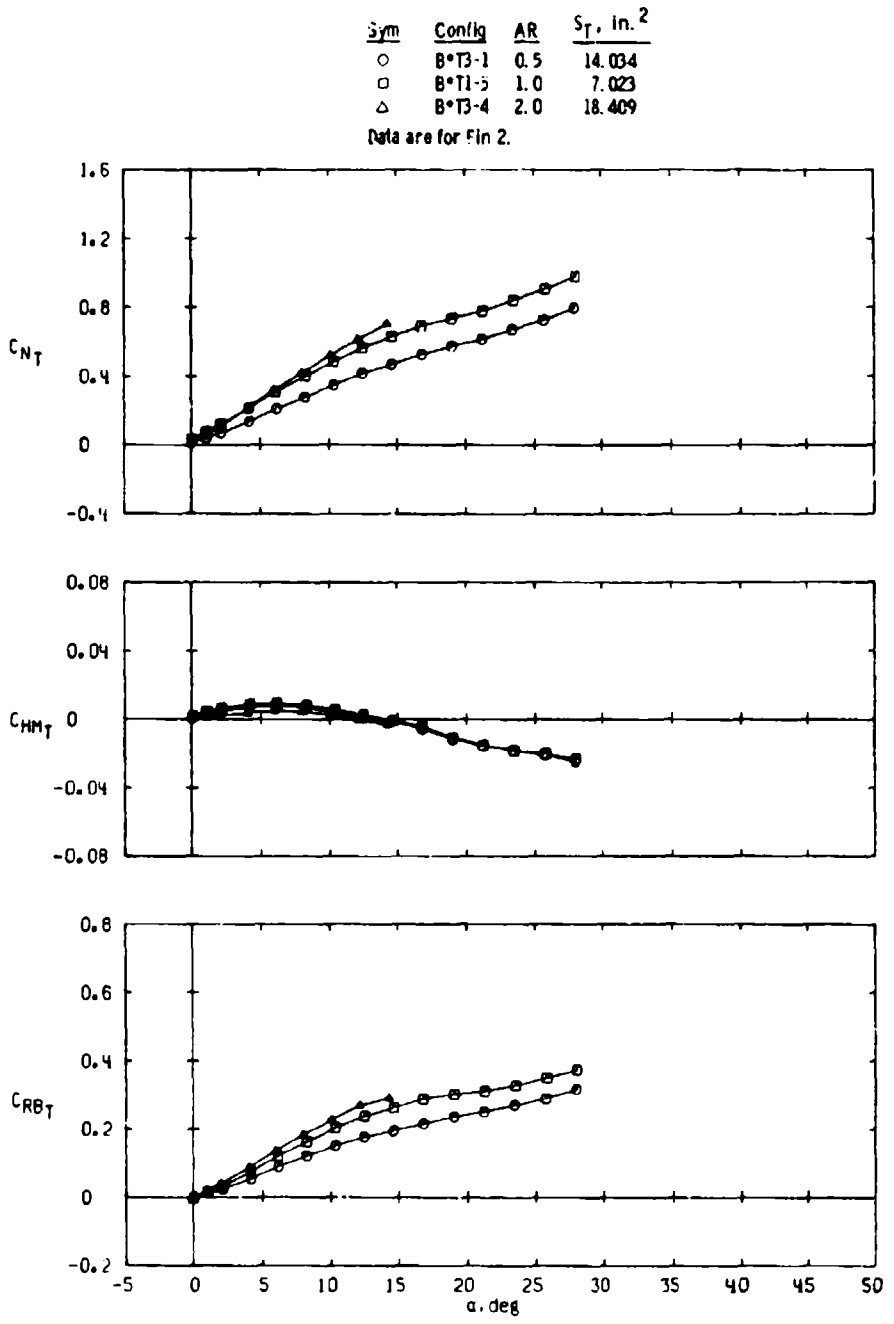

a. $M_\infty = 1.76$

Figure 13. Effect of delta fin aspect ratio on fin aerodynamic characteristics, $\phi = 0$.

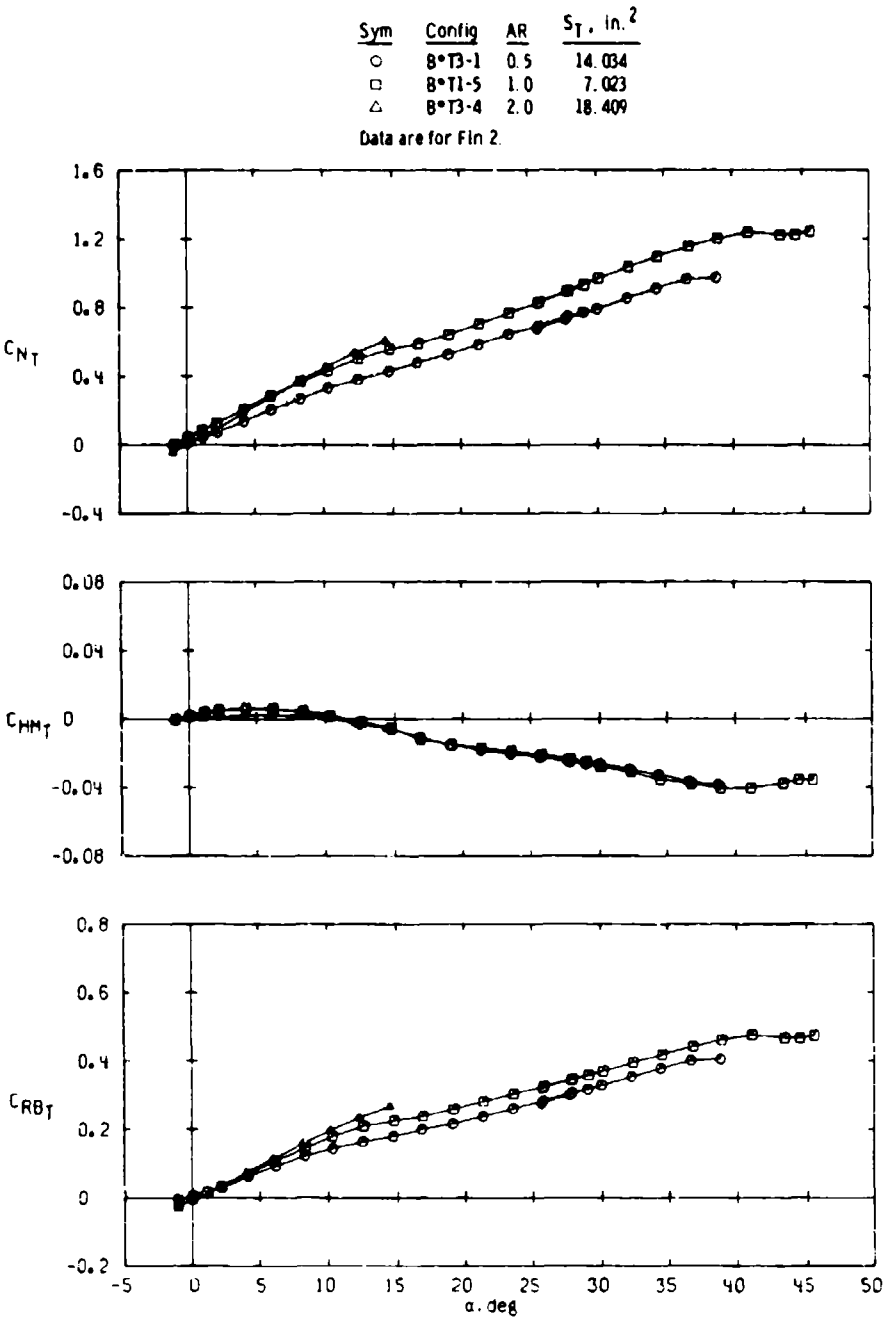

b. M_∞ = 2.00
Figure 13. Continued.

Sym	Config	AR	S_T, in.^{2}
○	B*T3-1	0.5	14.034
□	B*T1-5	1.0	7.023
△	B*T3-4	2.0	18.409

Data are for Fin 2.

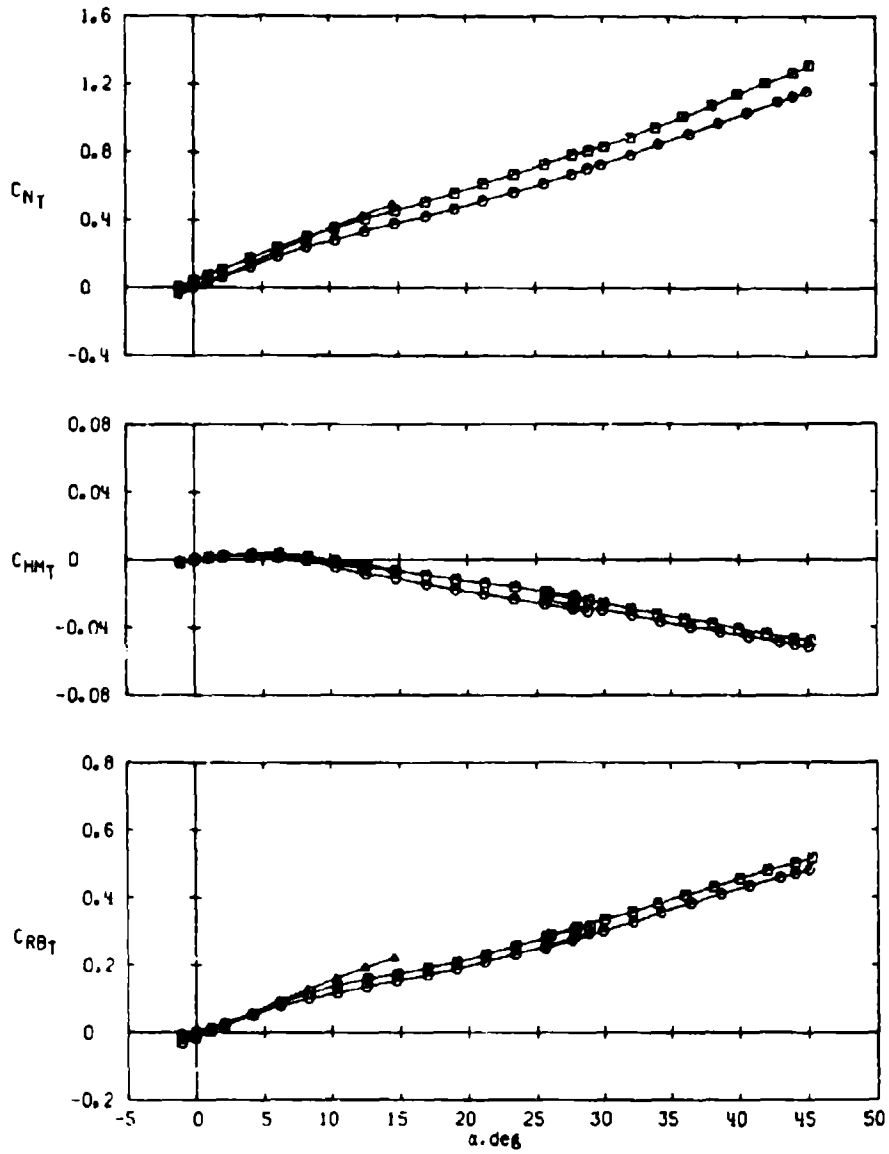

c. M_∞ = 2.50

Figure 13. Continued.

Sym	Config	AR	S_T, in.^{2}
○	B*T3-1	0.5	14.034
□	B*T1-5	1.0	7.023
△	B*T3-4	2.0	18.409

Data are for Fin 2.

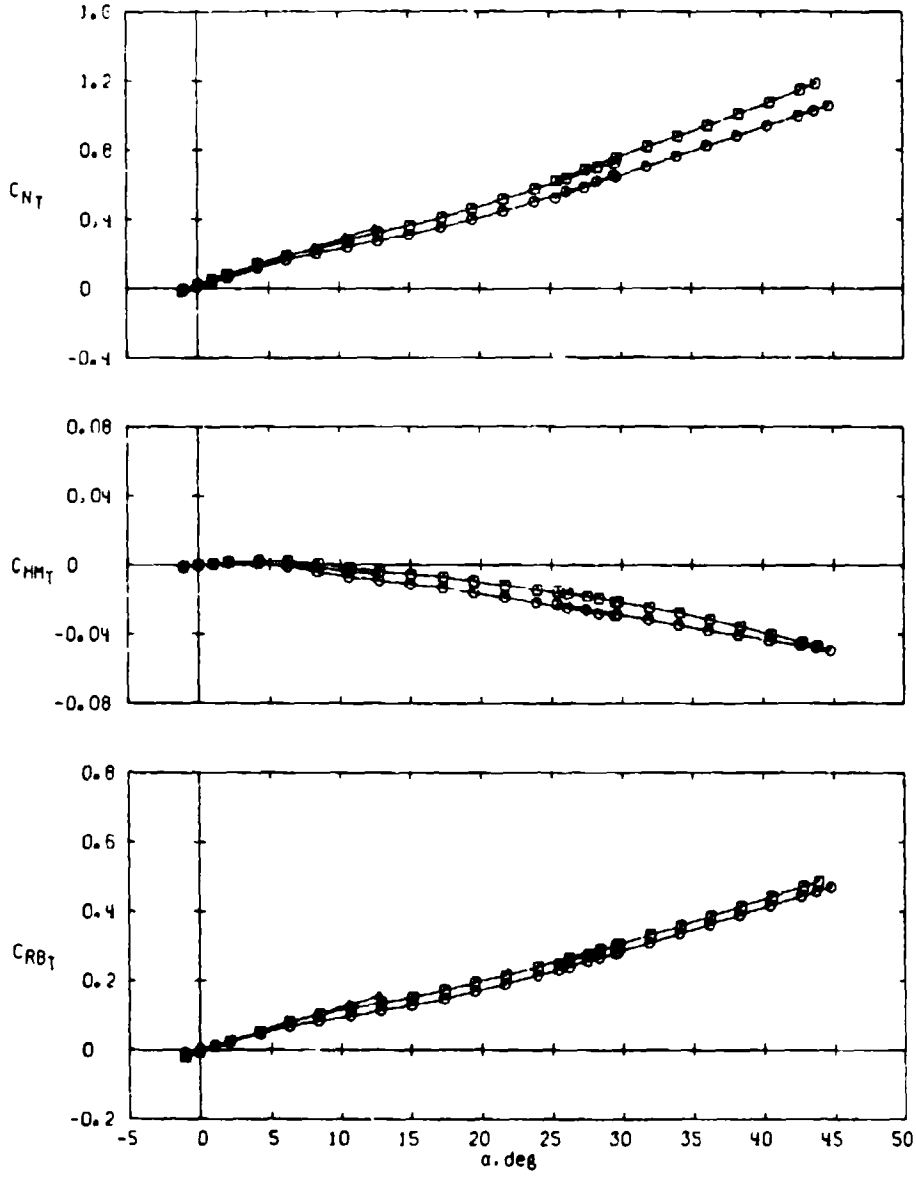

d. $M_\infty = 3.01$

Figure 13. Concluded.

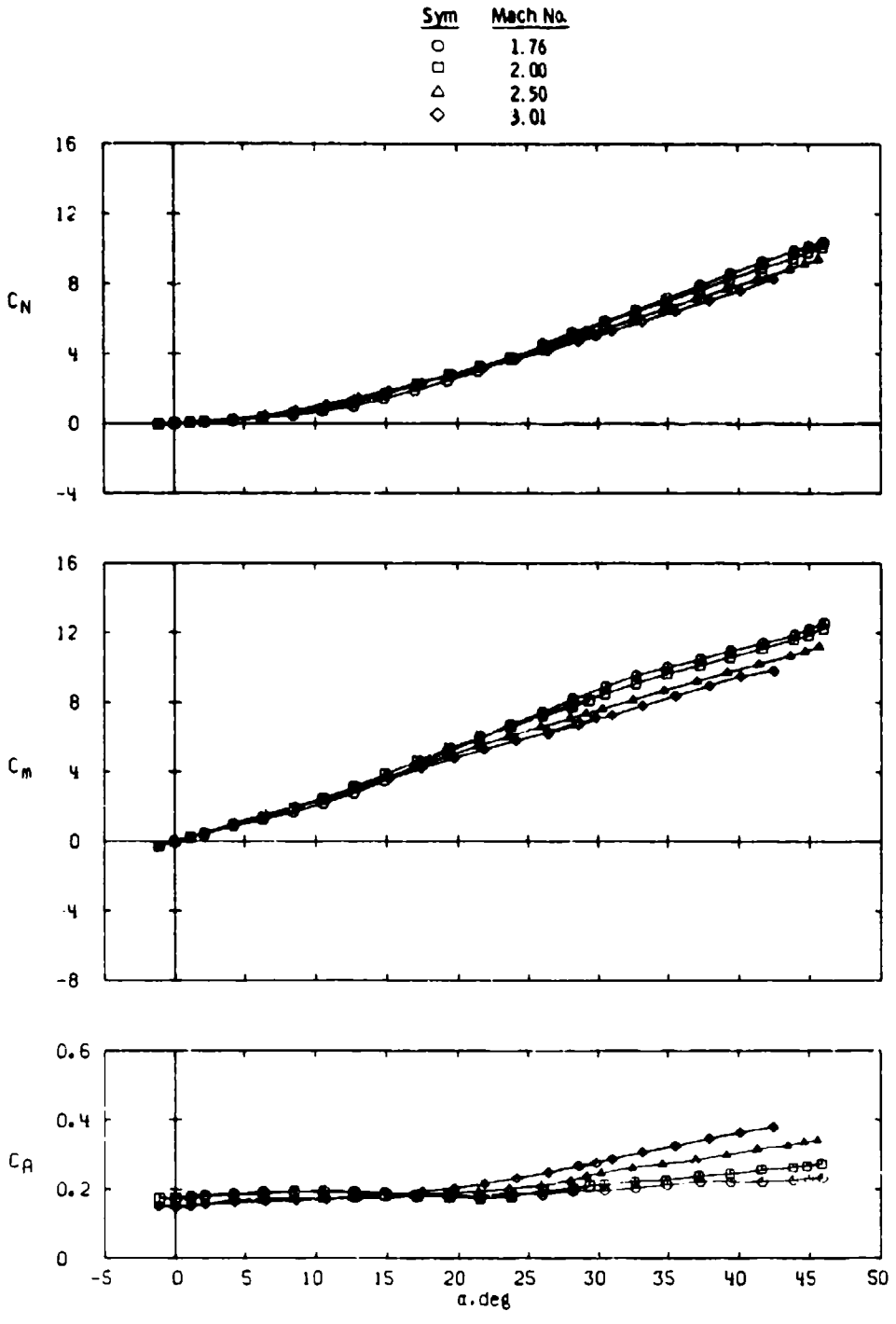

a. Configuration B

Figure 14. Effect of Mach number on missile longitudinal stability and axial-force characteristics, ϕ = 0.

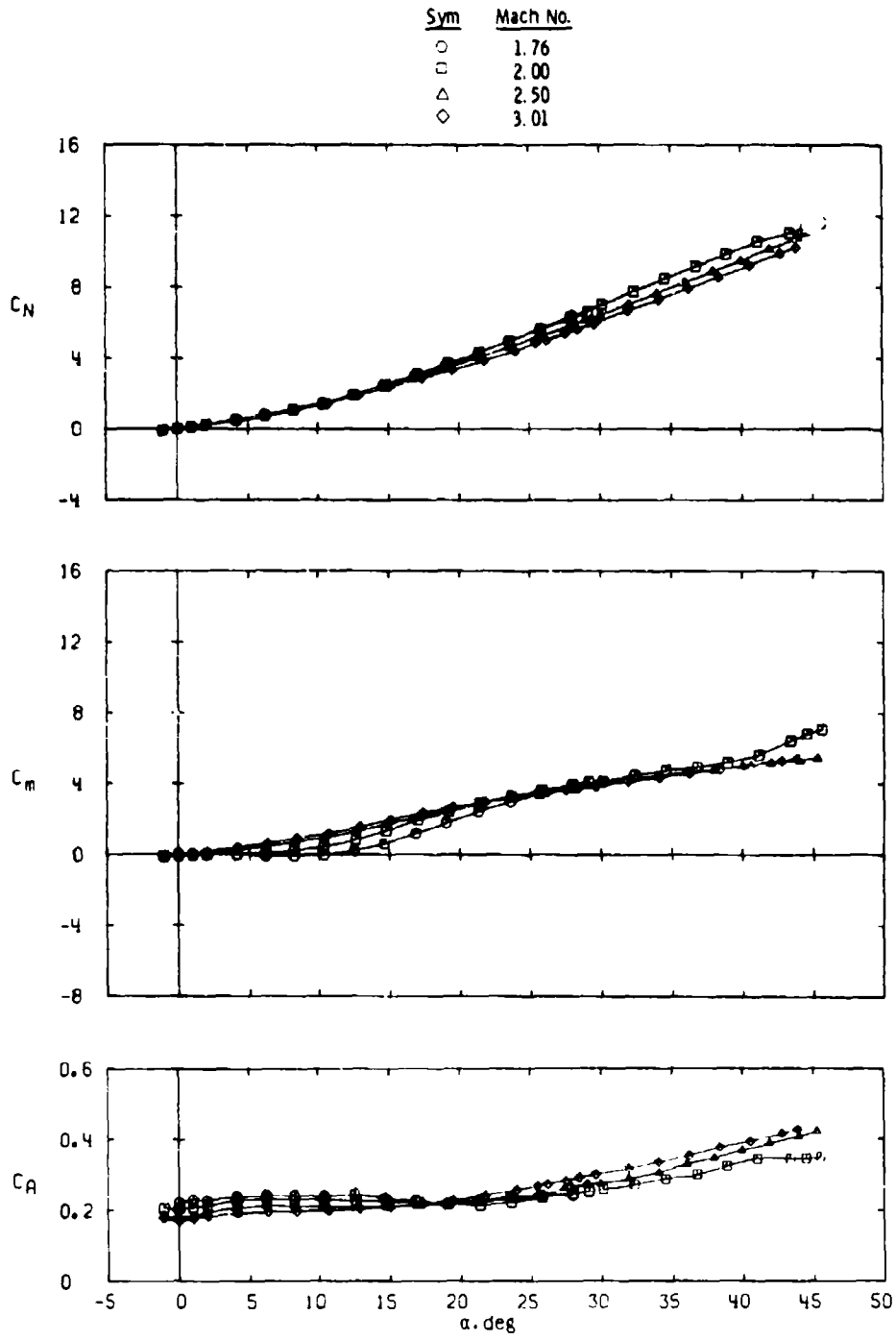

b. Configuration B*T1-5, delta fin, AR = 1.0, S_T = 7.023 in.^{2}
Figure 14 Continued.

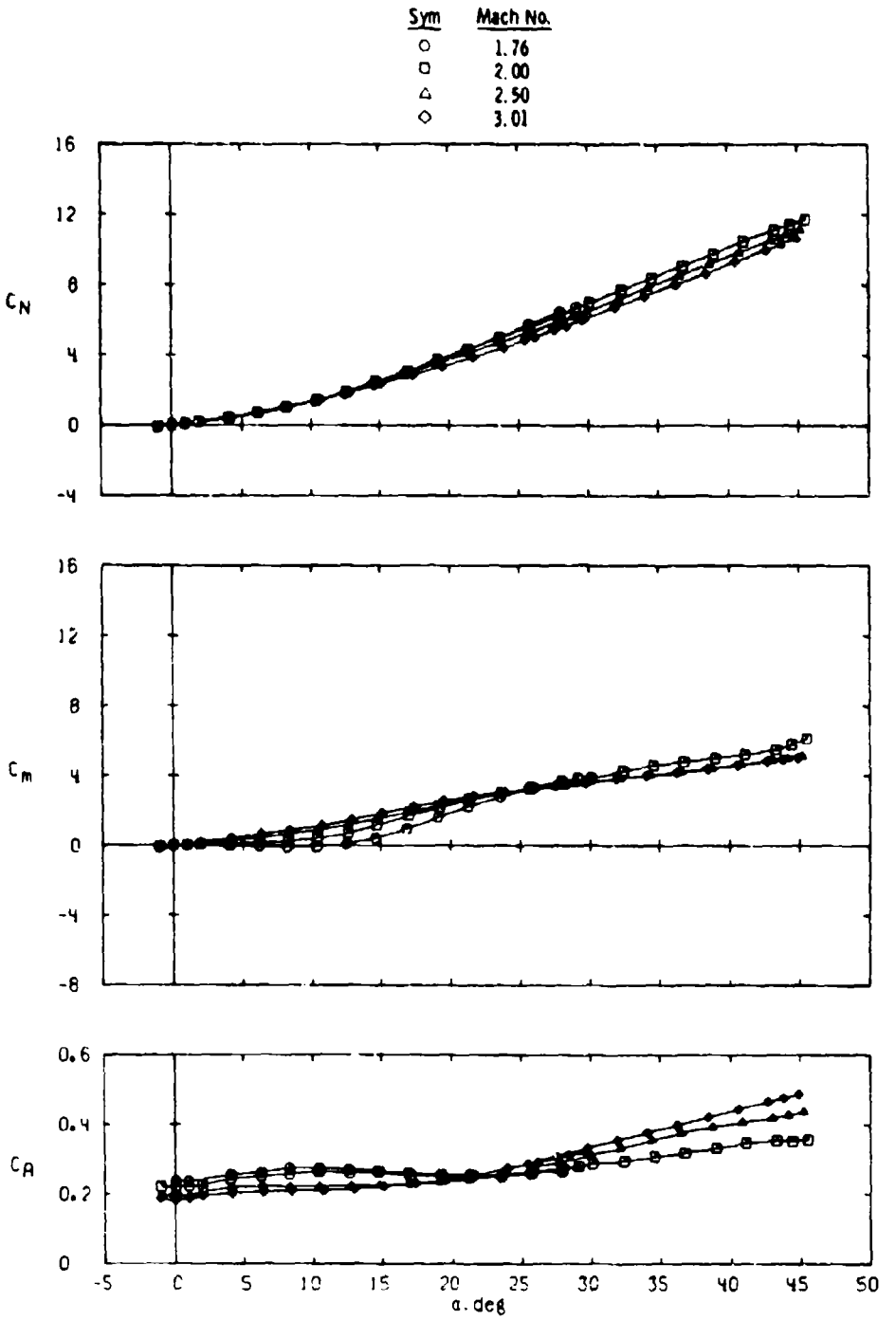

c. Configuration B*T1-1, rectangular fin, AR = 1.0, S_T = 7.031 in.^{2}
Figure 14. Continued.

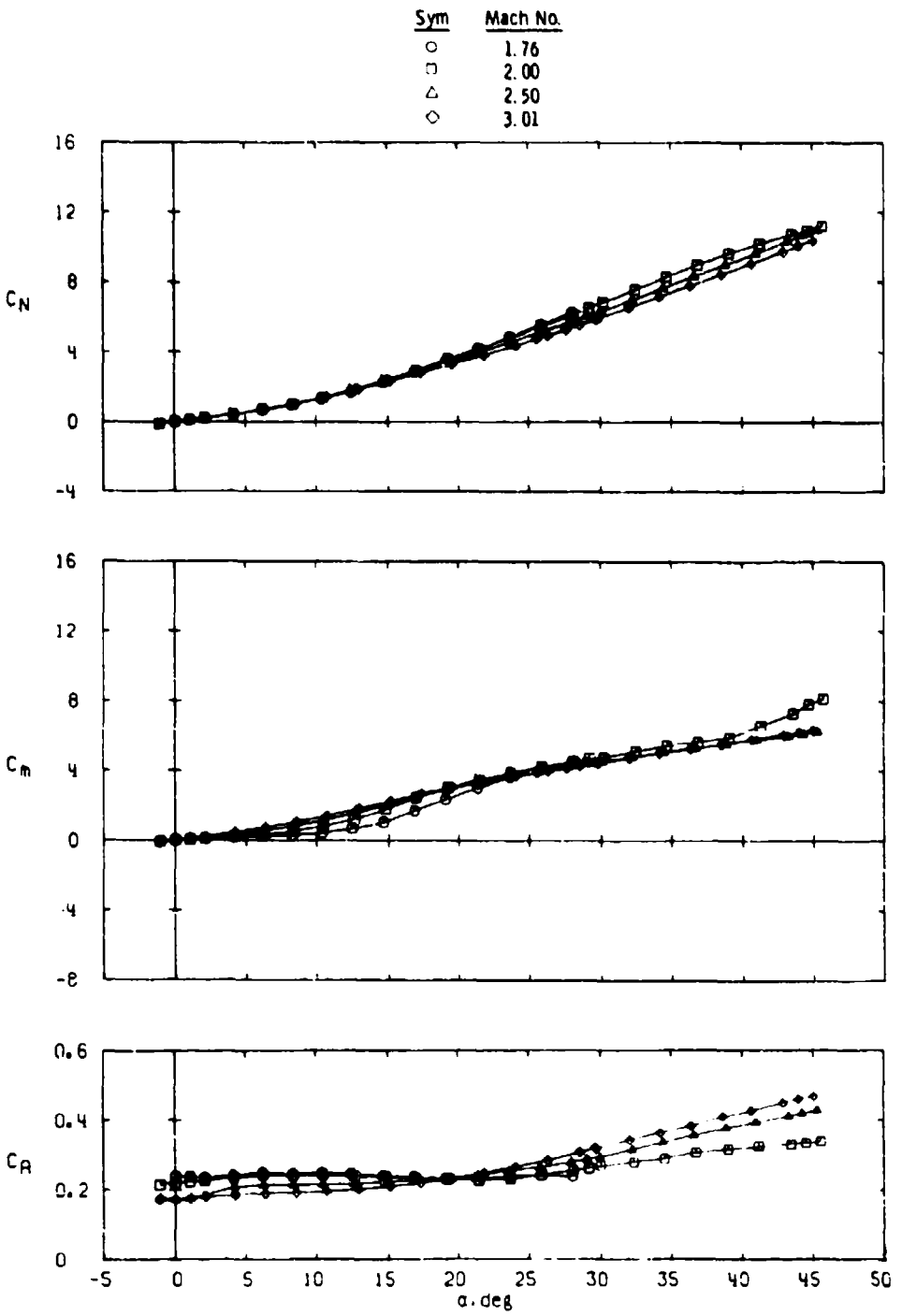

d. Configuration B*T1-4, triangular fin, AR = 1.0, S_T = 7.031 in.^{2}
Figure 14. Concluded.

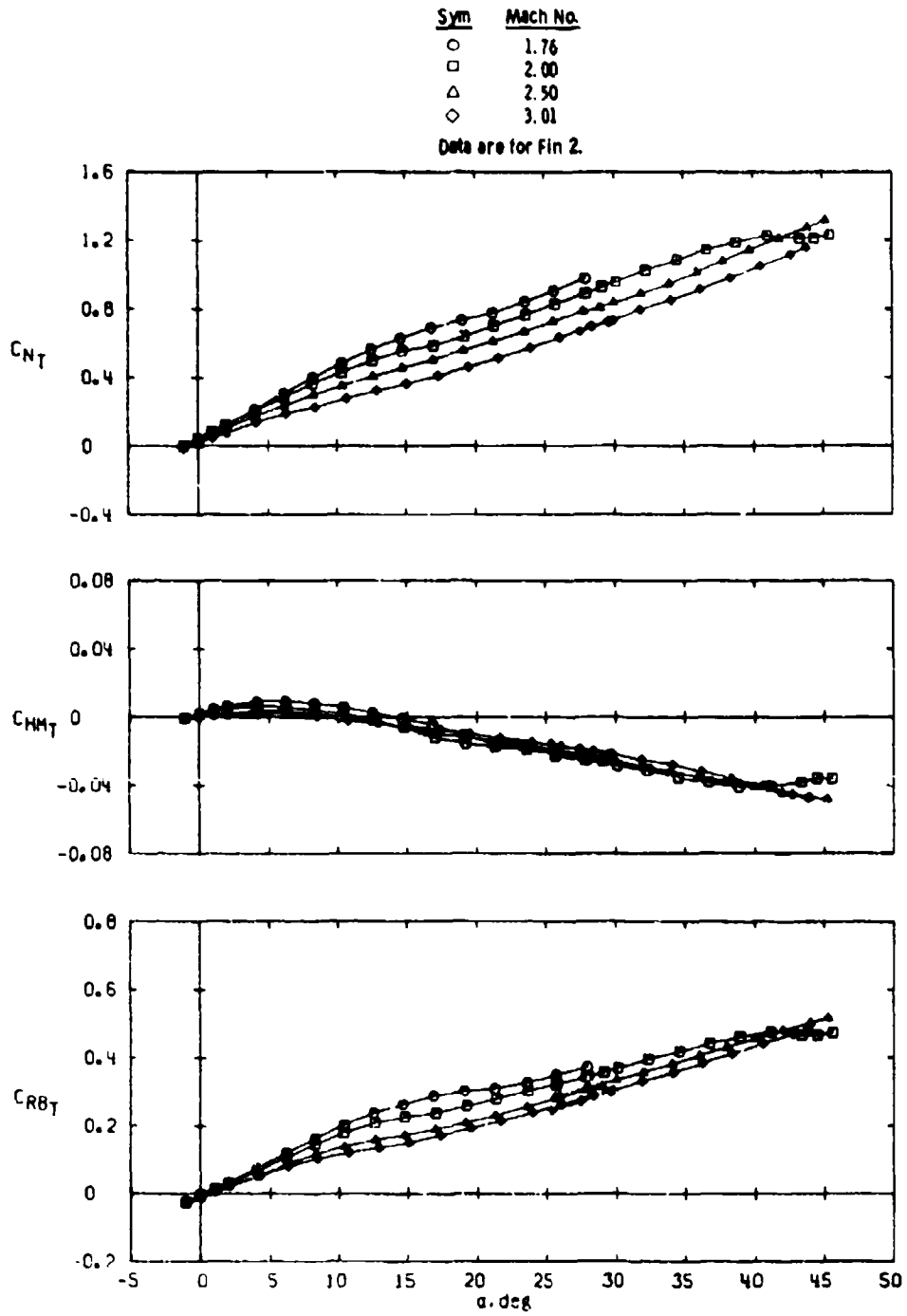

a. Configuration B*T1-5, delta fin, S_T = 7.023 in.^{2}

Figure 15. Effect of Mach number on fin aerodynamic characteristics for aspect ratio 1.0 fins, ϕ = 0.

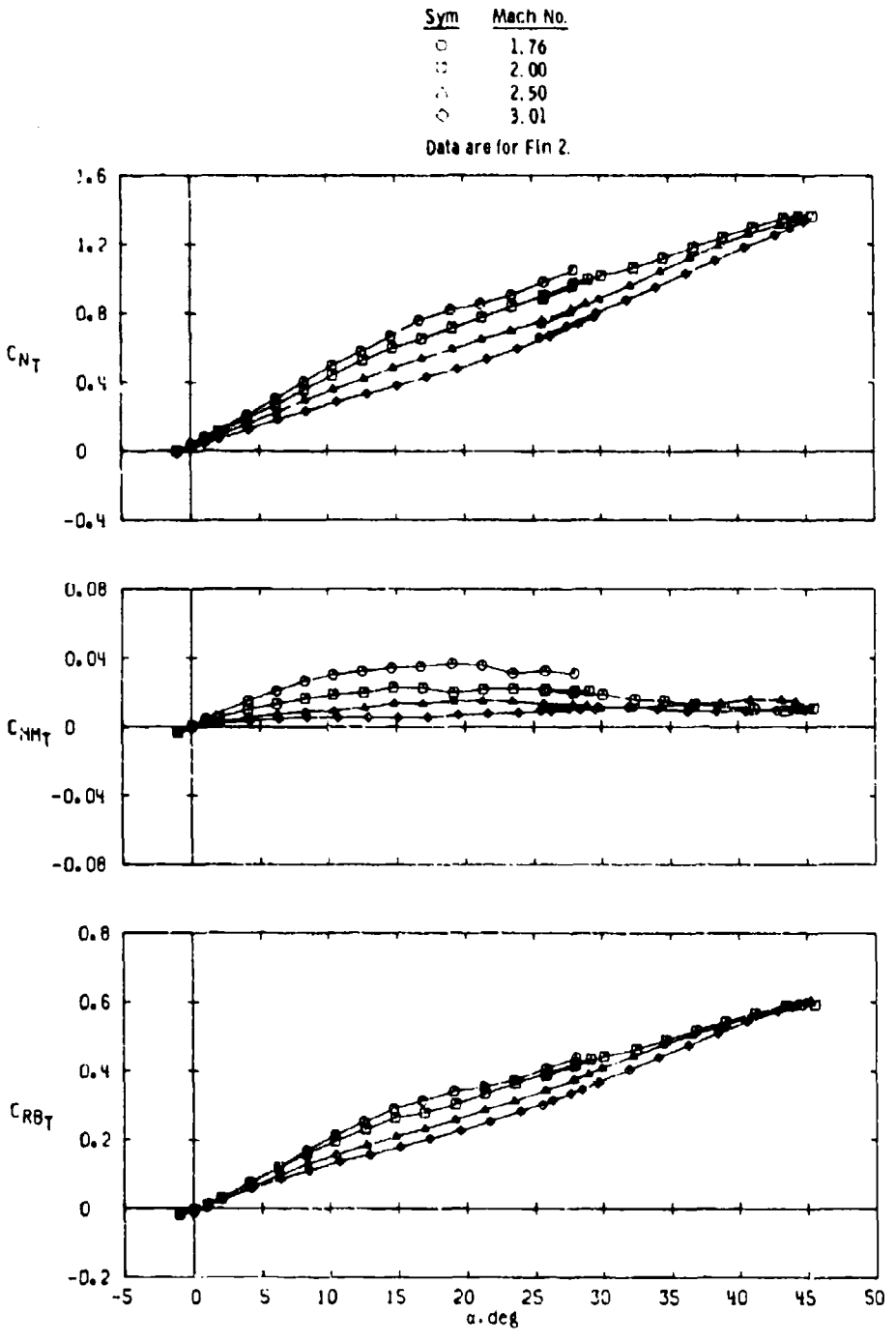

b. Configuration B*T1-1, rectangular fin, S_T = 7.031 in.^{2}
Figure 15. Continued.

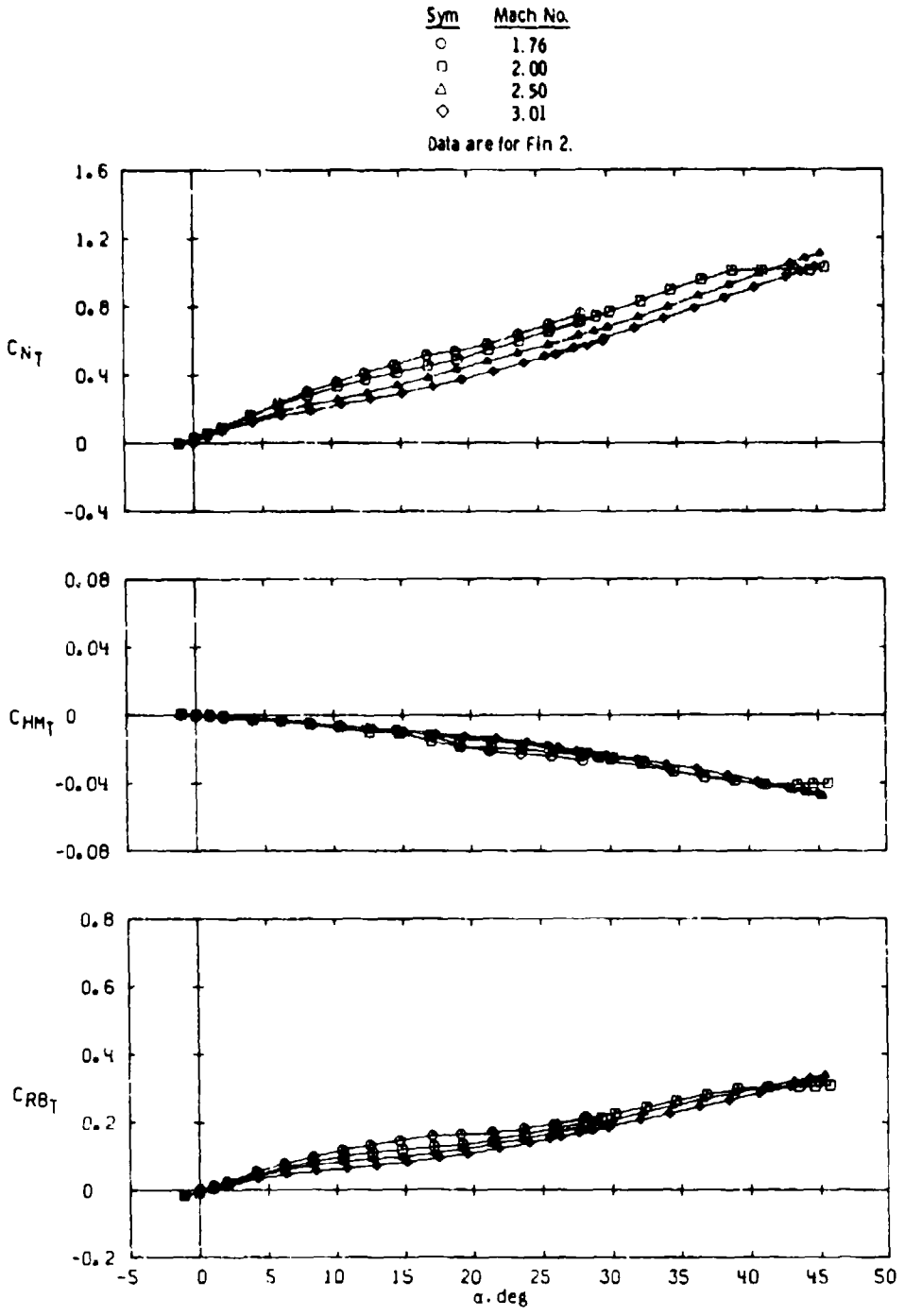

c. Configuration B*T1-4, triangular fin, S_T = 7.031 in.^{2}

Figure 15. Concluded.

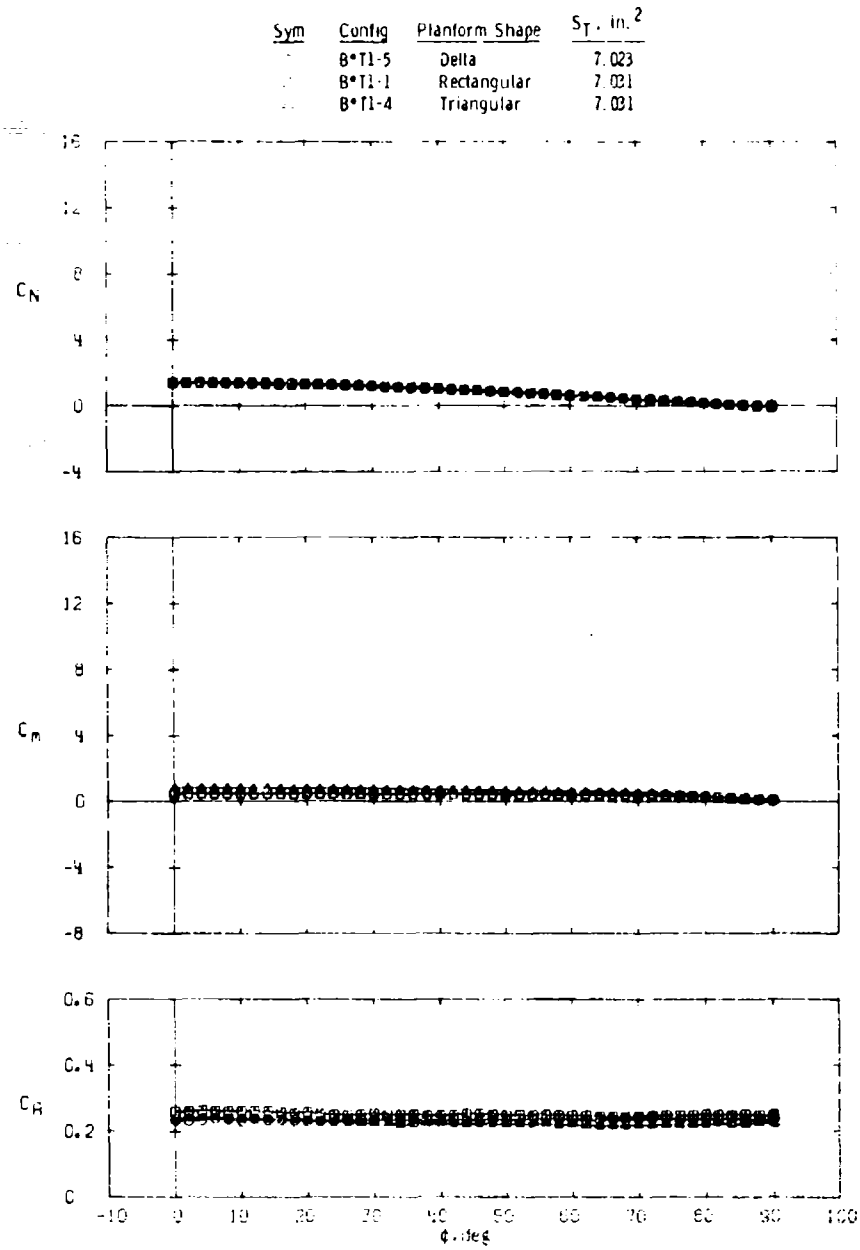

ε. $\alpha \approx 10$ deg

Figure 16. Variations in missile normal-force, pitching-moment, and axial-force coefficients with roll angle for different fin planform shapes of aspect ratio 1.0, $M_\infty = 2.00$.

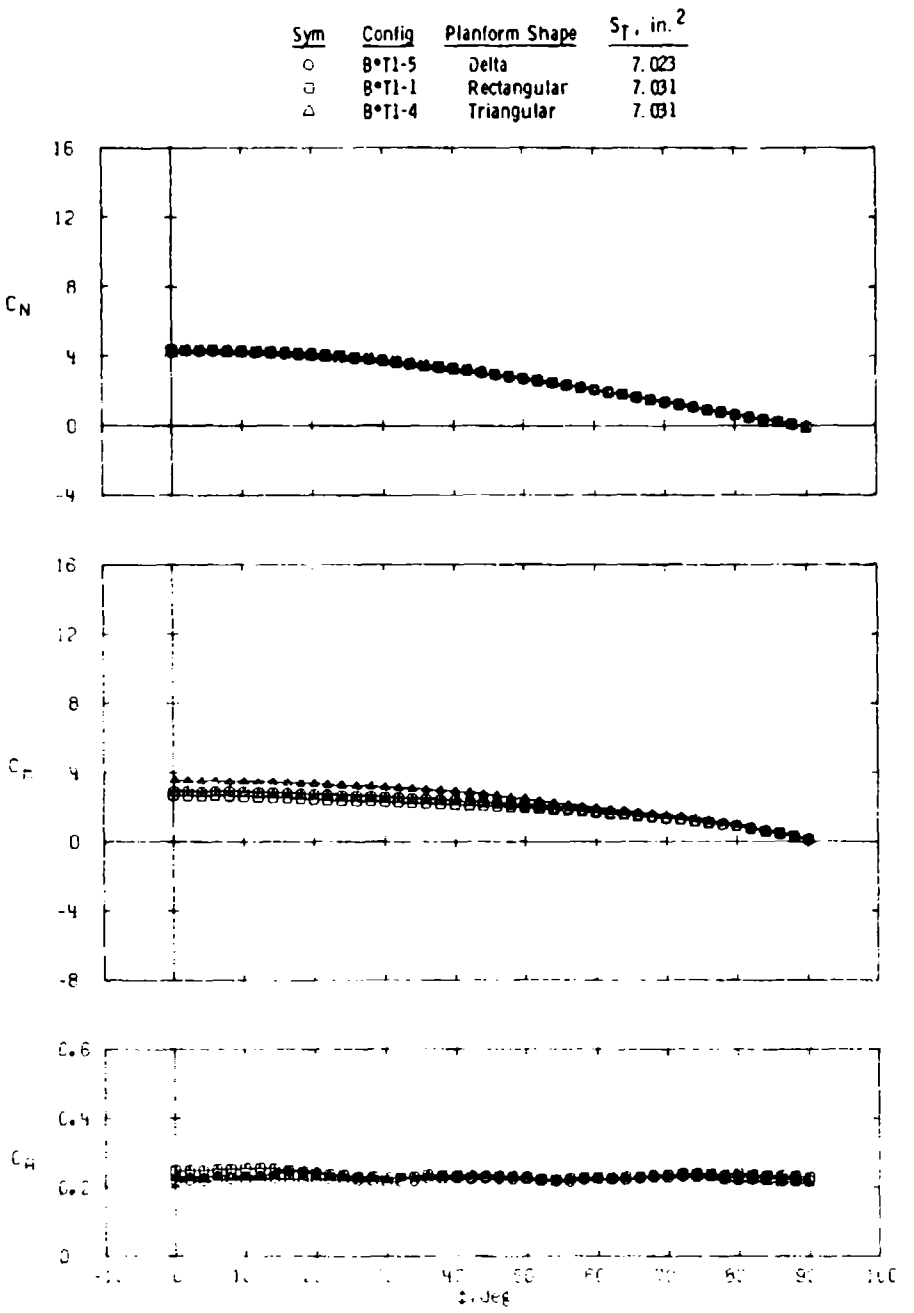

b. $\alpha \approx 21$ deg
Figure 16. Continued.

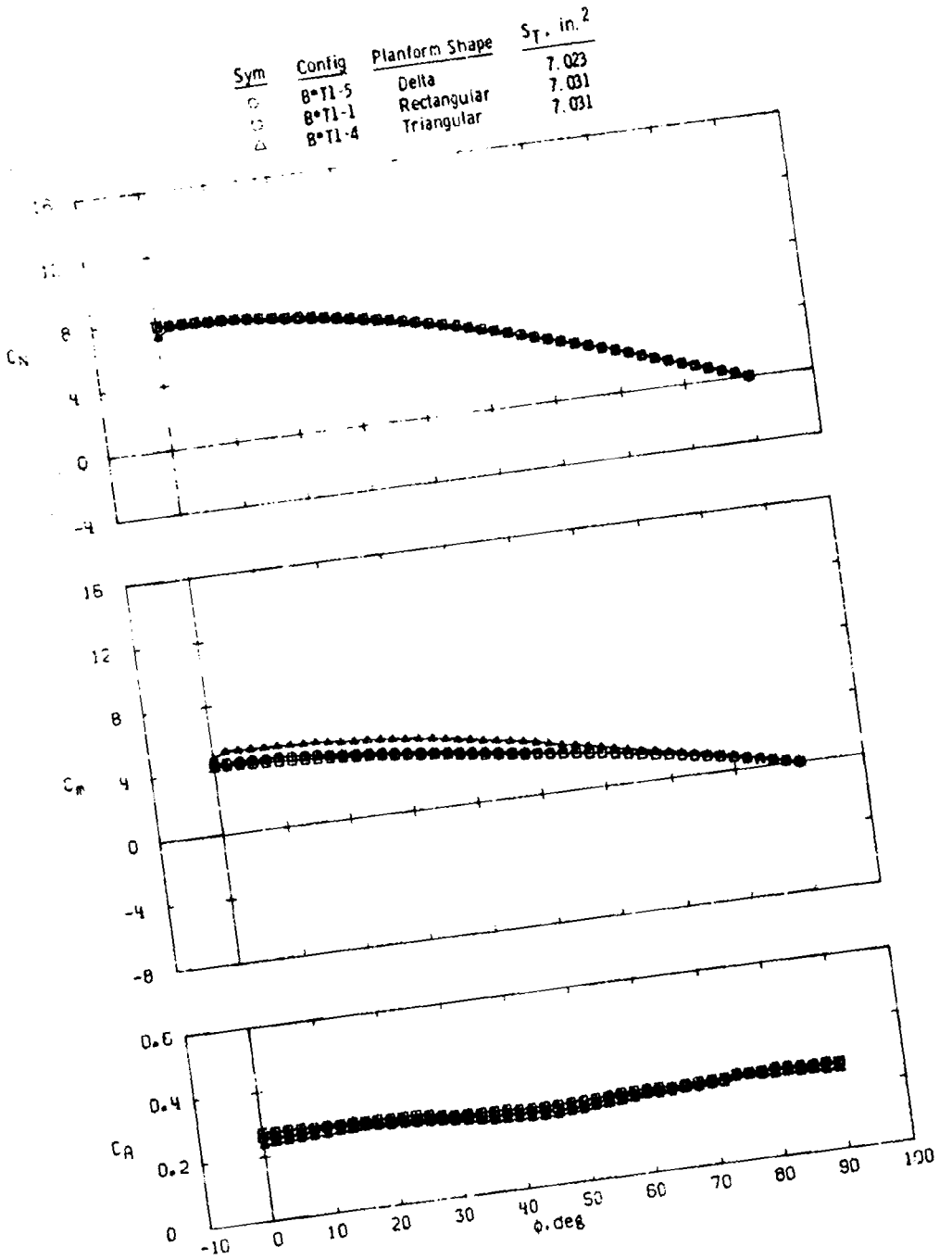

c. $\alpha \approx 32$ deg

Figure 16. Continued.

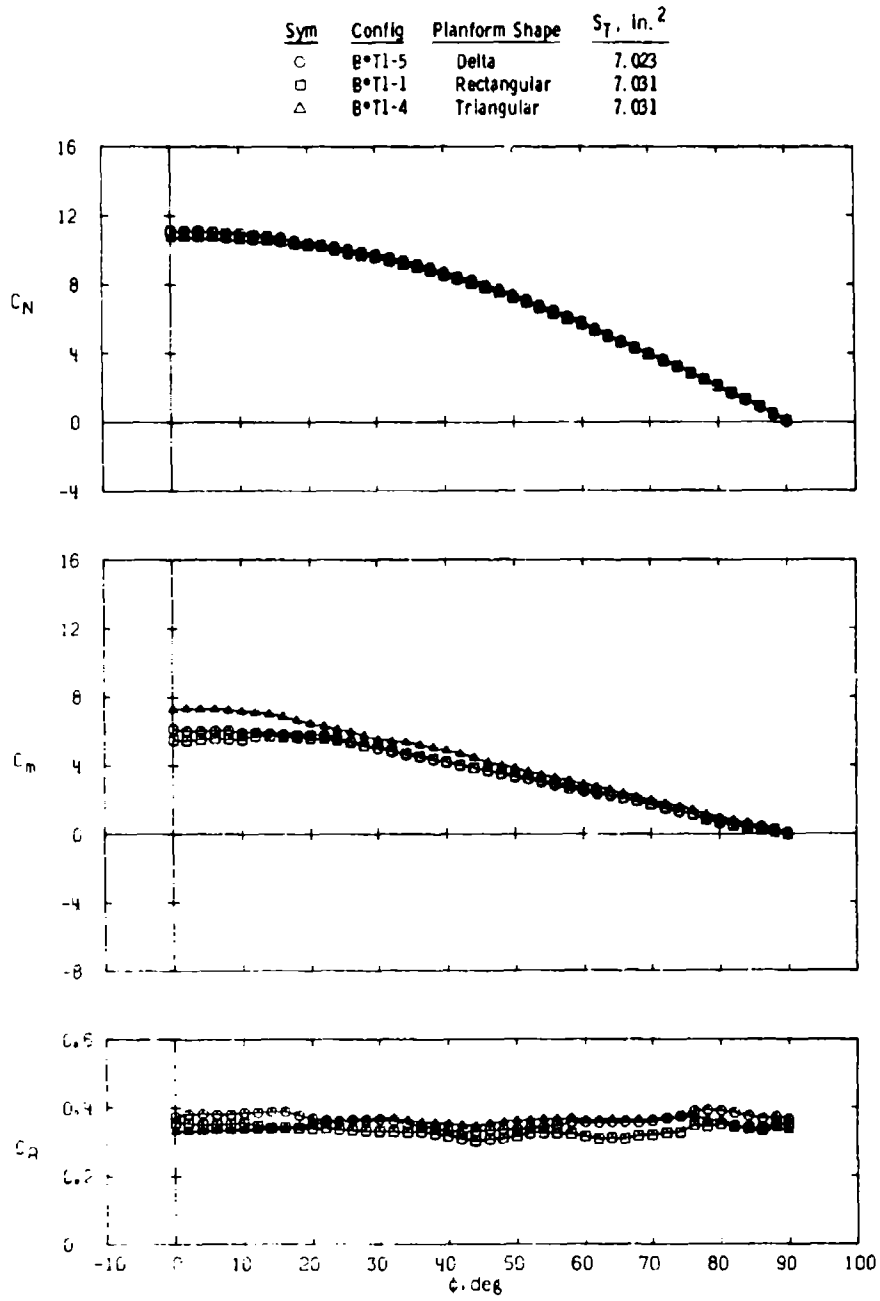

d. $\alpha \approx$ 43 deg

Figure 16. Concluded.

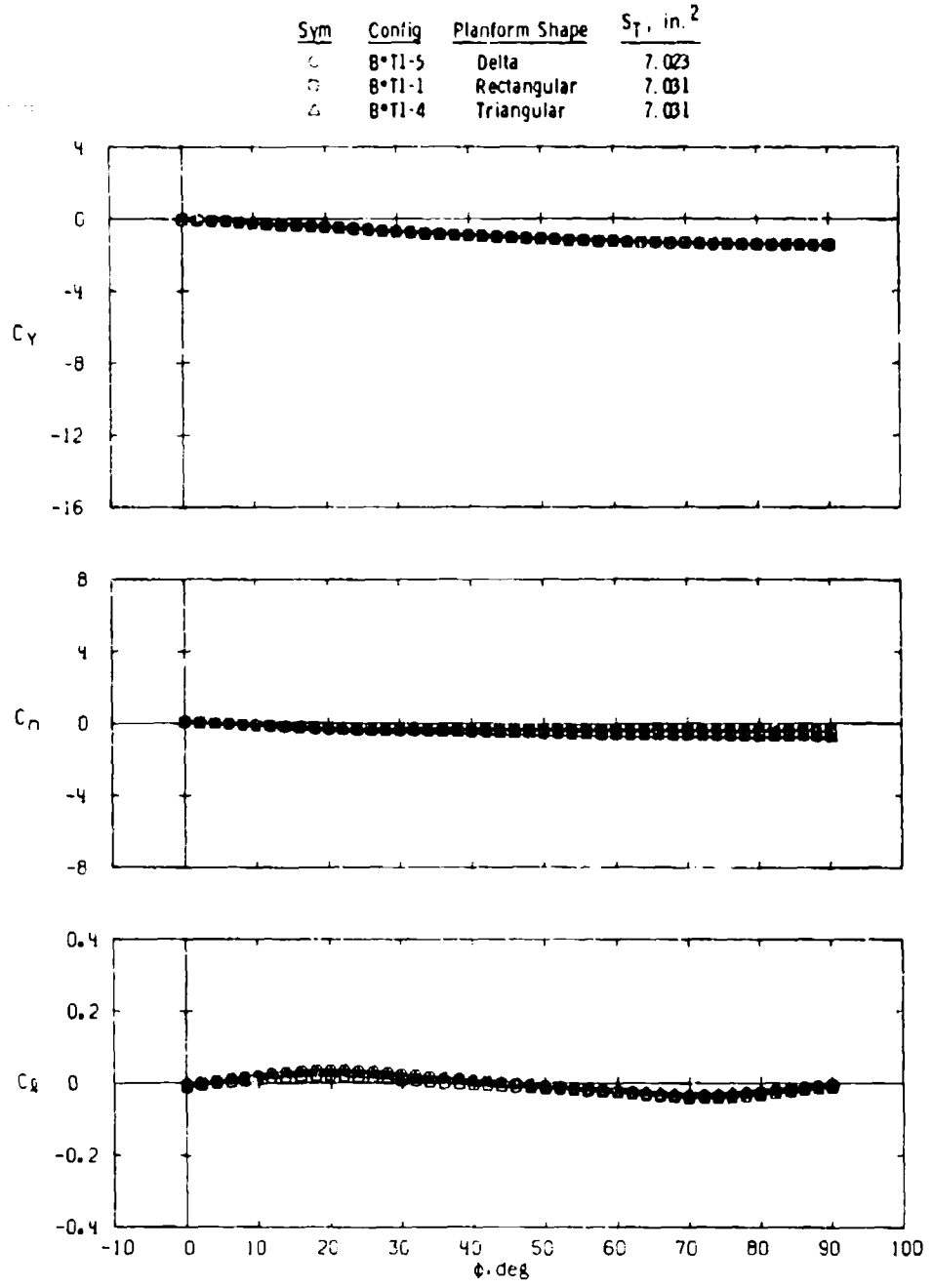

a. $\alpha \approx 10$ deg

Figure 17. Variations in missile side-force, yawing-moment, and rolling-moment coefficients with roll angle for different fin planform shapes of aspect ratio 1.0, M_∞ = 2.00.

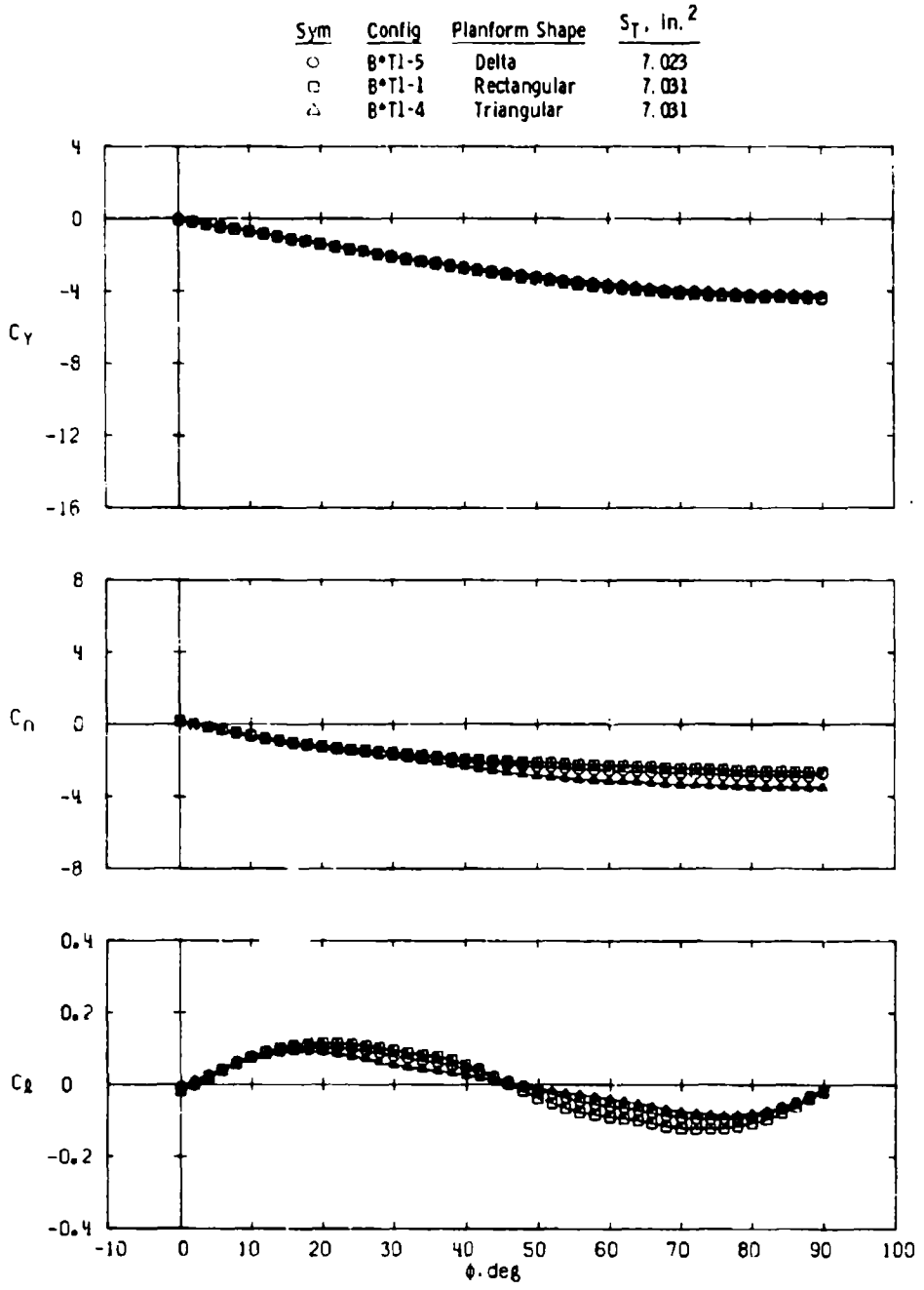

b. $\alpha \approx 21$ deg

Figure 17. Continued.

Sym	Config	Planform Shape	S_T, in.^{2}
○	B*T1-5	Delta	7.023
□	B*T1-1	Rectangular	7.031
△	B*T1-4	Triangular	7.031

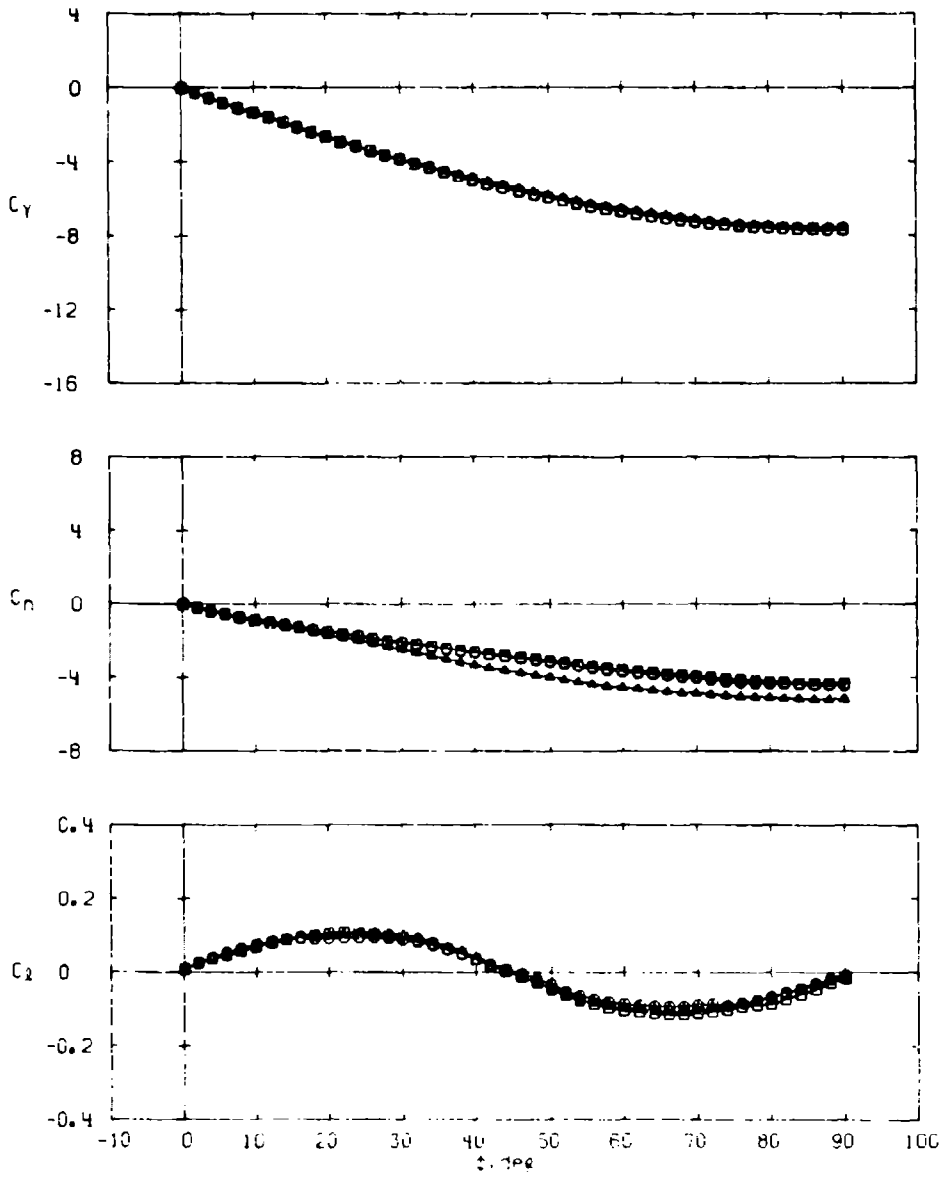

c. $\alpha \approx 32$ deg

Figure 17. Continued.

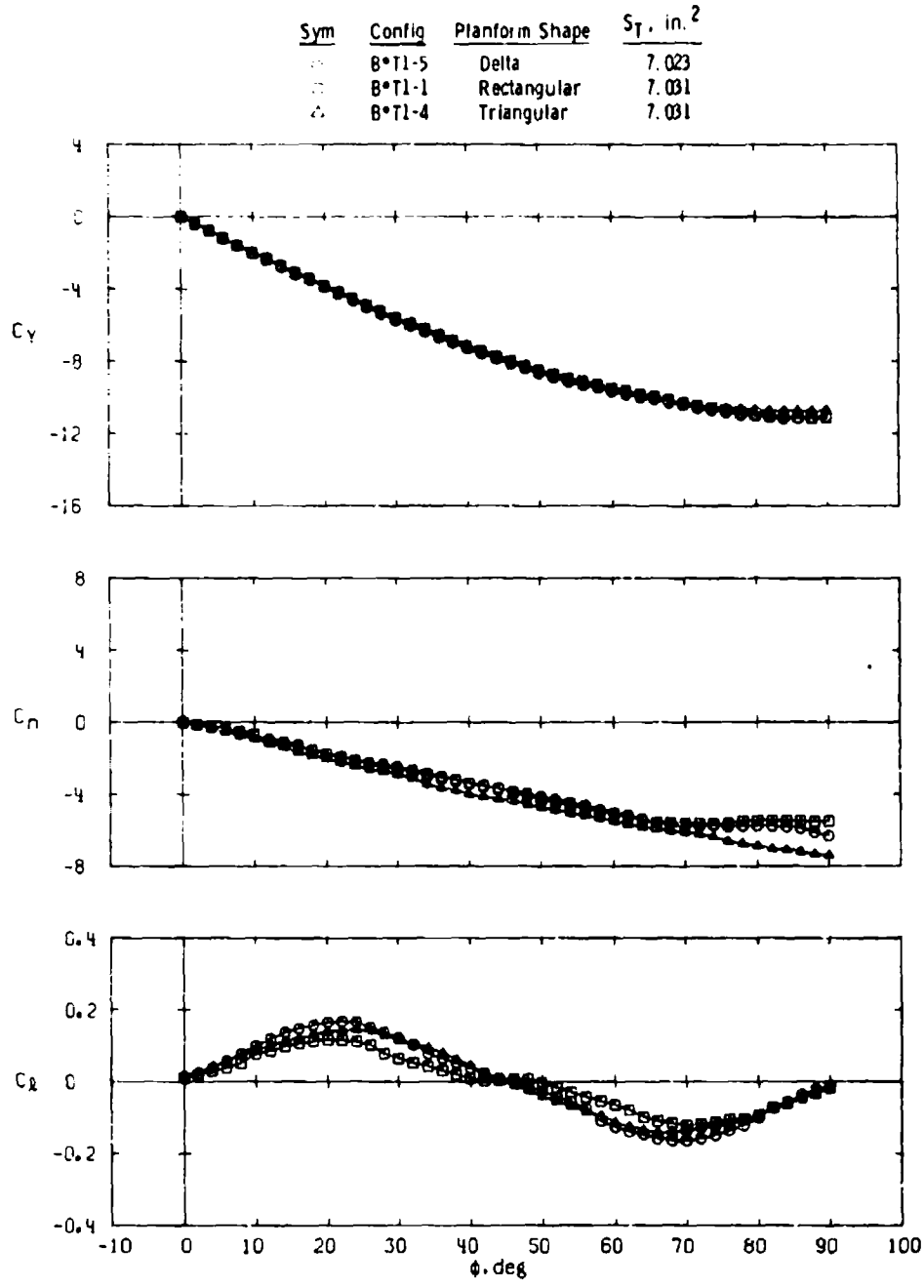

d. $\alpha \approx 43$ deg

Figure 17. Concluded.

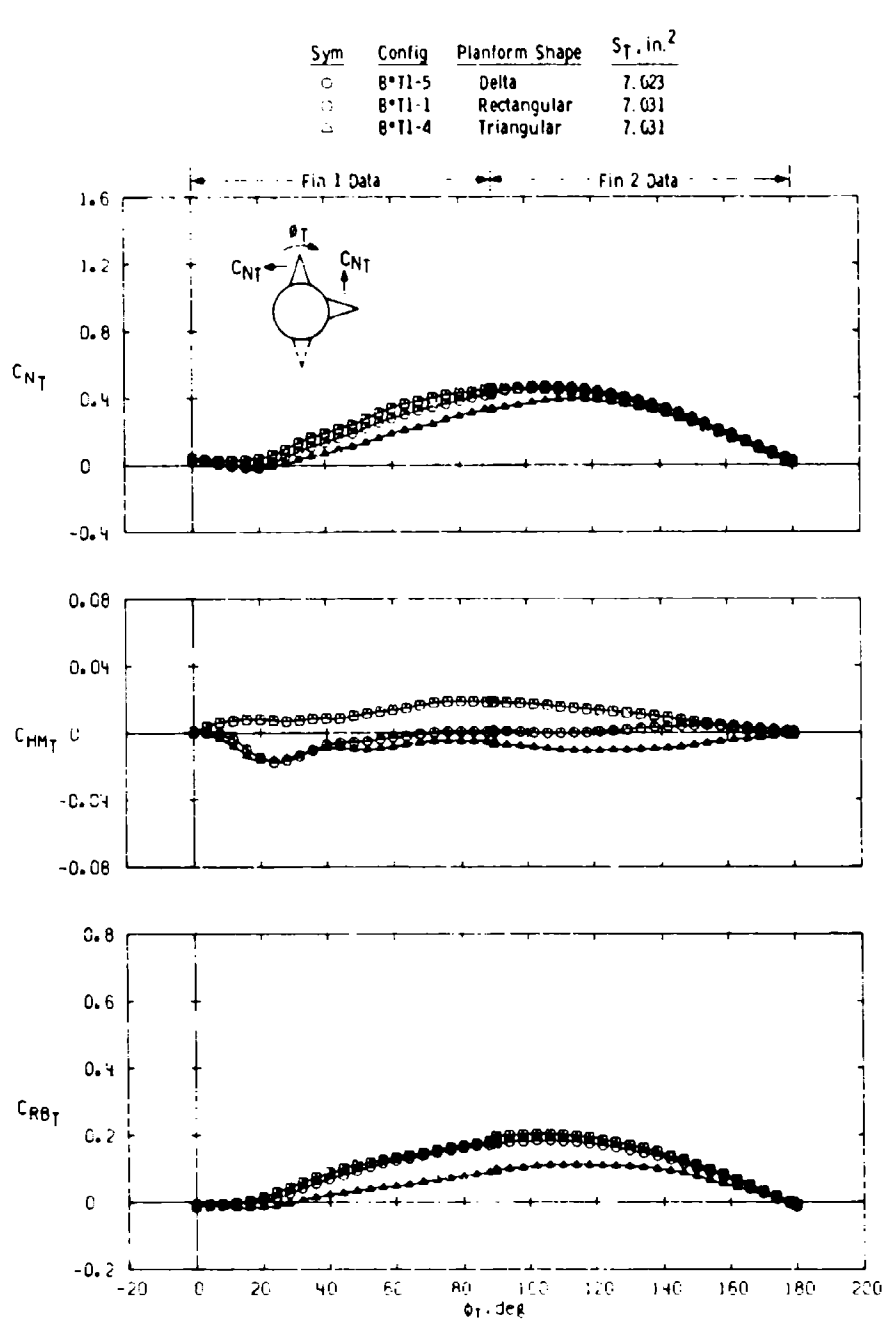

a. $\alpha \approx 10$ deg

Figure 18. Variations in fin normal-force, hinge-moment, and bending-moment coefficients with fin roll position for different fin planform shapes of aspect ratio 1.0, M_∞ = 2.00.

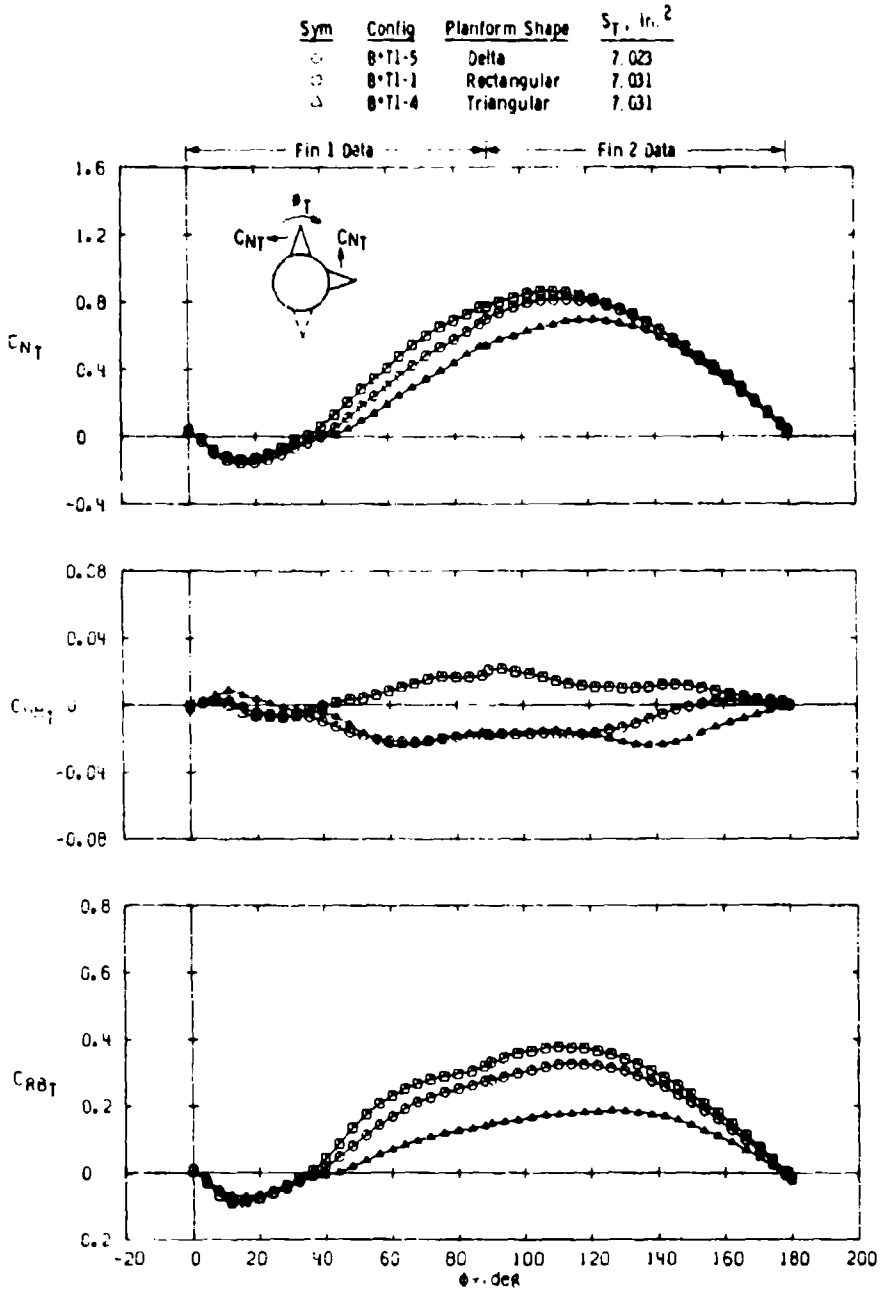

b. $\alpha \approx 21$ deg

Figure 18. Continued.

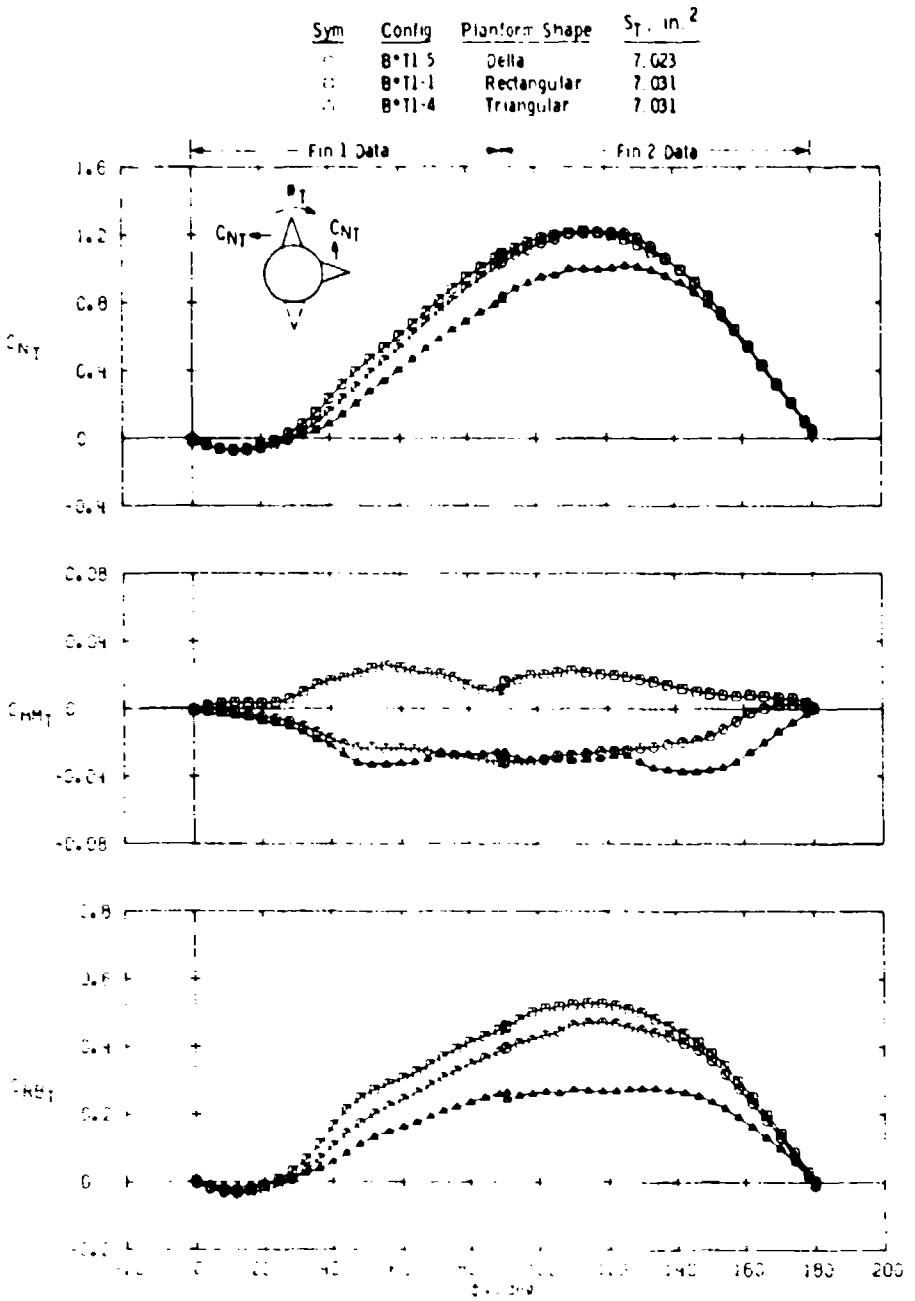

c. α = 32 deg

Figure 18. Continued.

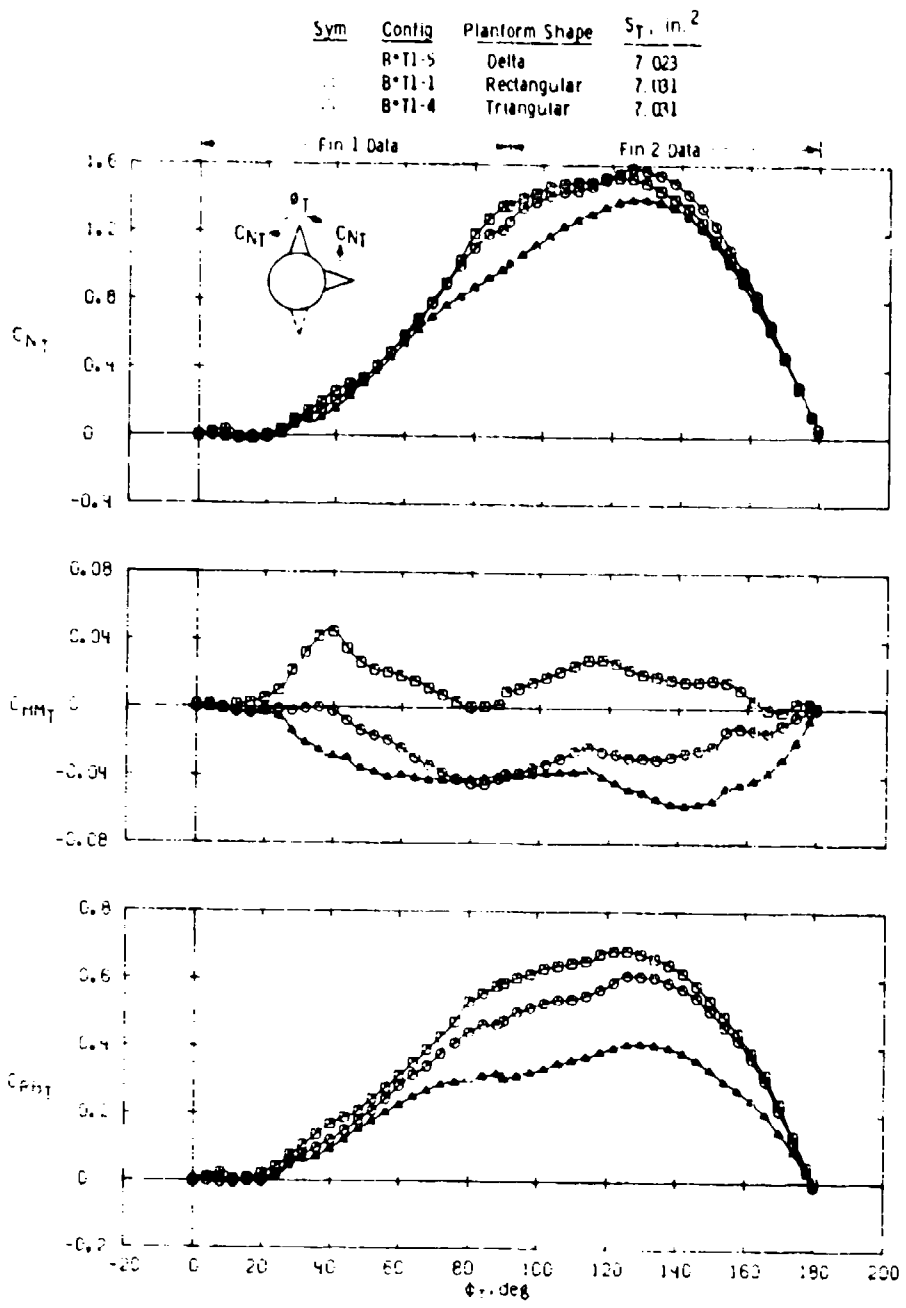

d. $\alpha \approx 43$ deg

Figure 18. Concluded.

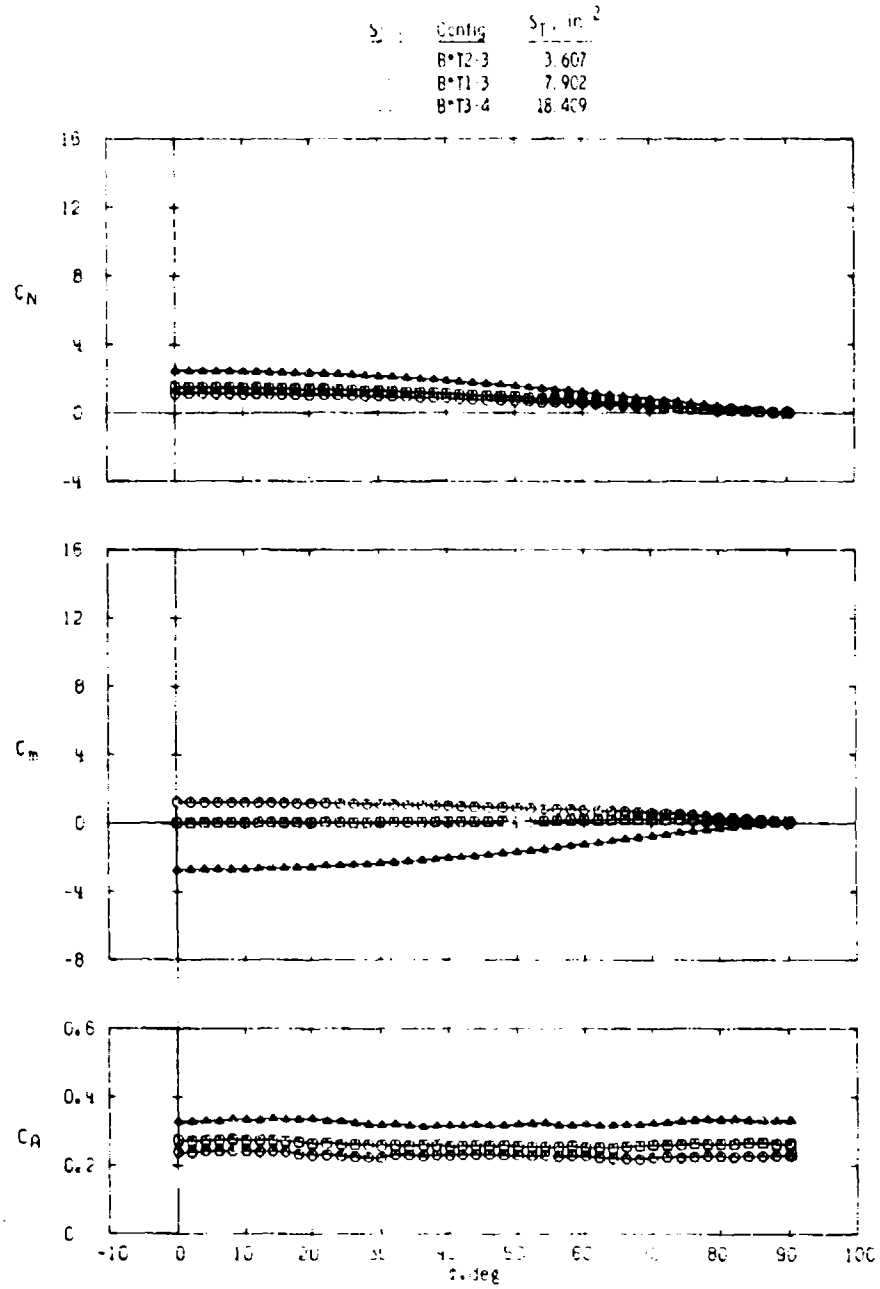

a. α = 10 deg

Figure 19. Variations in missile normal-force, pitching-moment, and axial-force coefficients with roll angle for different delta fin planform areas of aspect ratio 2.0, M_∞ = 2.00.

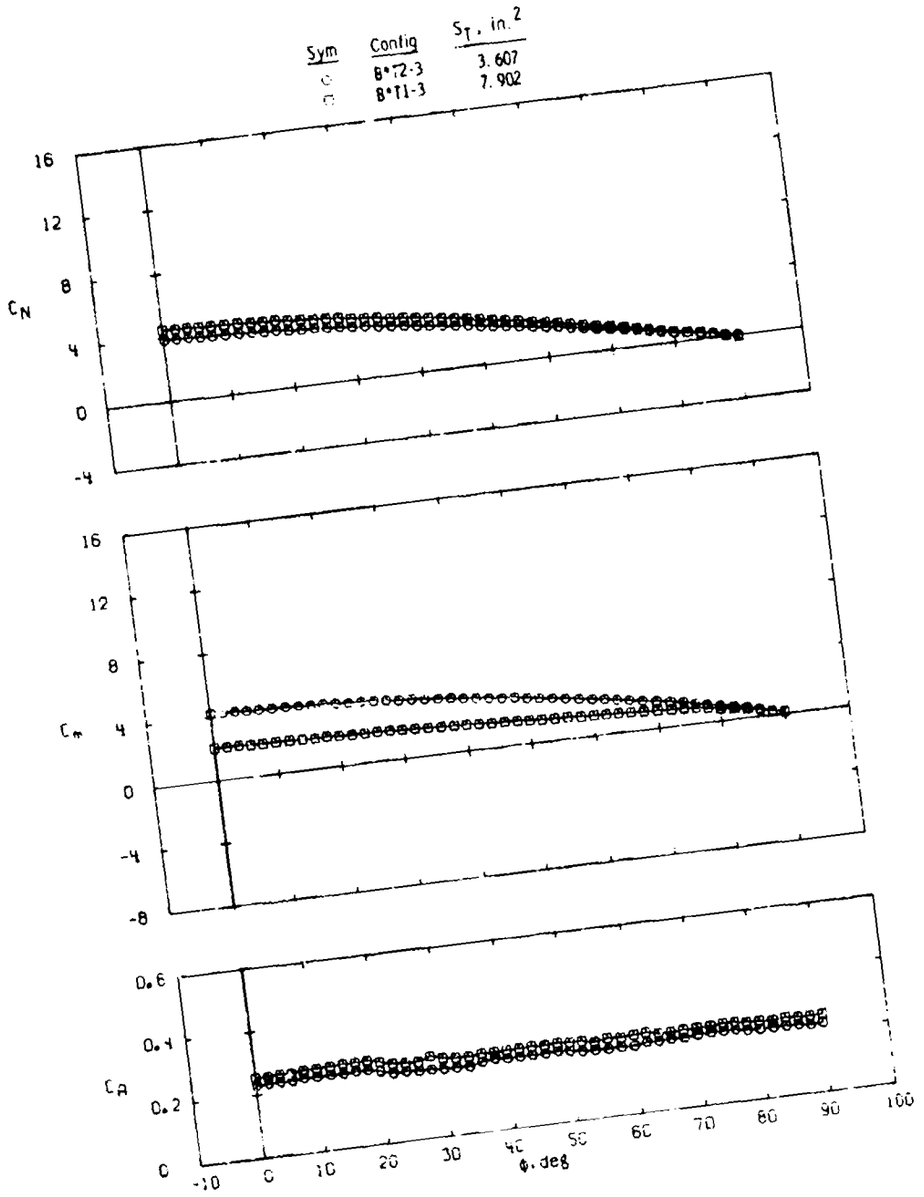

b. $\alpha \approx 21$ deg

Figure 19. Continued.

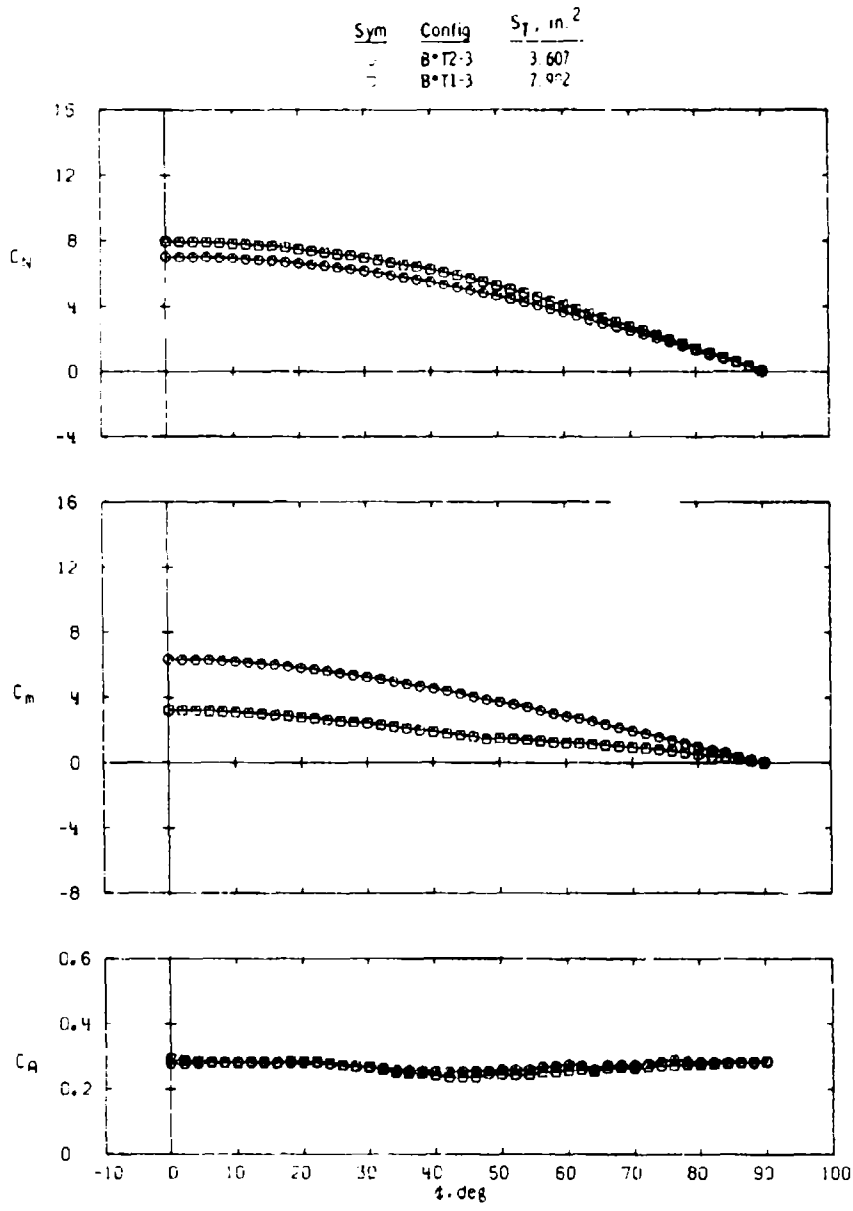

c. $\alpha \approx 32$ deg

Figure 19. Concluded.

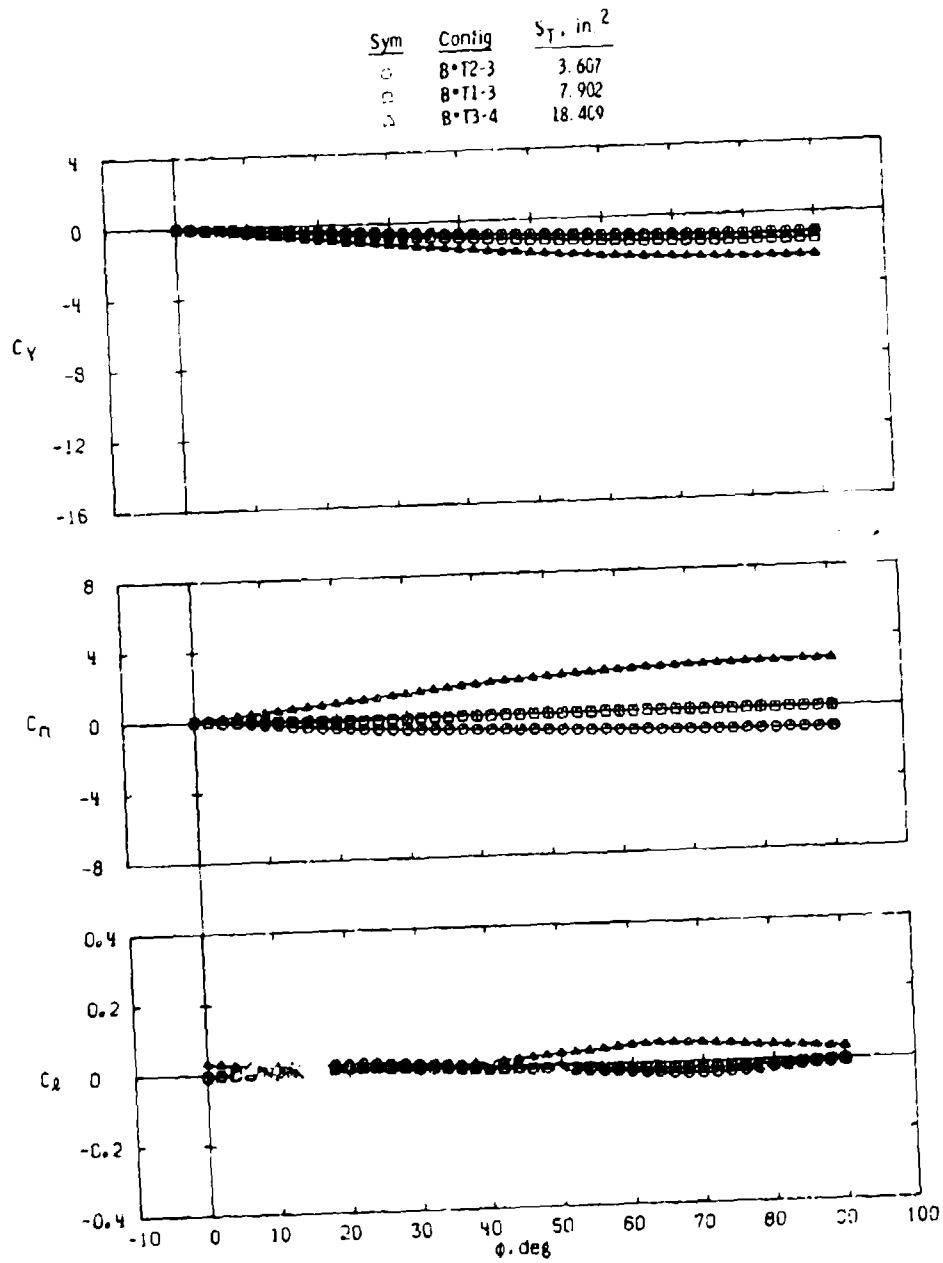

a. $\alpha \approx 10$ deg

Figure 20. Variations in missile side-force, yawing-moment, and rolling-moment coefficients with roll angle for different delta fin planform areas of aspect ratio 2.0, $M_\infty = 2.00$.

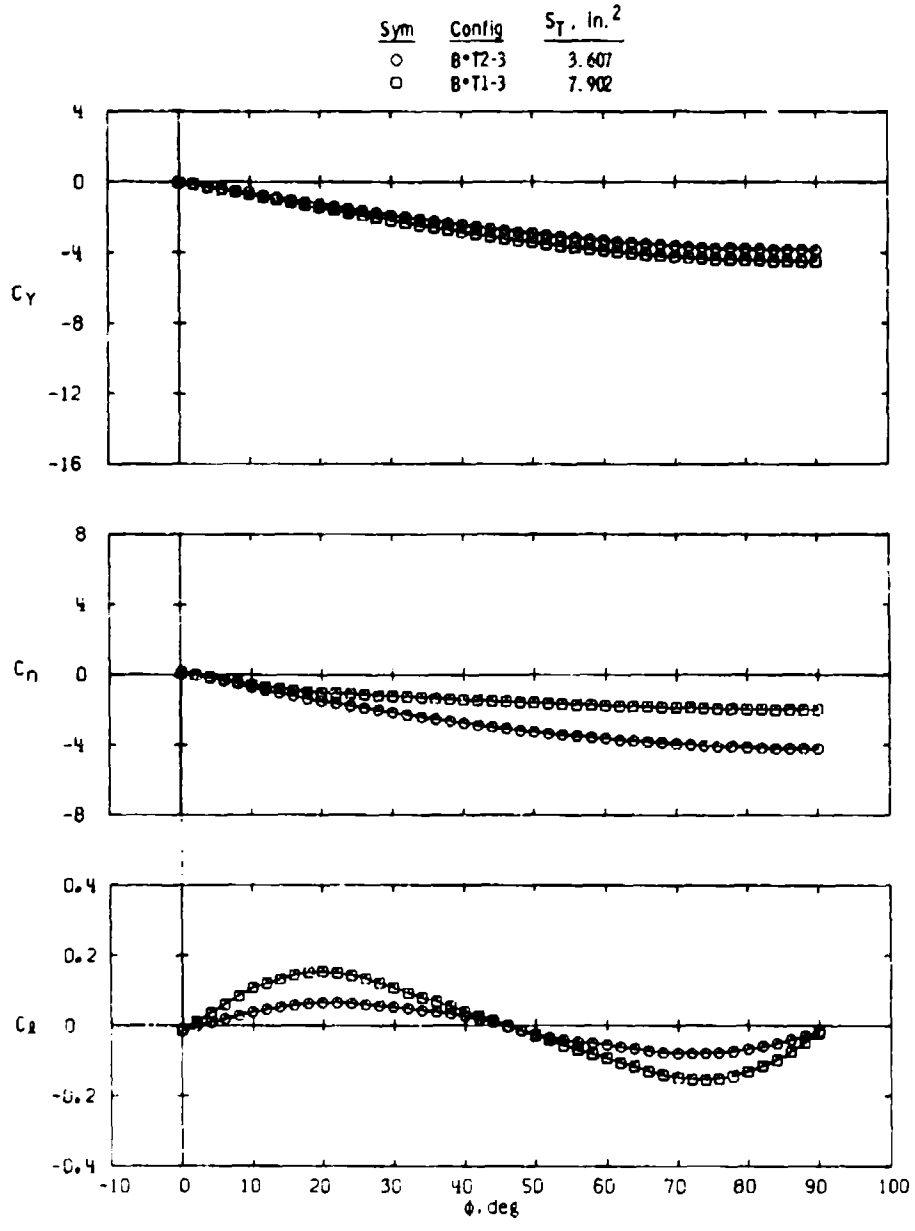

b. $\alpha \approx 21$ deg

Figure 20. Continued.

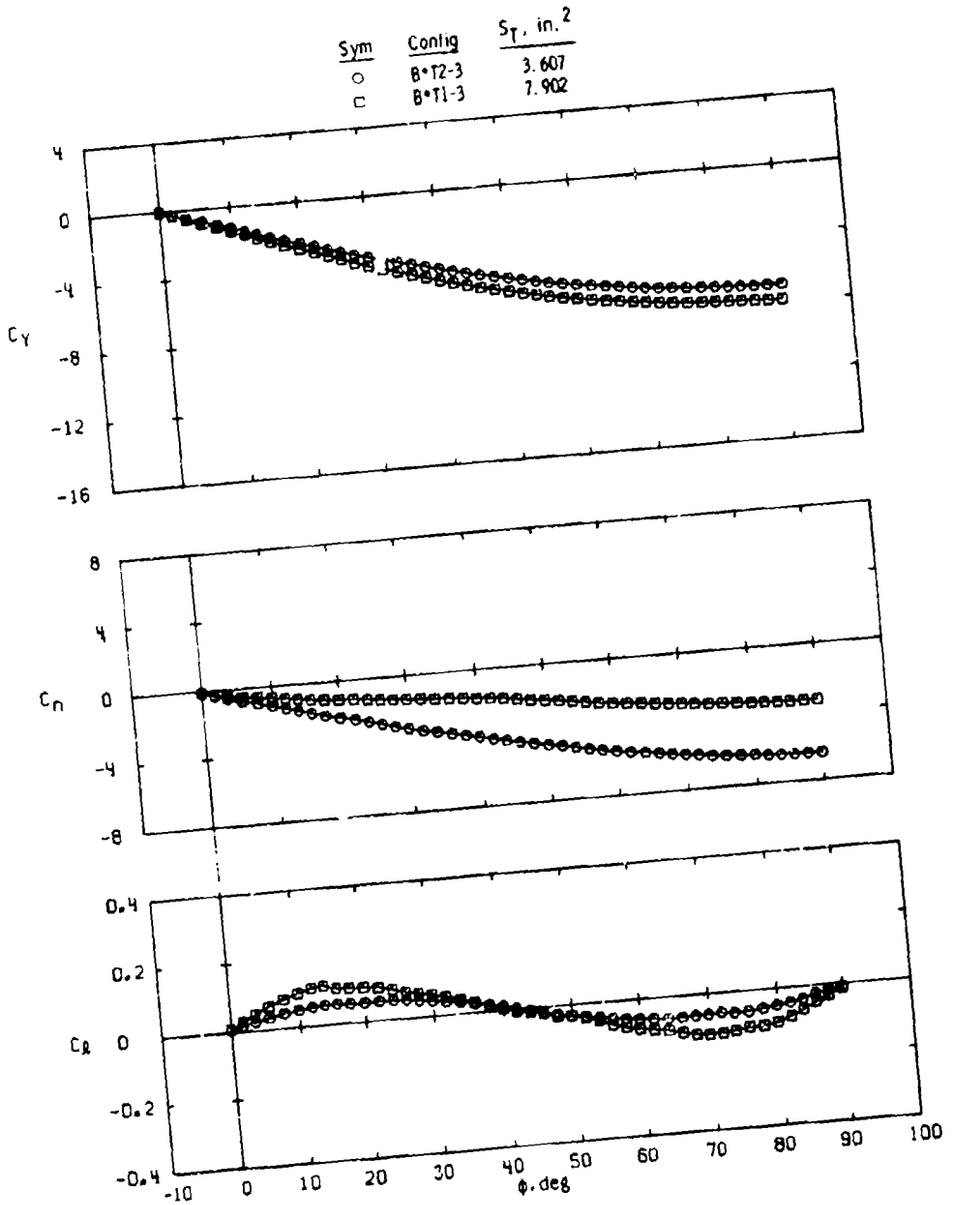

c. $\alpha \approx 32$ deg

Figure 20. Concluded.

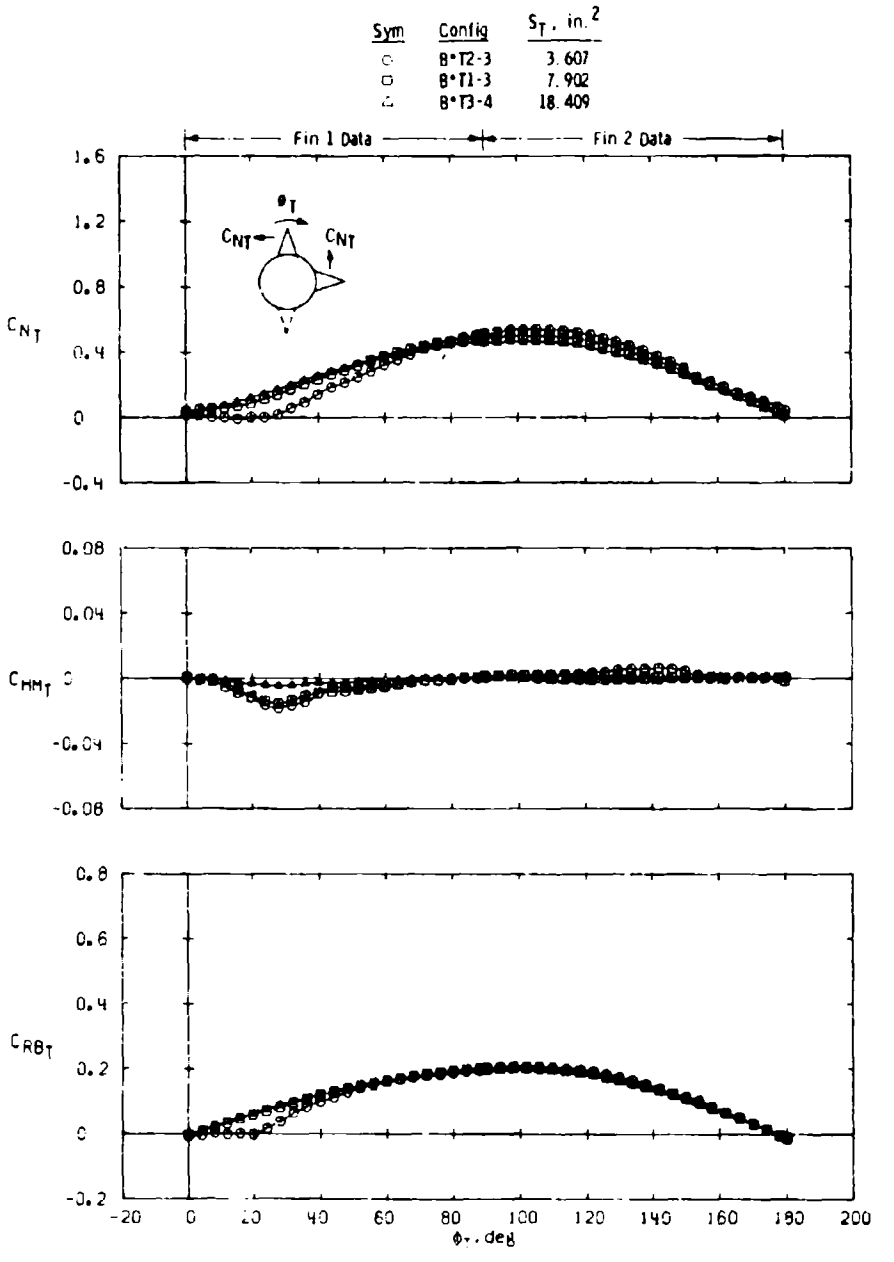

a. $\alpha \approx 10$ deg

Figure 21. Variations in fin normal-force, hinge-moment, and bending-moment coefficients with fin roll position for different delta fin planform areas of aspect ratio 2.0, $M_\infty = 2.00$.

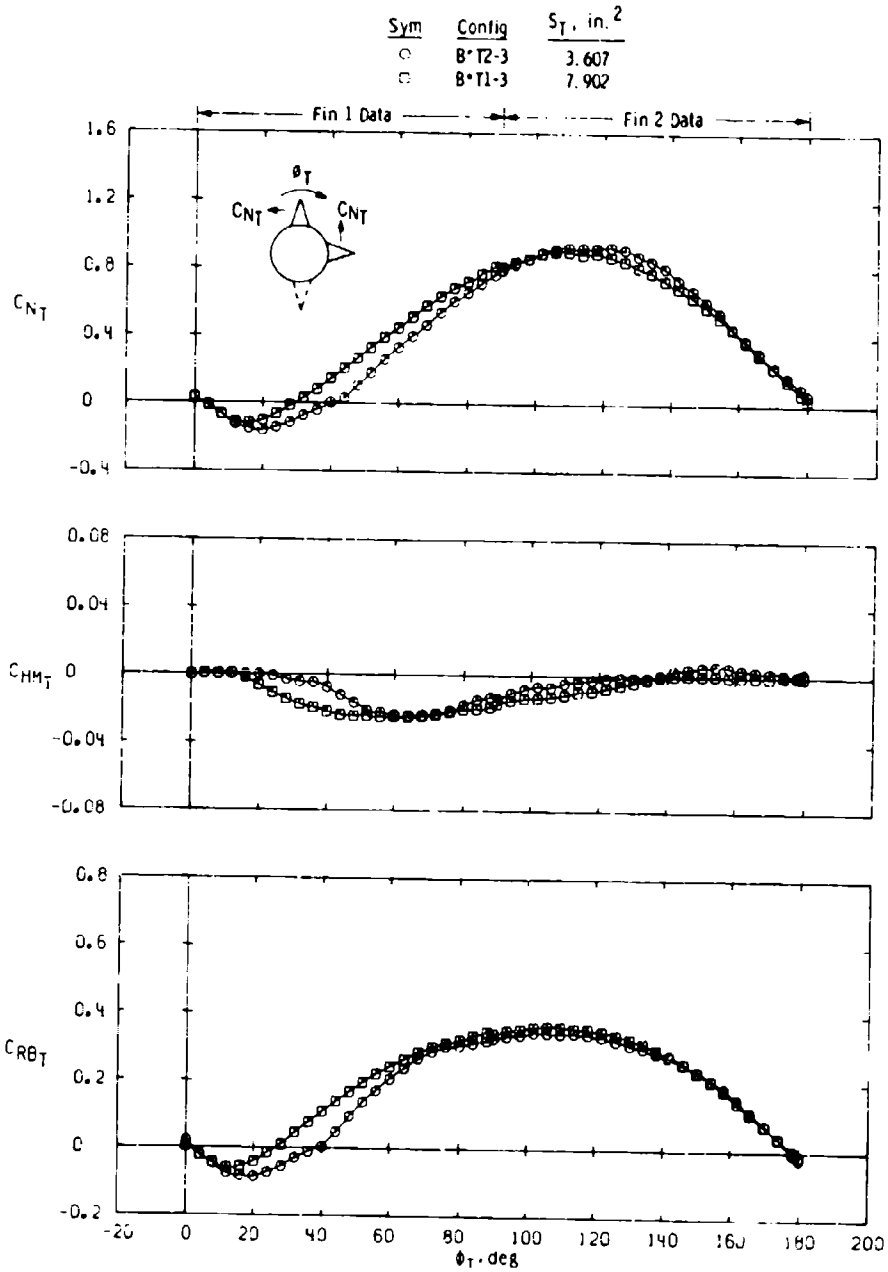

b. $\alpha \approx 21$ deg

Figure 21. Continued.

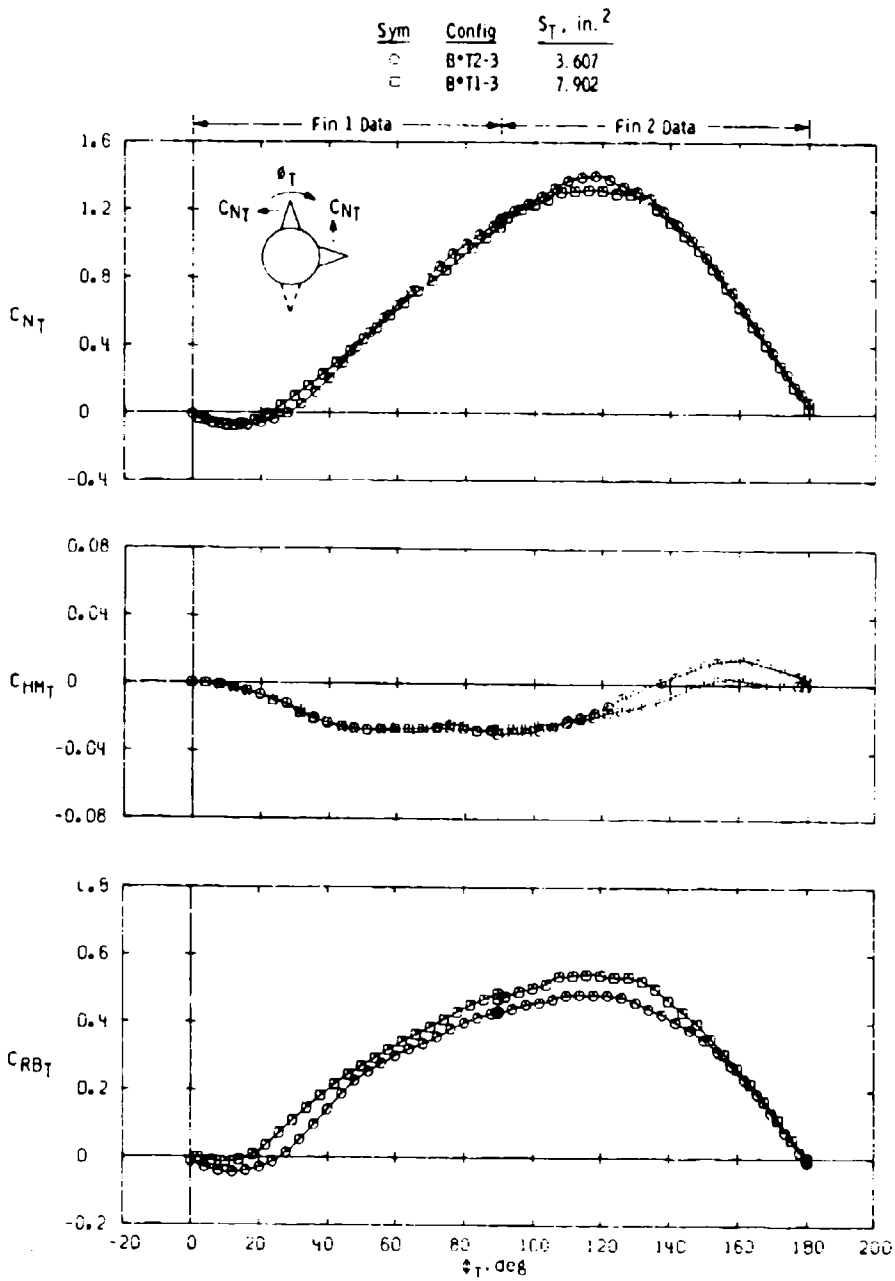

c. $\alpha \approx$ 32 deg

Figure 21. Concluded.

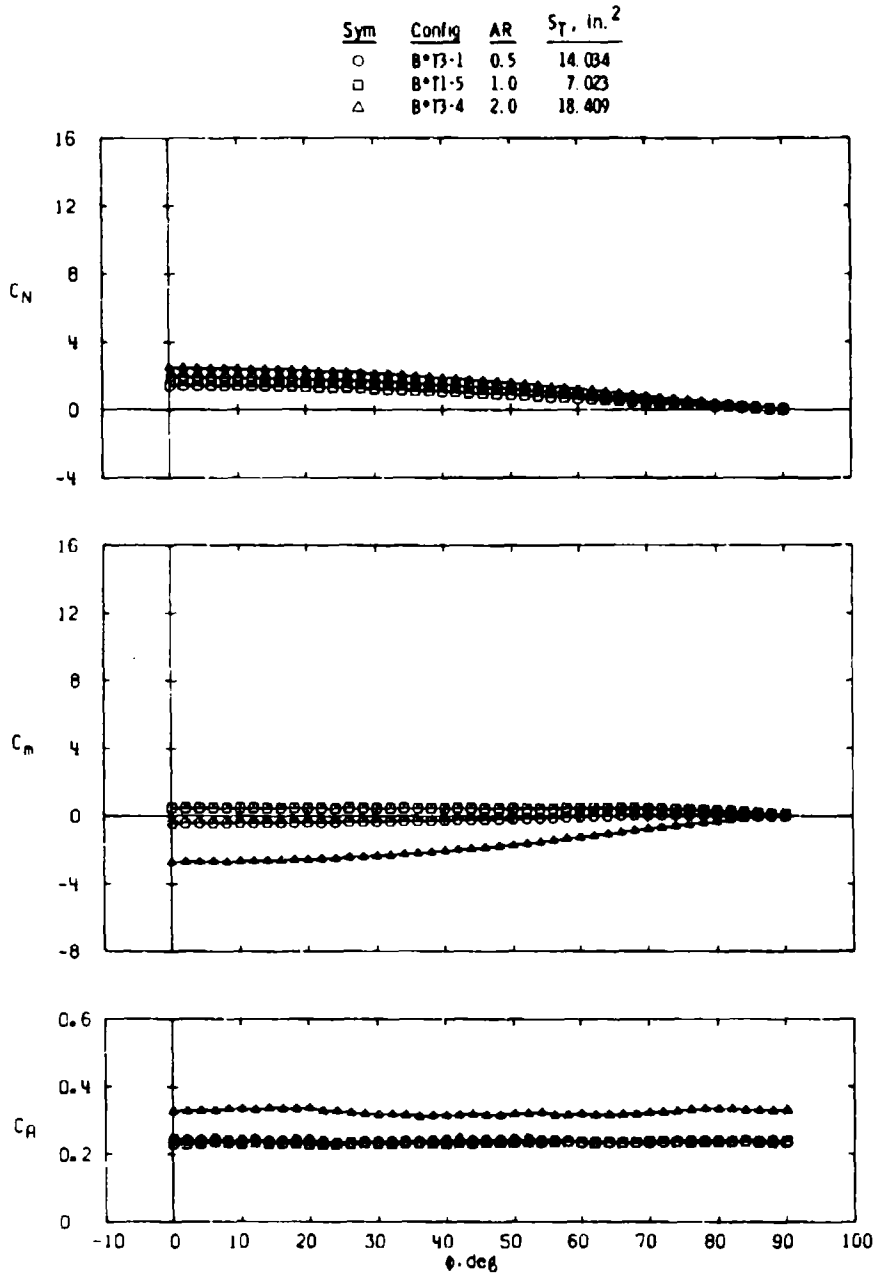

a. $\alpha \approx 10$ deg

Figure 22. Variations in missile normal-force, pitching-moment, and axial-force coefficients with roll angle for different delta fin aspect ratios, $M_\infty = 2.00$.

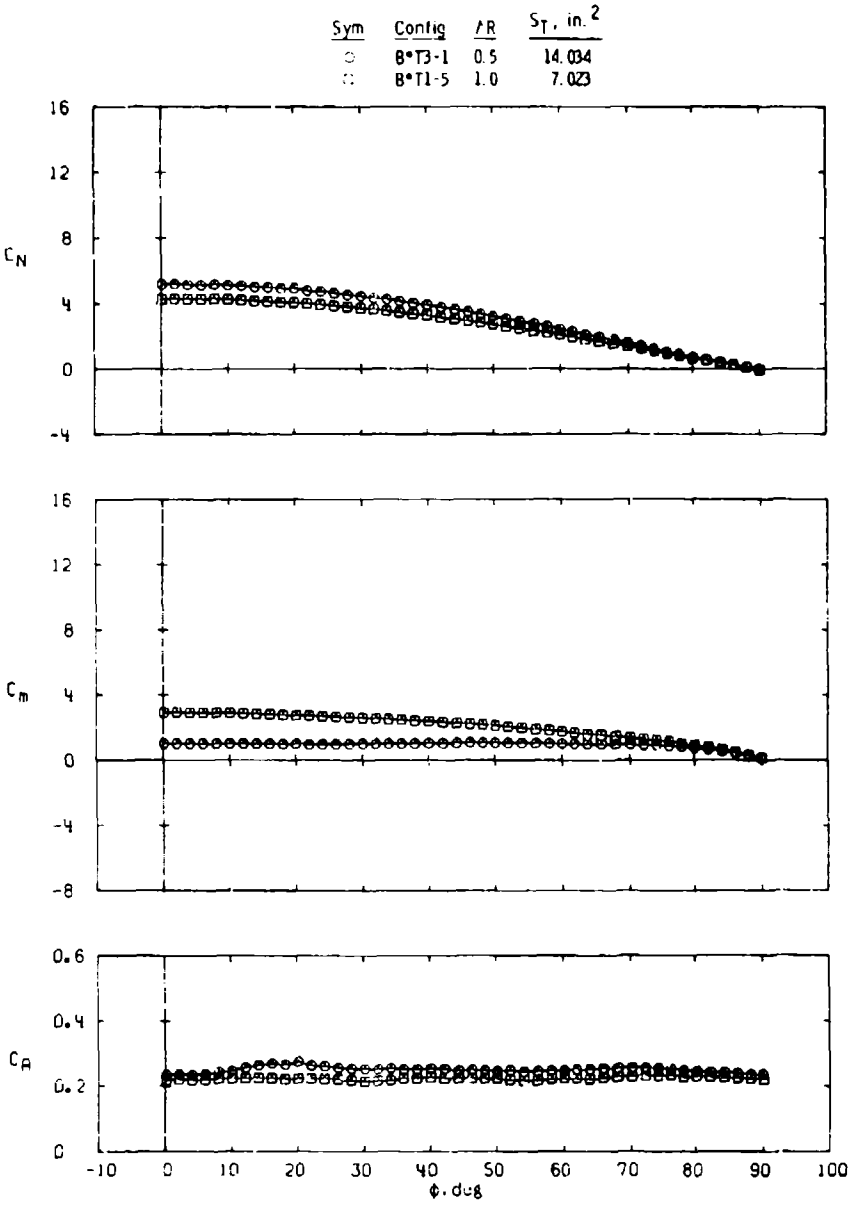

b. $\alpha \approx 21$ deg

Figure 22. Continued.

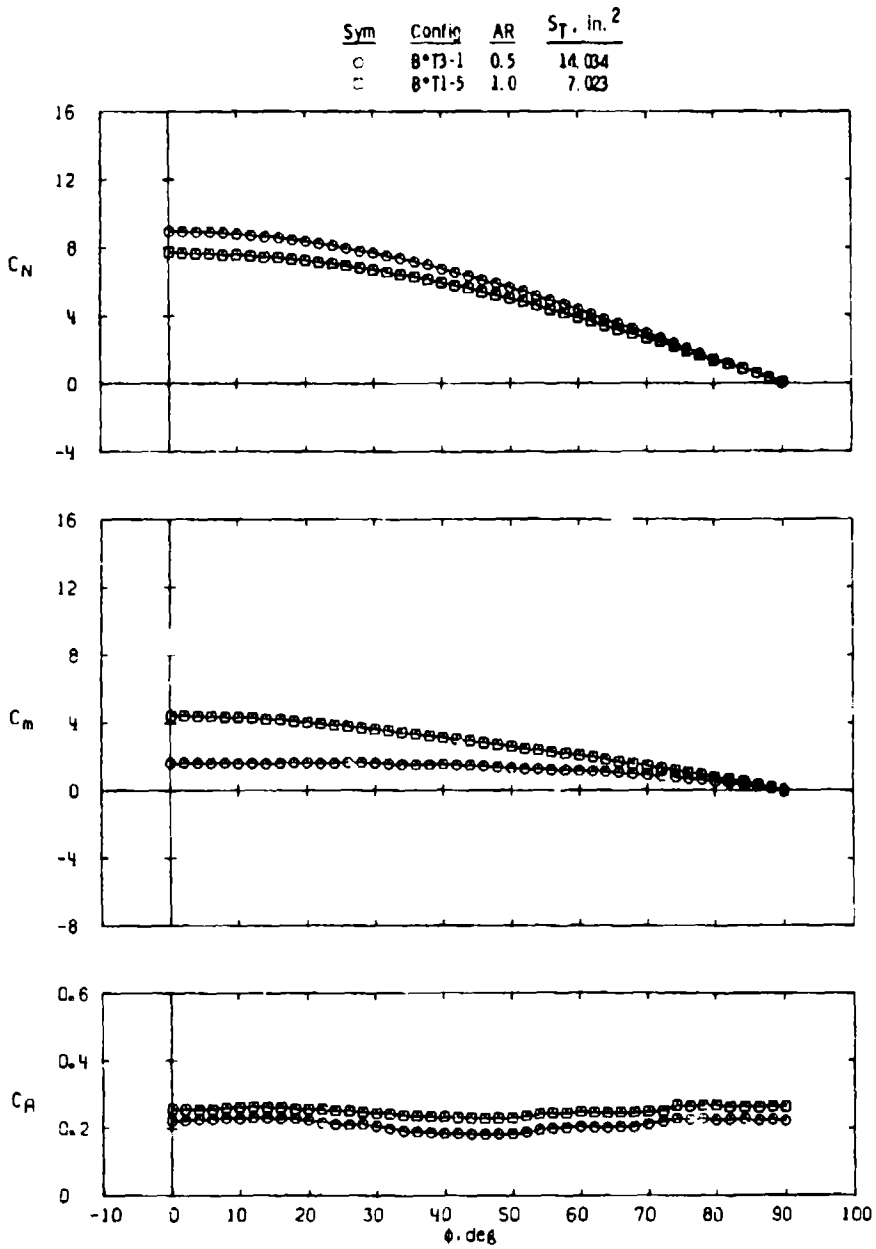

c. $\alpha \approx 32$ deg

Figure 22. Concluded.

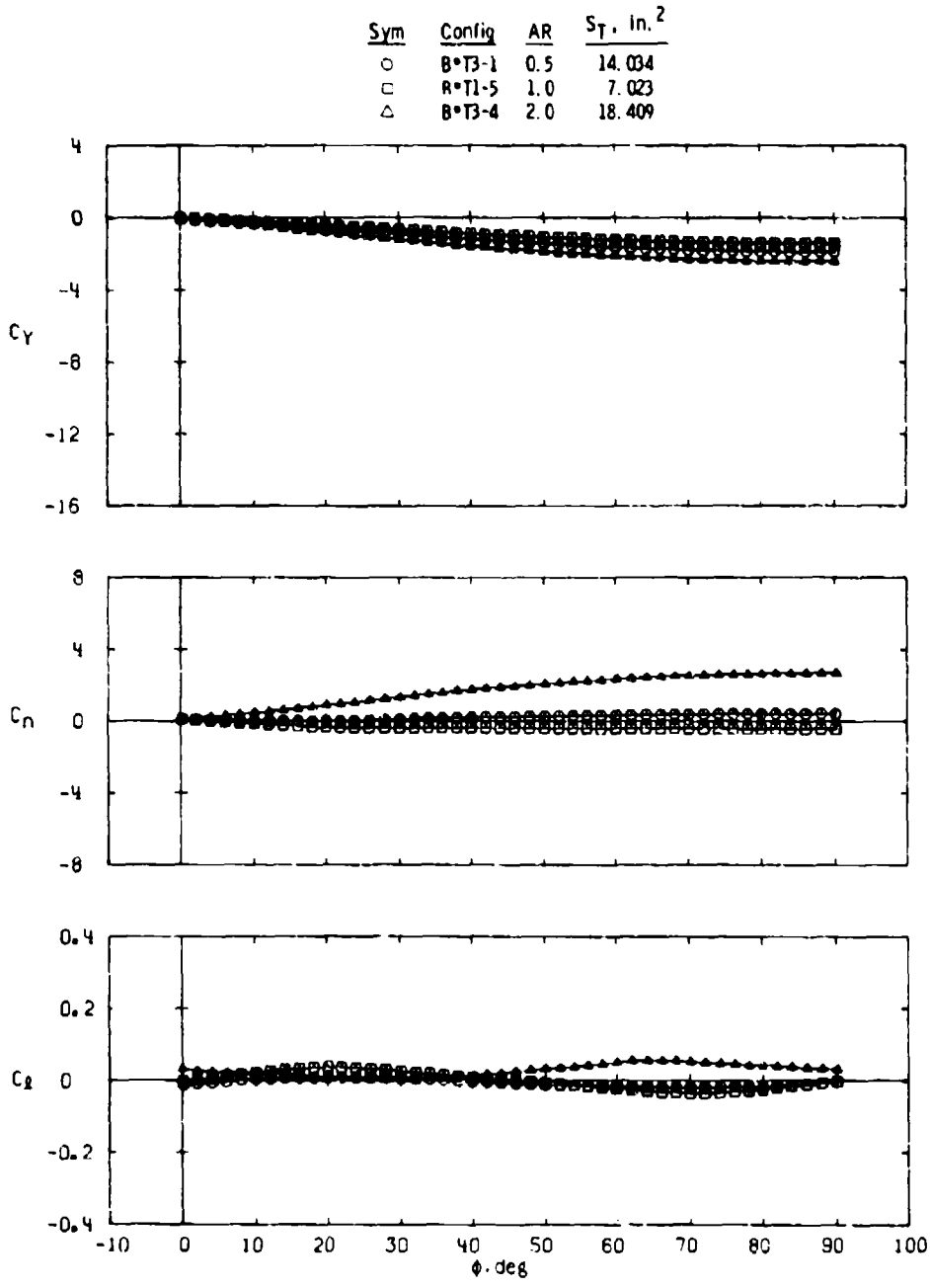

a. $\alpha \approx$ 10 deg

Figure 23. Variations in missile side-force, yawing-moment, and rolling-moment coefficients with roll angle for different delta fin aspect ratios, M_∞ = 2.00.

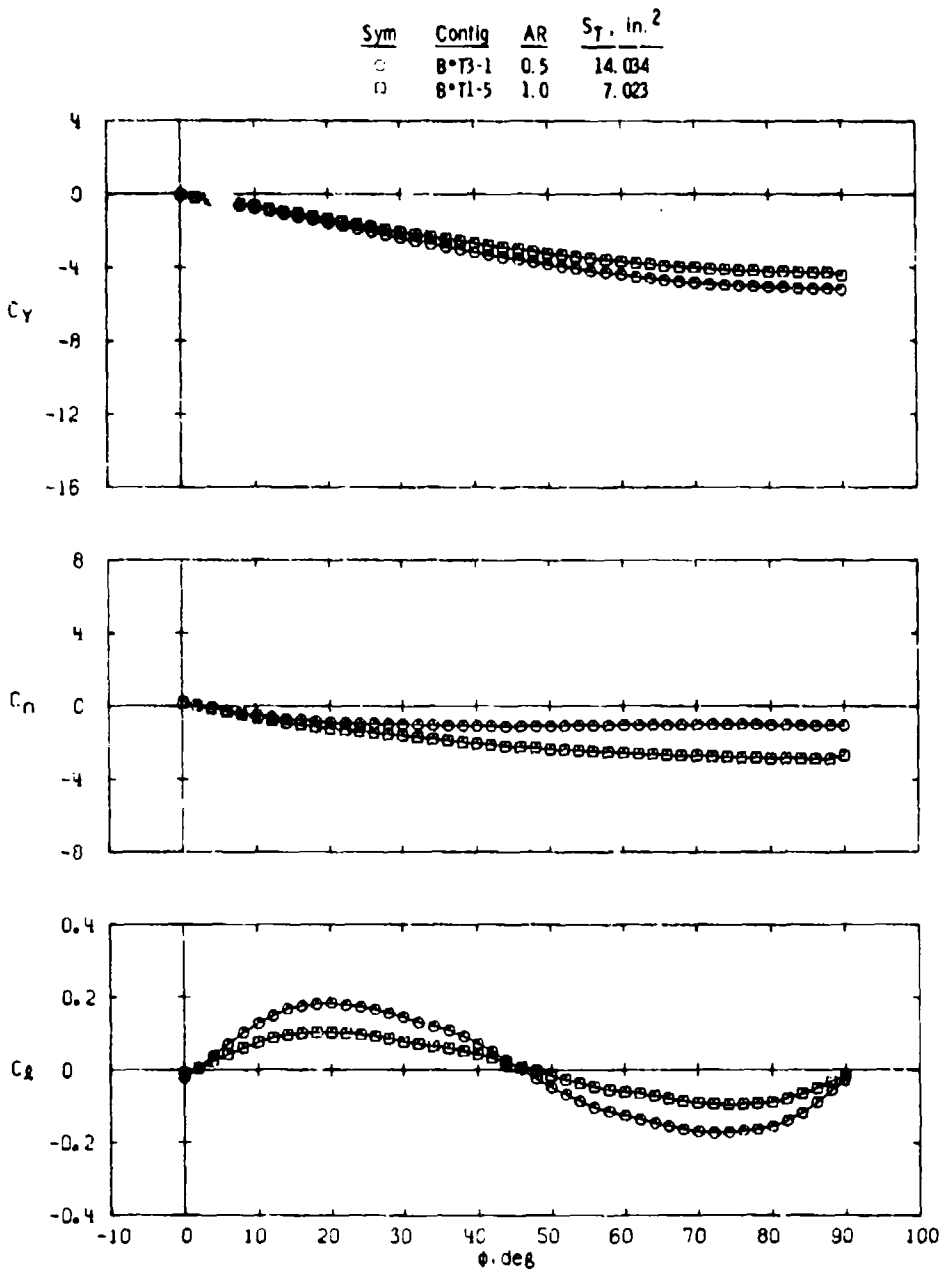

b. $\alpha \approx 21$ deg

Figure 23. Continued.

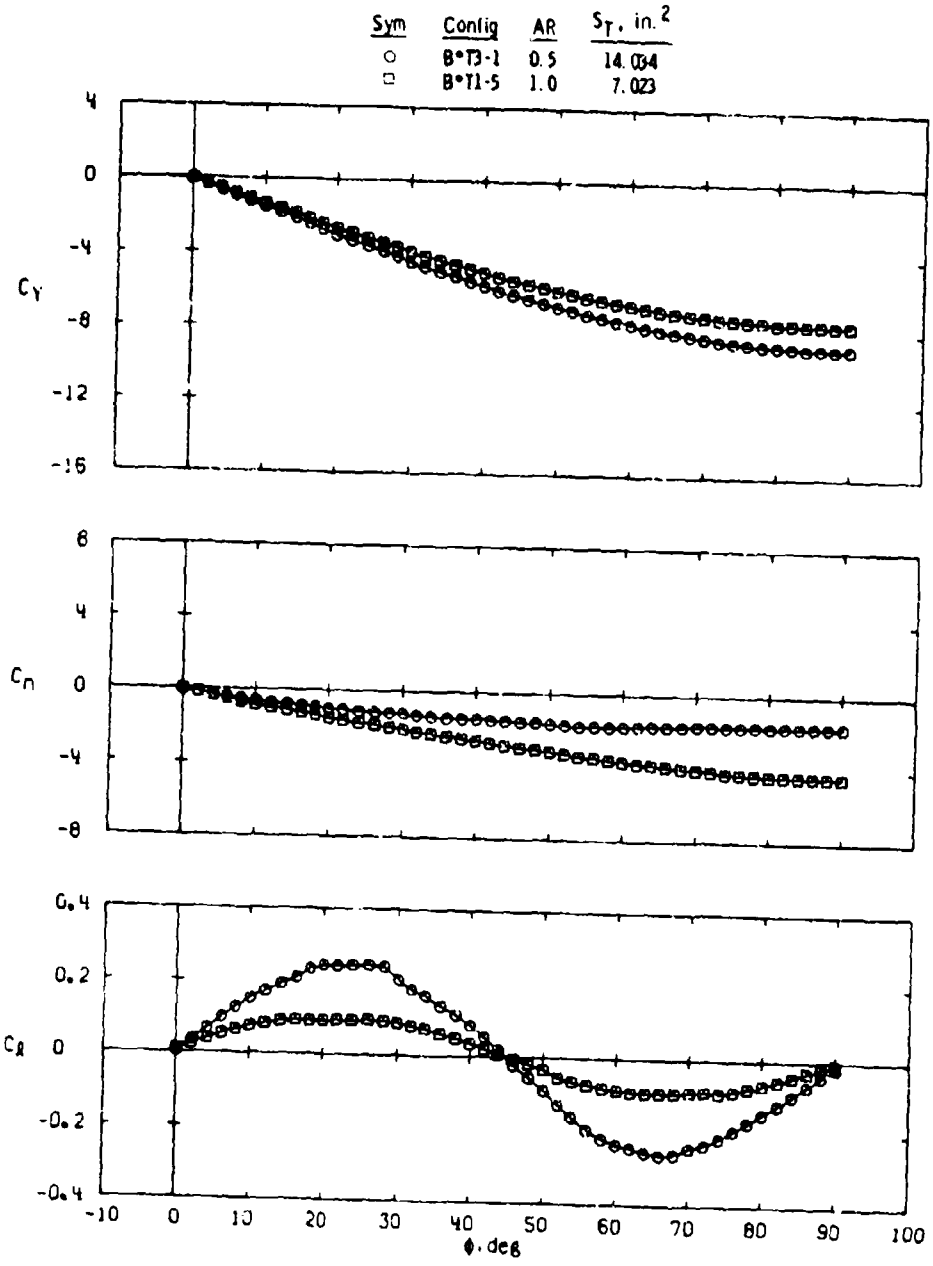

c. $\alpha \approx 32$ deg

Figure 23. Concluded.

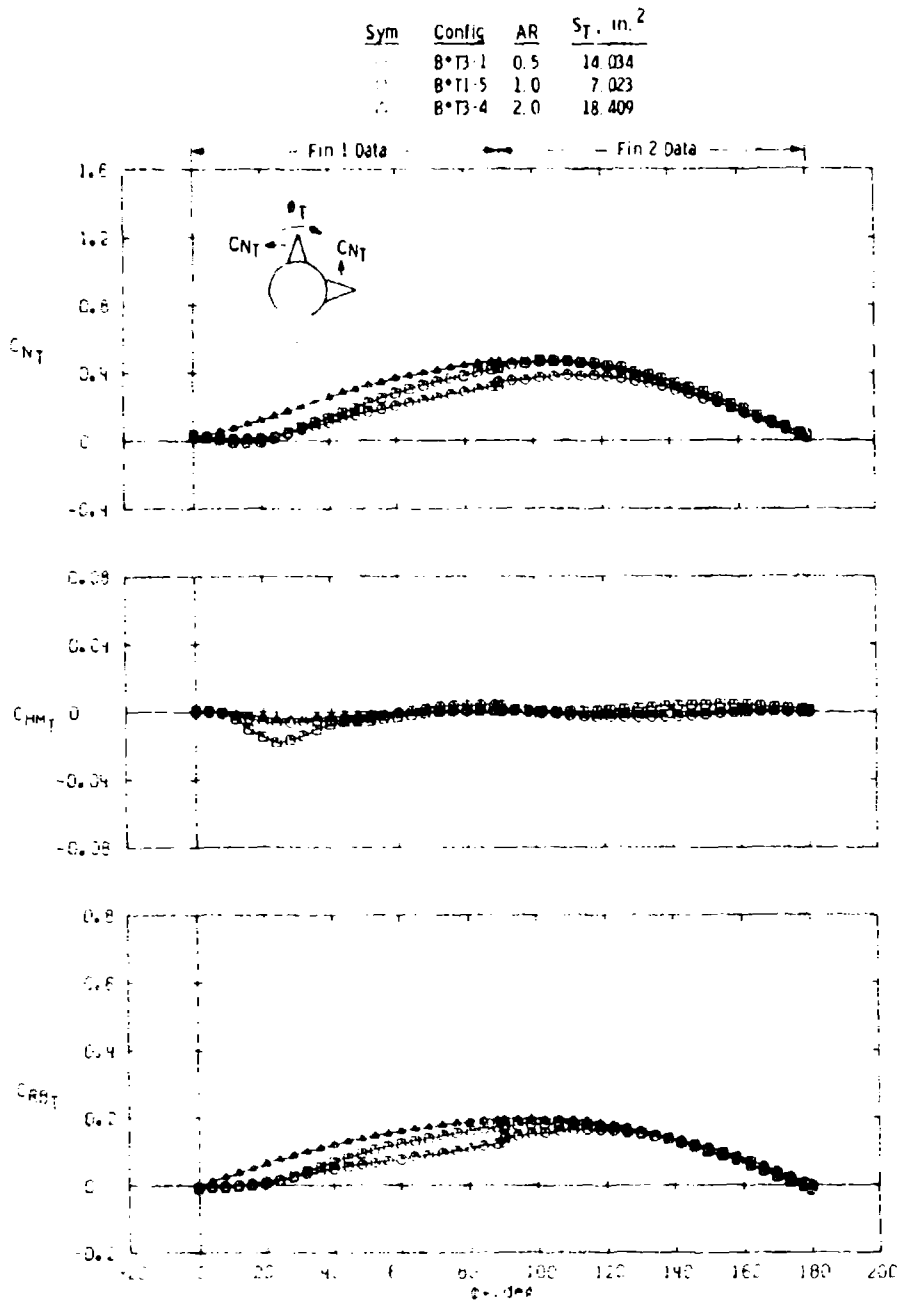

a. α = 10 deg

Figure 24. Variations in fin normal-force, hinge-moment, and bending-moment coefficients with fin roll position for different delta fin aspect ratios, M_∞ = 2.00.

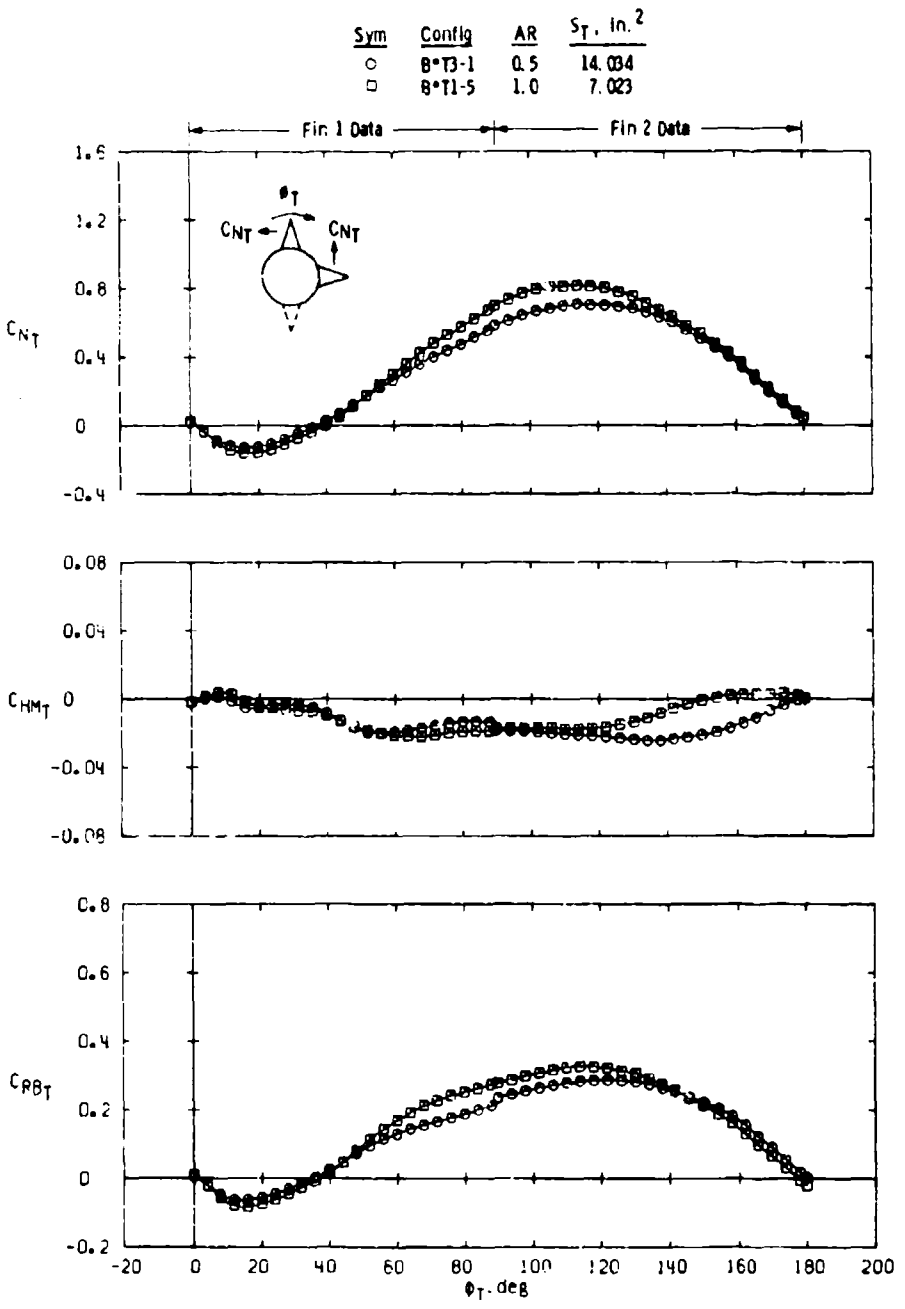

b. $\alpha \approx 21$ deg

Figure 24. Continued.

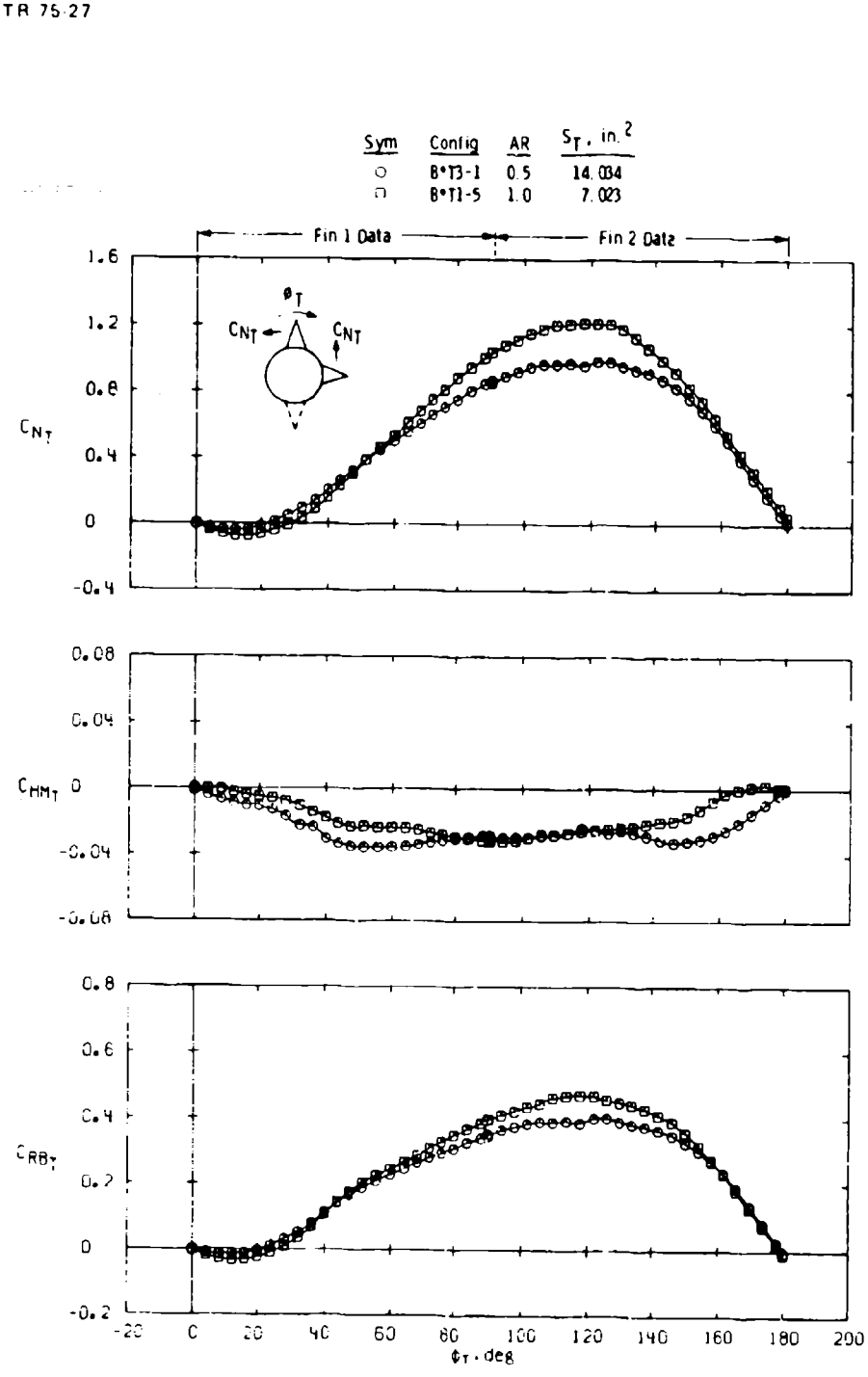

c. $\alpha \approx 32$ deg

Figure 24. Concluded.

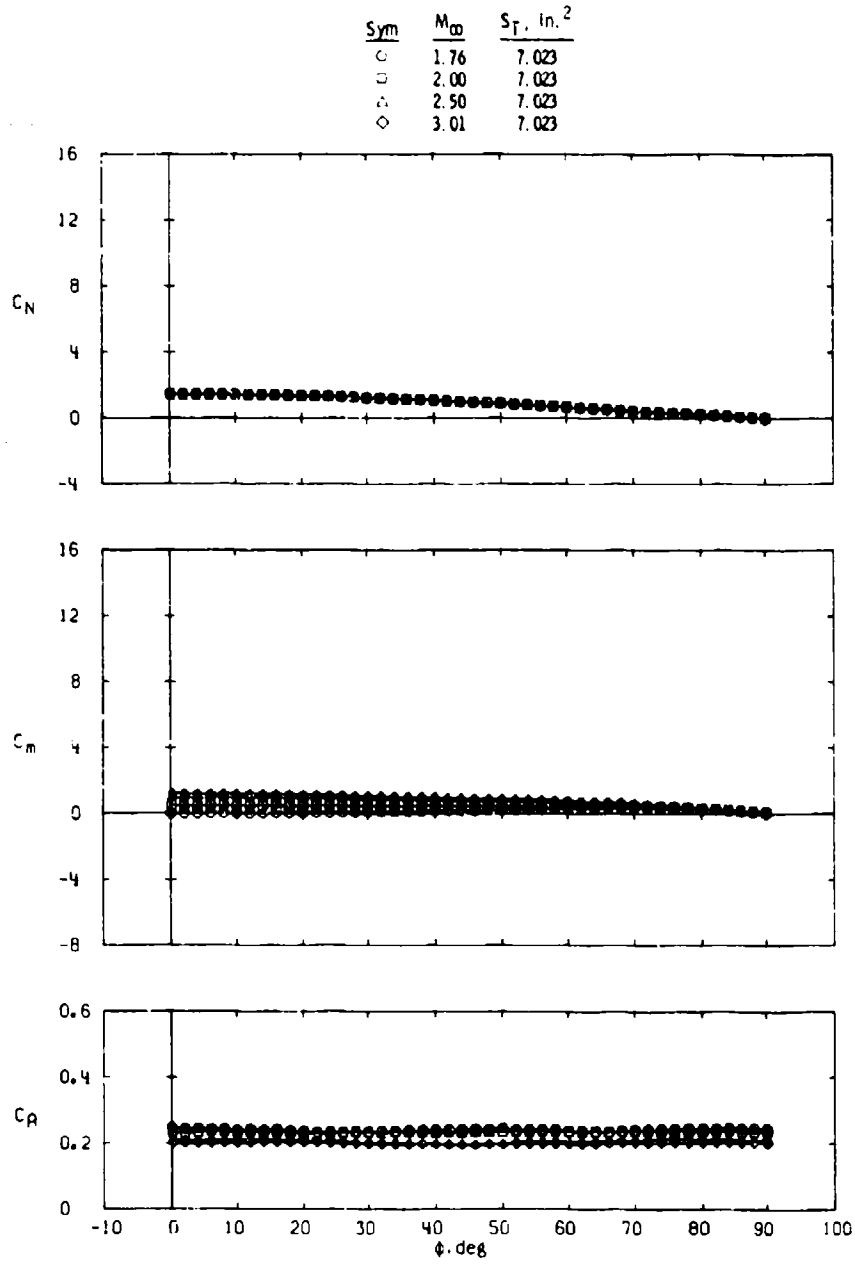

a. $\alpha \approx 10$ deg

Figure 25. Variations in missile normal-force, pitching-moment, and axial-force coefficients with roll angle at different Mach numbers for a delta fin configuration (B*T1-5) of aspect ratio 1.0.

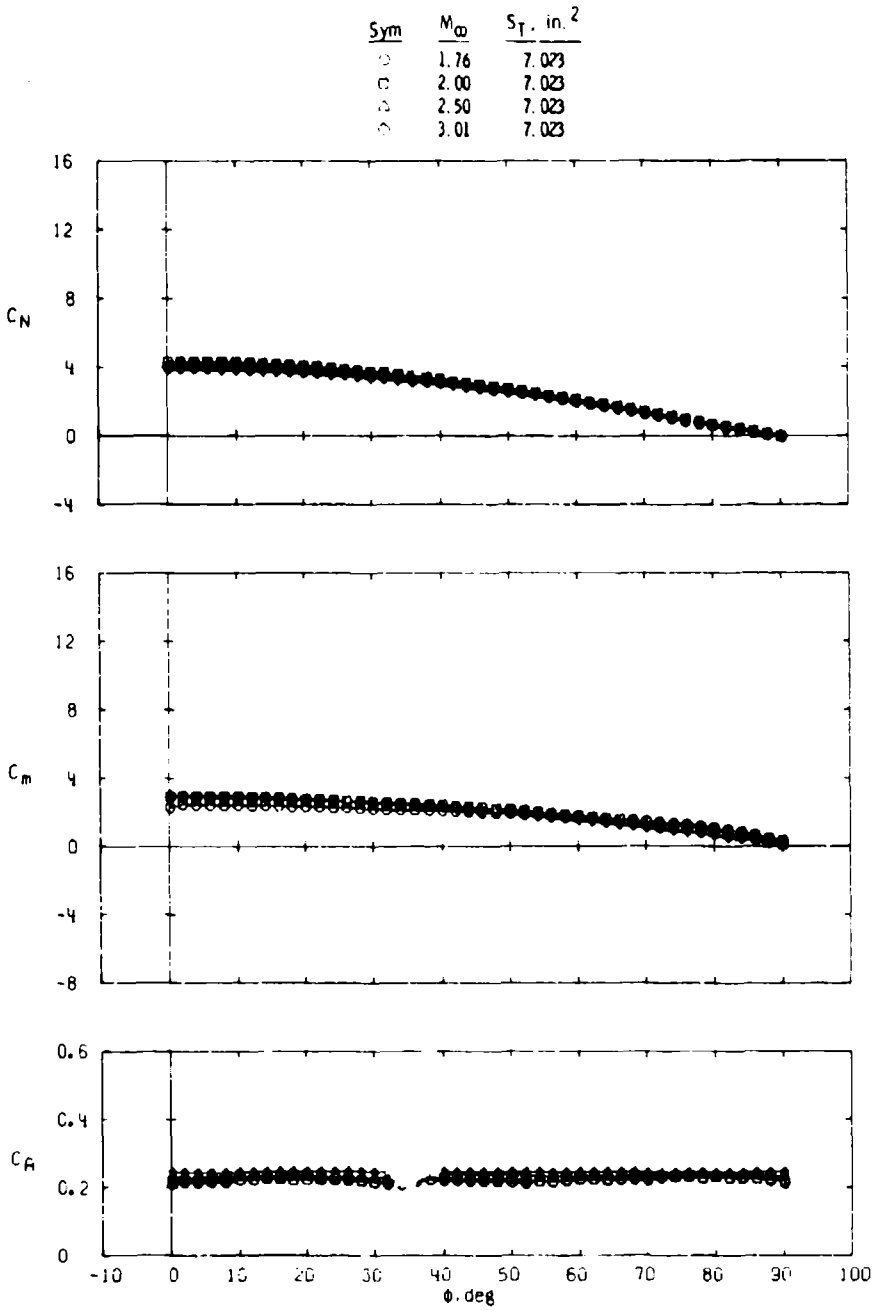

b. $\alpha \approx 21$ deg

Figure 25. Continued.

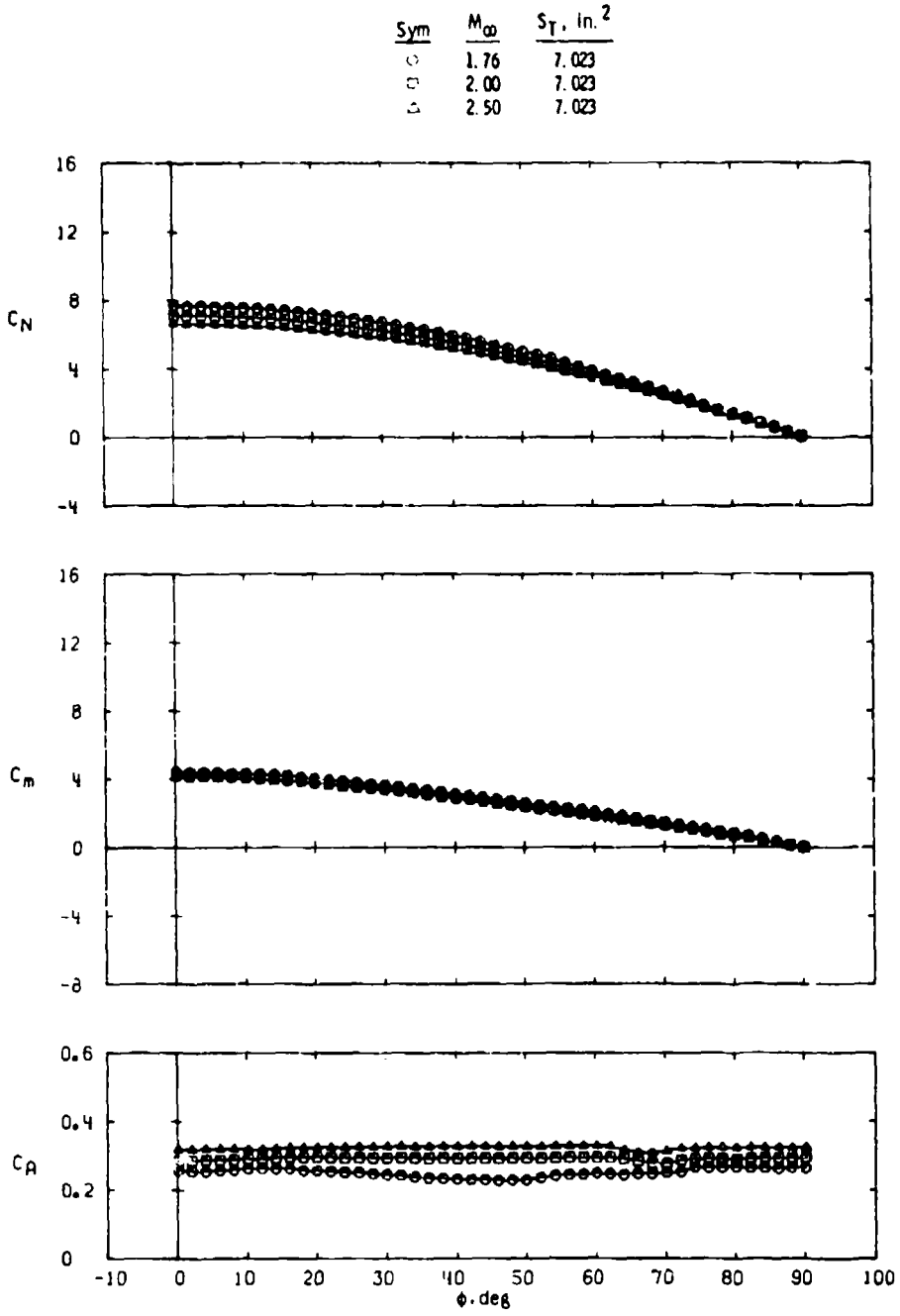

c. $\alpha \approx 32$ deg

Figure 25. Continued.

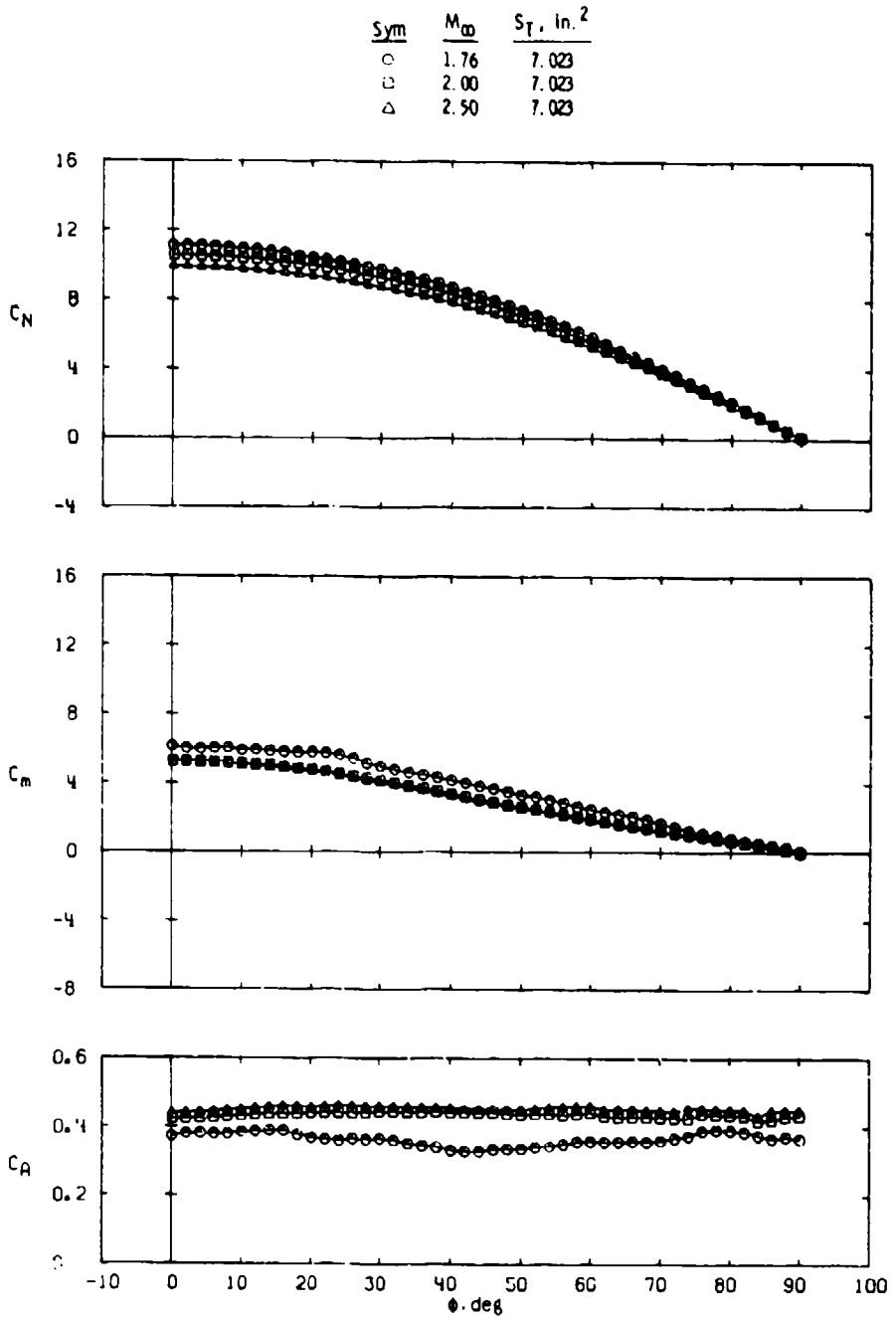

d. $\alpha \approx 43$ deg

Figure 25. Concluded.

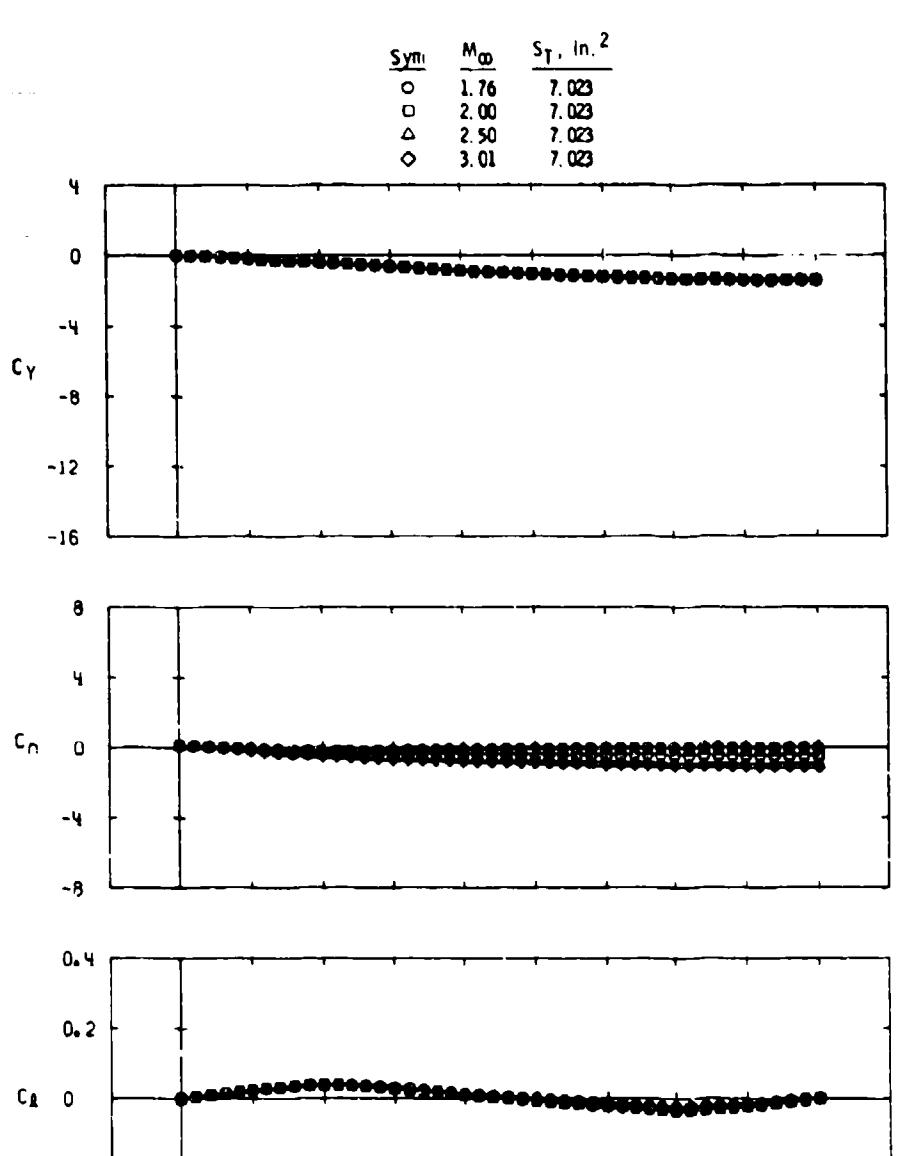

a. $\alpha \approx 10$ deg

Figure 26. Variations in missile side-force, yawing-moment, and rolling-moment coefficients with roll angle at different Mach numbers for a delta fin configuration (B*T1-5) of aspect ratio 1.0.

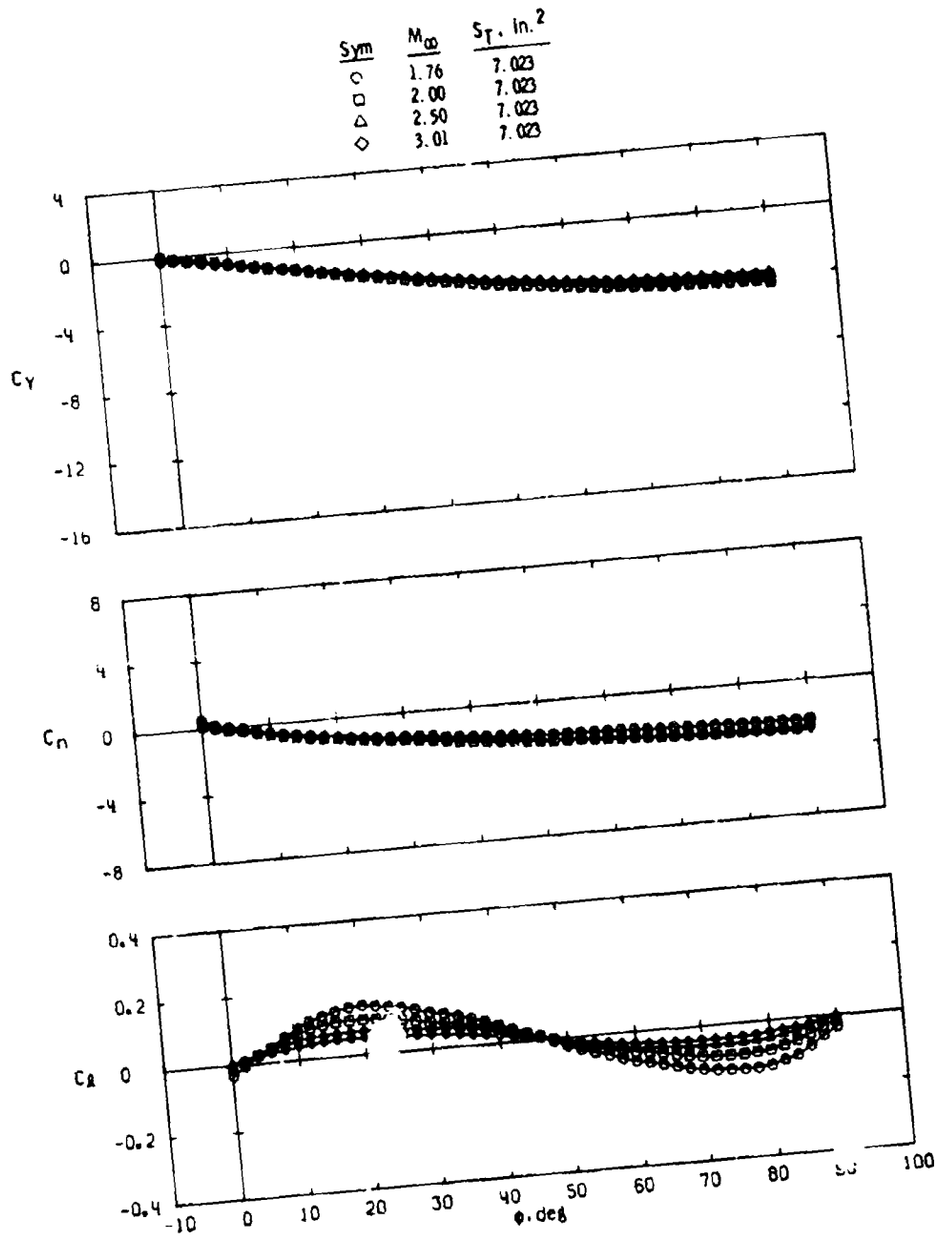

b. $\alpha \approx 21$ deg

Figure 26. Continued.

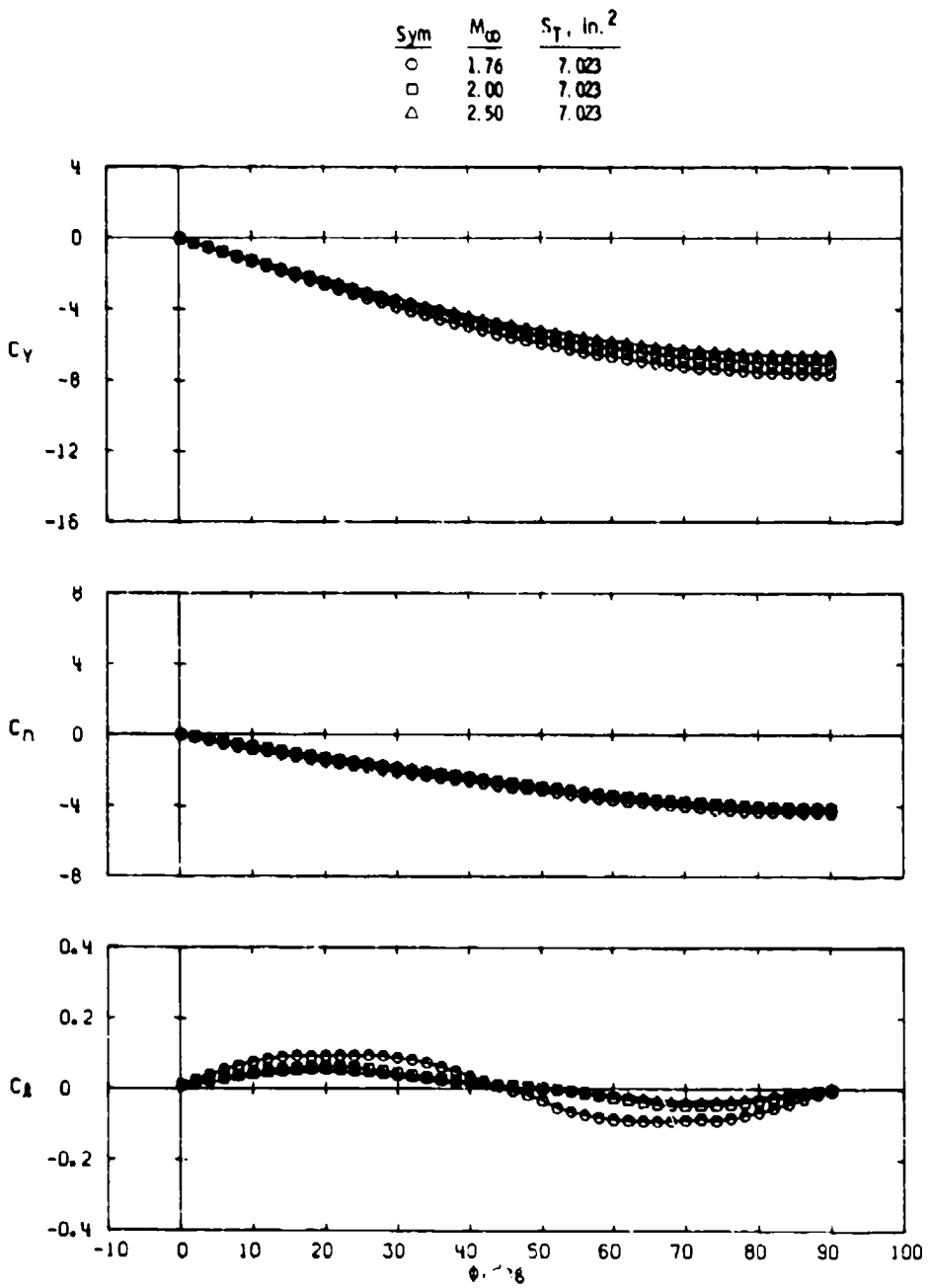

c. $\alpha \approx 32$ deg

Figure 26. Continued.

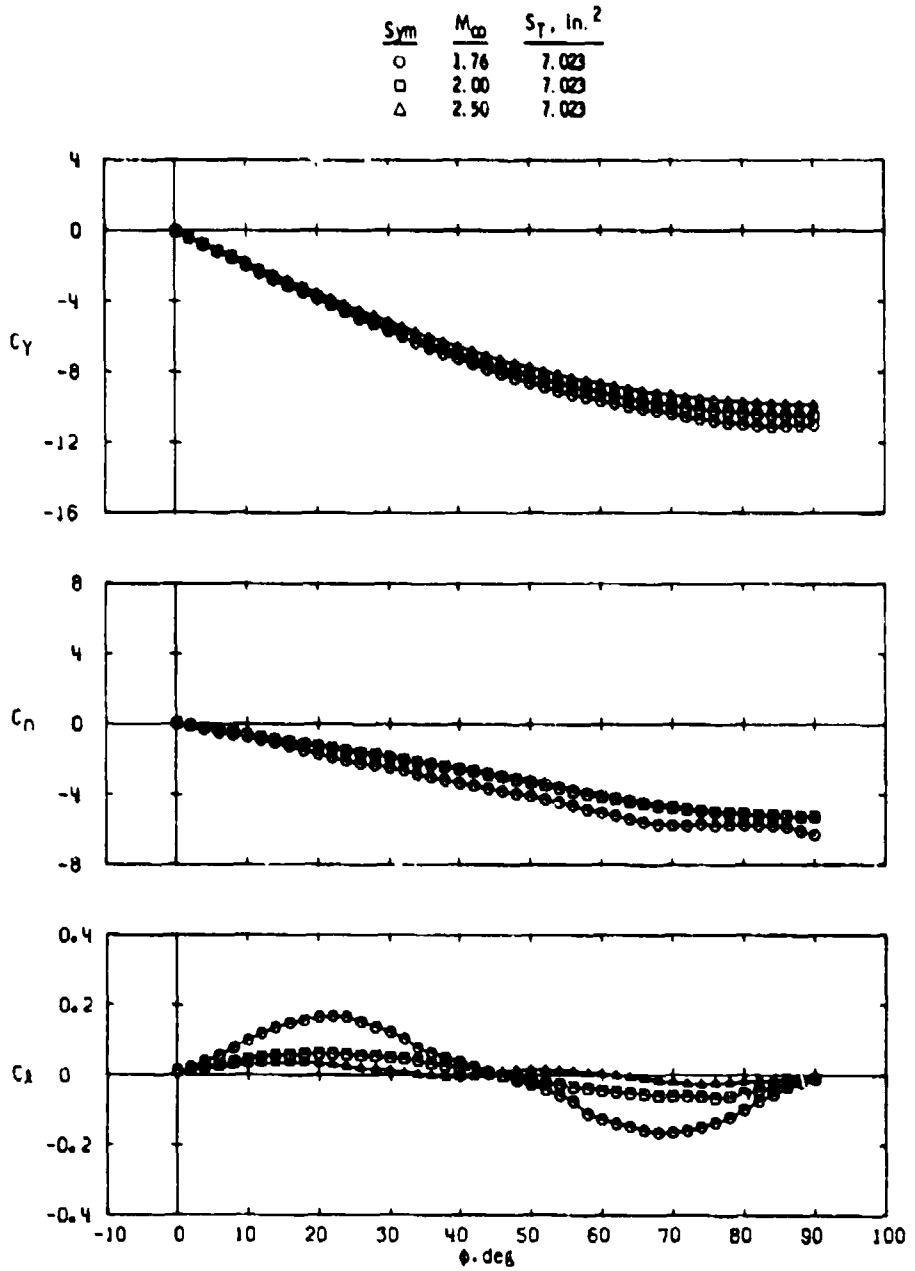

d. $\alpha \approx 43$ deg

Figure 26. Concluded.

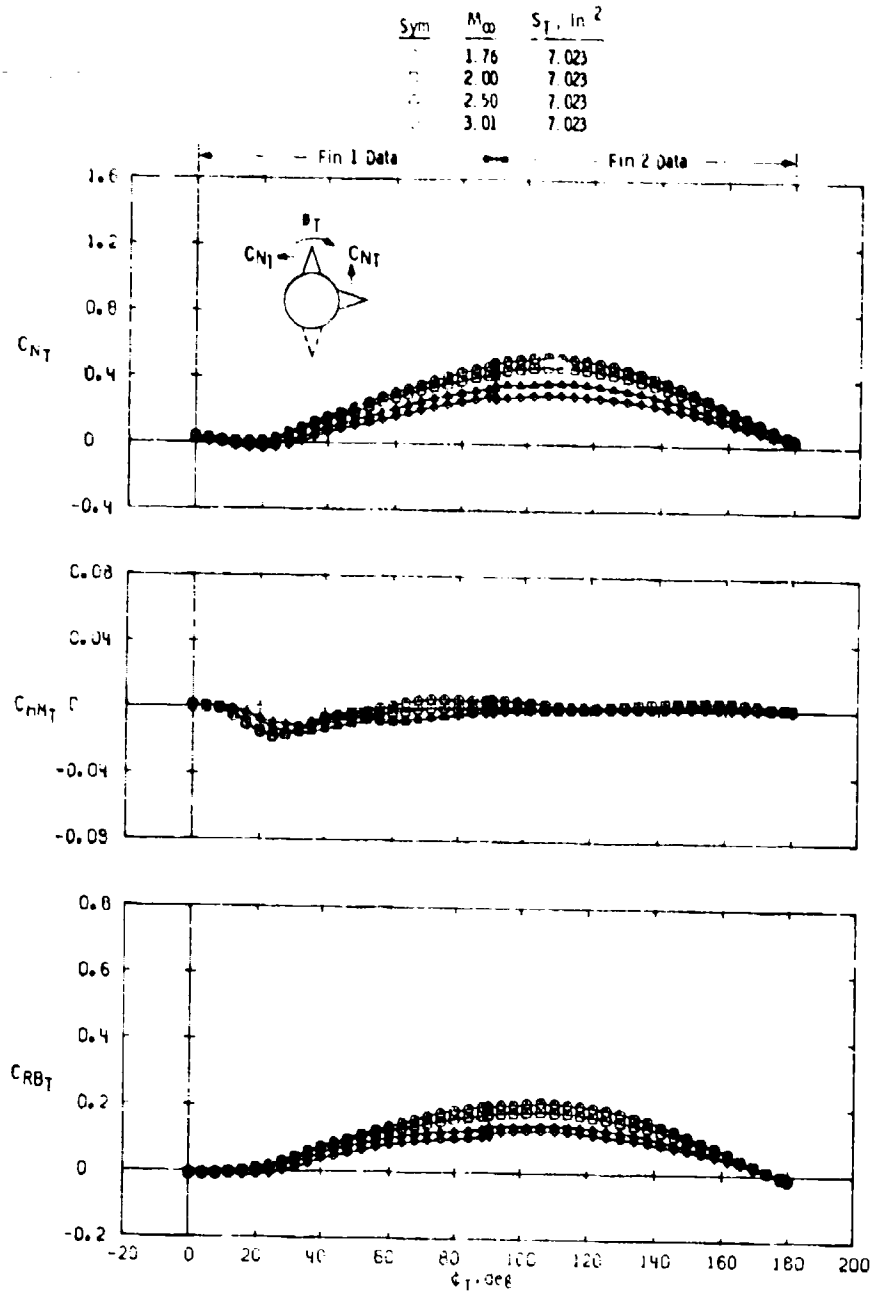

a. $\alpha \approx 10$ deg

Figure 27. Variations in fin normal-force, hinge-moment, and bending-moment coefficients with fin roll position at different Mach numbers for a delta fin configuration (B*T1-5) of aspect ratio 1.0.

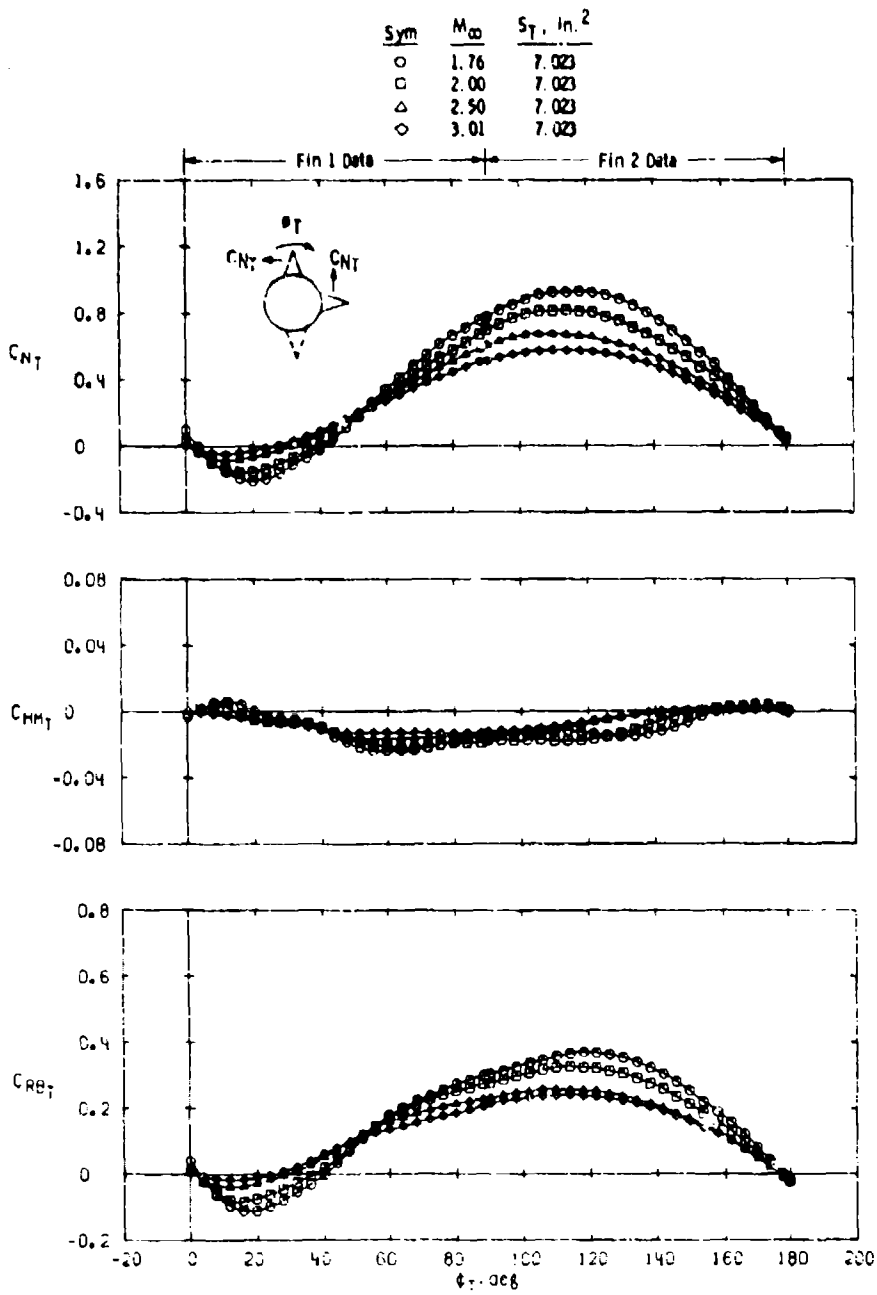

b. $\alpha \approx 21$ deg

Figure 27. Continued.

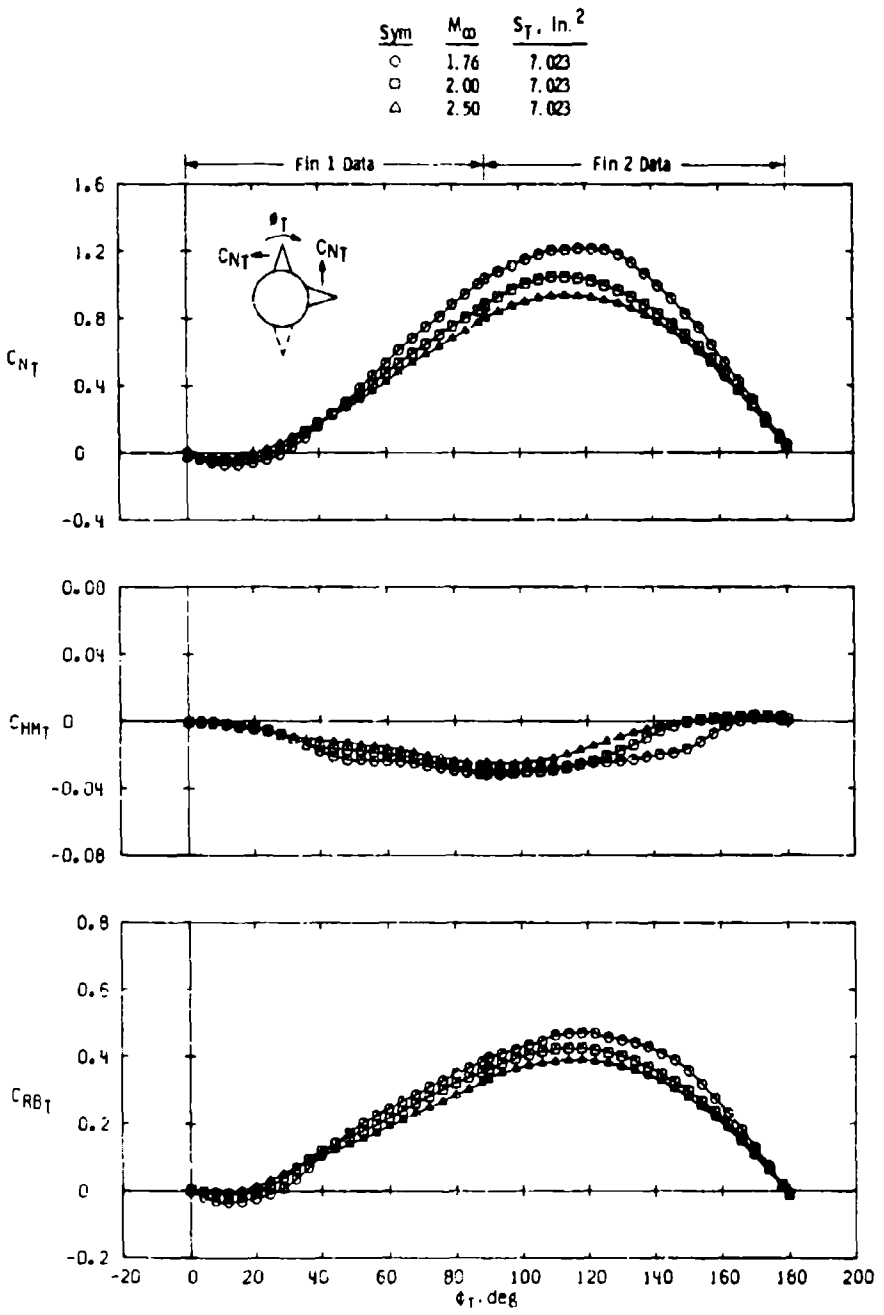

c. $\alpha \approx 32$ deg

Figure 27. Continued.

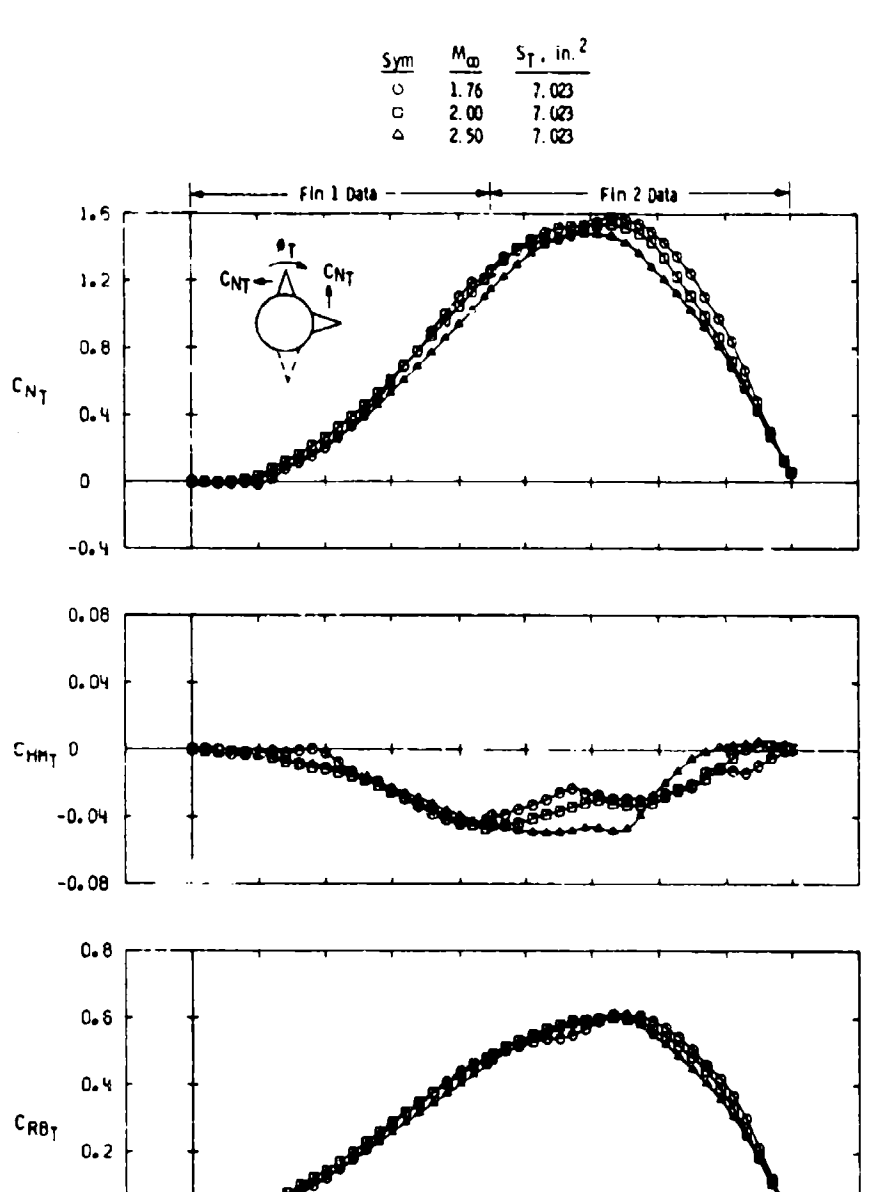

d. $\alpha \approx 43$ deg

Figure 27. Concluded.

Table 1. Test Summary

Configuration	Mach Number	P-P	Continuous Roll Sweep Data, ϕ = 0 to 90 deg, at the Following Nominal Angles of Attack, deg																									
			-1	0	1	2	4	6	8	10	12	15	17	19	21	23	26	28	29	30	32	34	37	39	41	43	44	45
B	1.76	x																										
	2.00	x																										
	2.50	x																										
	3.01	x																										
B•T1-1	1.76	x		x	x	x	x	x	x	x	x	x	x	x	x	x	x	x										
	2.00	x	x	x	x	x	x	x	x		x	x	x	x	x	x	x	x	x	x	x	x	x	x	x	x	x	x
	2.50	x	x	x	x	x	x	x	x		x	x	x	x	x	x	x	x	x	x	x	x	x	x	x	x	x	x
	3.01	x	x	x	x	x	x	x	x	x	x	x	x	x	x	x	x	x	x	x	x	x	x	x	x	x	x	x
B•T1-3	1.76	x		x	x	x	x	x	x	x	x	x	x	x	x	x	x	x										
	2.00	x	x	x	x	x	x	x	x	x	x	x	x	x	x	x	x	x	x	x	x	x	x	x	x	x	x	x
	2.50	x	x	x	x	x	x	x	x	x	x	x	x	x	x	x	x	x	x	x	x	x	x	x	x	x	x	x
	3.01	x	x	x	x	x	x	x	x	x	x	x	x	x	x	x	x	x	x	x	x	x	x	x	x	x	x	x
B•T1-4	1.76	x		x	x	x	x	x	x	x	x	x	x	x	x	x	x	x										
	2.00	x	x	x	x	x	x	x	x	x	x	x	x	x	x	x	x	x	x	x	x	x	x	x	x	x	x	x
	2.50	x	x	x	x	x	x	x	x	x	x	x	x	x	x	x	x	x	x	x	x	x	x	x	x	x	x	x
	3.01	x	x	x	x	x	x	x	x	x	x	x	x	x	x	x	x	x	x	x	x	x	x	x	x	x	x	x
B•T1-5	1.76	x		x	x	x	x	x	x	x	x	x	x	x	x	x	x	x										
	2.00	x	x	x	x	x	x	x	x	x	x	x	x	x	x	x	x	x	x	x	x	x	x	x	x	x	x	x
	2.50	x	x	x	x	x	x	x	x	x	x	x	x	x	x	x	x	x	x	x	x	x	x	x	x	x	x	x
	3.01	x	x	x	x	x	x	x	x	x	x	x	x	x	x	x	x	x	x	x	x	x	x	x	x	x	x	x
B•T2-3	1.76	x		x	x	x	x	x	x	x	x	x	x	x	x	x	x	x										
	2.00	x	x	x	x	x	x	x	x	x	x	x	x	x	x	x	x	x	x	x	x	x	x	x				
	2.50	x	x	x	x	x	x	x	x	x	x	x	x	x	x	x	x	x	x	x	x	x	x	x	x			
	3.01	x	x	x	x	x	x	x	x	x	x	x	x	x	x	x	x	x	x	x	x	x	x	x	x	x	x	x
B•T3-1	1.76	x		x	x	x	x	x	x	x	x	x	x	x	x	x	x	x										
	2.00	x	x	x	x	x	x	x	x	x	x	x	x	x	x	x	x	x	x	x	x	x	x	x				
	2.50	x	x	x	x	x	x	x	x	x	x	x	x	x	x	x	x	x	x	x	x	x	x	x	x			
	3.01	x	x	x	x	x	x	x	x	x	x	x	x	x	x	x	x	x	x	x	x	x	x	x	x	x	x	x
B•T3-2	1.76	x		x	x	x	x	x	x	x	x	x	x	x	x	x	x	x										
	2.00	x	x	x	x	x	x	x	x	x	x	x	x	x	x	x	x	x	x	x	x	x	x	x				
	2.50	x	x	x	x	x	x	x	x	x	x	x	x	x	x	x	x	x	x	x	x	x	x	x	x			
	3.01	x	x	x	x	x	x	x	x	x	x	x	x	x	x	x	x	x	x	x	x	x	x	x	x	x	x	
B•T3-4	1.76	x		x	x	x	x	x	x	x	x																	
	2.00	x	x	x	x	x	x	x	x	x	x	x																
	2.50	x	x	x	x	x	x	x	x	x	x	x																
	3.01	x	x	x	x	x	x	x	x	x	x	x																
B•T3-6	2.00	x															x	x		x	x	x	x	x	x	x		
	2.50	x															x	x		x	x	x	x	x	x	x	x	
	3.01	x															x	x		x	x	x	x	x	x	x	x	x

Notes: 1. P-P indicates pitch-pause data, ϕ = 0, at the same α's noted for roll sweep data for each configuration and Mach number.
2. Body alone (B) pitch-pause groups cover the entire α range at each Mach number except for -1 deg at Mach number 1.76, ϕ = 0.
3. Limitations to the α range were due to fin balance overload, or bow shock reflection crossing the model base, except for the B•T3-6 configuration which was run only during the second phase (α's from 26 to 45 deg).

NOMENCLATURE

AR	Fin aspect ratio, $2b^2/S_T$
b	Exposed fin semispan, in. (see Fig. 4b)
C	Fin root chord, in. (see Fig. 4b)
C_A	Model forebody axial-force coefficient, $C_{A_t} - C_{A_B}$
C_{A_B}	Model base axial-force coefficient, $-(p_b - p_\infty)/q_\infty$
C_{A_t}	Total axial-force coefficient, total axial force/$q_\infty S$
C_{HM_T}	Fin hinge-moment coefficient, hinge moment/$q_\infty S_T C$
C_ℓ	Model rolling-moment coefficient, rolling moment/$q_\infty Sd$
C_m	Model pitching-moment coefficient, pitching moment/$q_\infty Sd$
C_N	Model normal-force coefficient, normal force/$q_\infty S$
C_{N_T}	Fin normal-force coefficient, fin normal force/$q_\infty S_T$
C_n	Model yawing-moment coefficient, yawing moment/$q_\infty Sd$
C_{RB_T}	Fin root chord bending-moment coefficient, root bending moment/$q_\infty S_T b$
C_Y	Model side-force coefficient, side force/$q_\infty S$
d	Model base diameter, d = 3.75 in.
ℓ	Model length, 37.500 in.
M_∞	Free-stream Mach number
p_b	Model base pressure, psia
p_o	Tunnel stilling chamber pressure, psia
p_∞	Free-stream static pressure, psia
q_∞	Free-stream dy. amic pressure, psia
Re_ℓ	Reynolds number based on free-stream conditions and model length

S	Model base area, 11.045 in.^{2}
S_T	Fin exposed semispan planform area, in.^{2}
T_o	Tunnel stilling chamber temperature, °R
α	Model angle of attack in wind axis system, deg
ϕ	Model roll angle, deg
ϕ_T	Fin roll position measured from model zero roll, deg
Λ	Fin leading-edge sweep angle, deg (see Fig. 4b)

CONFIGURATION DESIGNATION

B	Missile body alone (see Fig. 2)
TX-X	A fin where the numbers X-X identify the fin configurations shown in Fig. 4